

HD 62542: Probing the Bare, Dense Core of a Translucent Interstellar Cloud¹

Daniel E. Welty¹, Paule Sonnentrucker¹, Theodore P. Snow², Donald G. York^{3,4}

ABSTRACT

We discuss the interstellar absorption from many atomic and molecular species seen in high-resolution *HST*/STIS UV and high-S/N optical spectra of the moderately reddened B3-5 V star HD 62542. This remarkable sight line exhibits both very steep far-UV extinction and a high fraction of hydrogen in molecular form – with strong absorption from CH, C₂, CN, and CO, but weak absorption from CH⁺ and most of the commonly observed diffuse interstellar bands. Most of the material resides in a single narrow velocity component – offering a rare opportunity to probe the primarily molecular core of a single interstellar cloud with little associated diffuse atomic gas. Detailed analyses of the spectra indicate that (1) the molecular fraction in the main cloud is high [$f(\text{H}_2) \gtrsim 0.8$]; (2) the gas is fairly cold ($T_k = 40\text{--}43$ K; from the rotational excitation of H₂ and C₂); (3) the local hydrogen density $n_{\text{H}} \sim 1500 \text{ cm}^{-3}$ (from the C₂ excitation, the fine-structure excitation of C⁰, and simple chemical models); (4) the unusually high excitation temperatures for ¹²CO and ¹³CO may be largely due to radiative excitation; (5) $N(\text{C}^+):N(\text{CO}):N(\text{C}) \sim 100:10:1$; (6) the depletions of many elements are more severe than those seen in any other sight line, and the detailed pattern of depletions differs from those derived from larger samples of Galactic sight lines; and (7) the various neutral/first ion ratios do not yield consistent estimates for the electron density, even when the effects of grain-assisted recombination and low-temperature dielectronic recombination are considered.

1. INTRODUCTION

While interstellar clouds have long been idealized as uniform spheres or slabs, high-resolution maps of emission due to dust, neutral hydrogen, CO, and other species indicate that both the

⁰Based on observations made with the NASA/ESA *Hubble Space Telescope*, obtained at the Space Telescope Science Institute, which is operated by the Association of Universities for Research in Astronomy, Inc., under NASA contract NAS 5-26555. These observations are associated with program 12277. Based on observations made with ESO telescopes at the La Silla Paranal Observatory, under program IDs 064.I-0475, 072.C-0682, and 099.C-0637.

¹Space Telescope Science Institute, 3700 San Martin Dr., Baltimore, MD 21218; dwelty@stsci.edu

²University of Colorado, CASA – Campus Box 389, Boulder, CO 80309-0001

³University of Chicago, Department of Astronomy and Astrophysics, 5640 S. Ellis Ave., Chicago, IL 60637

⁴also, Enrico Fermi Institute

overall and the internal structure of the clouds are typically more complicated. Filamentary, sheet-like, and fractal-like structures are apparently quite common (e.g., Chappell & Scalo 2001; Heiles & Troland 2003; Kalberla et al. 2016), and clouds containing significant amounts of H_2 generally have colder, denser, predominantly molecular cores surrounded by more diffuse atomic gas (e.g., Andersson et al. 1991; Wannier et al. 1999). Different atomic and molecular species can be concentrated in different (but overlapping) regions within the clouds, based on where the conditions for their survival are most favorable (e.g., Pan et al. 2005). Moreover, many lines of sight exhibit multiple, closely spaced velocity components (assumed to correspond to individual clouds), which can be characterized by rather different properties (e.g., Welty et al. 1994, 1996). While higher spectral resolution can enable us to distinguish predominantly diffuse components from other velocity components containing significant amounts of denser gas, we still cannot separate the diffuse and dense gas contributions that are associated with a single cloud at the same velocity. That inability is particularly vexing for attempts to identify and characterize the so-called “translucent” clouds (with $A_V \sim 1\text{--}5$ mag), thought to be transitional objects between more diffuse, primarily atomic clouds and the denser molecular clouds involved in forming stars (e.g., Snow & McCall 2006). In the cores of such clouds, we expect a molecular fraction $f(\text{H}_2) = 2N(\text{H}_2)/(N(\text{H})+2N(\text{H}_2))$ approaching unity, fairly high densities, and enhanced depletions of refractory (and perhaps even nonrefractory) elements into dust grains. Those characteristics have not yet been observed, however, as most sight lines also include appreciable amounts of more diffuse material (Rachford et al. 2002, 2009; Snow et al. 2002a; Sonnentrucker et al. 2002, 2003).

The sight line toward the moderately reddened B3-5 V star HD 62542 [$E(B - V) \sim 0.35\text{--}0.37$; $A_V \sim 1.0\text{--}1.2$; $R_V \sim 2.7\text{--}3.1$ (Valencic et al. 2004; Fitzpatrick & Massa 2007; Rachford et al. 2009; Gordon et al. 2009)] offers a rare opportunity to probe the relatively dense molecular core of an interstellar cloud, with little associated diffuse atomic gas. This remarkable line of sight intersects a ridge of material in the western part of the *IRAS* Vela shell, foreground to the Gum Nebula (Sahu 1992; Pereyra & Magalhaes 2002), apparently swept up and sculpted by stellar winds, radiation pressure, and/or shocks (Cardelli & Savage 1988; Cardelli et al. 1990; O’Donnell et al. 1992). A portion of that ridge near HD 62542 has been identified as a *Planck* Galactic cold clump (Planck Collaboration 2016; Dirks & Meyer 2019). At a distance of about 390 pc (Gaia 2), HD 62542 apparently lies somewhat beyond that structure, however, as there are no signs of interaction between the star and the intervening interstellar material (Whittet et al. 1993). The far-UV extinction toward HD 62542 is among the steepest known, and the weak, broad 2175Å bump may be shifted to lower wavelengths (Cardelli & Savage 1988; Fitzpatrick & Massa 2007; but see also Valencic et al. 2004; Gordon et al. 2009). The column densities of CN and CH are the highest known for any sight line with $A_V < 2$ mag; the $N(\text{CN})/N(\text{CH})$ and $N(\text{C}_3)/N(\text{C}_2)$ ratios are quite high, but CH^+ is very weak (Cardelli et al. 1990; Gredel et al. 1991, 1993; Ádámkóvics et al. 2003). In addition to fairly strong emission from ^{12}CO (1-0), emission from ^{12}CO (3-2) and from the rare CO isotopolog C^{18}O (the latter usually seen in emission only for $A_V > 3$ mag) are also detected toward HD 62542 (van Dishoeck et al. 1991; Gredel et al. 1994). The typically strongest of the diffuse interstellar bands (DIBs; e.g., those at 5780.6, 5797.2, and 6283.8Å), which

trace predominantly atomic gas, are exceptionally weak toward HD 62542, but the typically much weaker “C₂ DIBs” (which are correlated with molecular gas) are still detected (Snow et al. 2002b; Ádámkóvics et al. 2005). While the available optical and mm-wave spectra had suggested that most of the interstellar material toward HD 62542 resides in a single narrow component at $v_{\odot} \sim 14 \text{ km s}^{-1}$ (Cardelli et al. 1990; Gredel et al. 1991, 1993, 1994), the UV spectra discussed in this paper have revealed a number of other components, with much lower total hydrogen column densities, at velocities from 4 to 32 km s^{-1} . Various diagnostics have yielded estimates for the total hydrogen density n_{H} ranging from several hundred per cm^3 (Black & van Dishoeck 1991) to 10^4 cm^{-3} (Cardelli et al. 1990) in the main cloud. The C₂ rotational excitation and the relative weakness of the mm-wave CN emission, however, have indicated that the local kinetic temperature $T_{\text{k}} \sim 30\text{--}45 \text{ K}$ and $n_{\text{H}} \sim 500\text{--}1000 \text{ cm}^{-3}$ (Gredel et al. 1991, 1993; Sonnentrucker et al. 2007); that density is still rather high for a cloud with $A_{\text{V}} \sim 1$. Cardelli et al. (1990) argued that the cloud is a small, dense knot whose more diffuse outer layers have been stripped away by the winds and radiation pressure from ζ Pup and γ^2 Vel. While the overall $f(\text{H}_2)$ toward HD 62542 is uncertain, it may be as high as 0.88 (Ádámkóvics et al. 2005). The main cloud toward HD 62542 thus may have $f(\text{H}_2) \sim 1$ – making it perhaps the best current candidate for a bona fide single, isolated translucent cloud.

In this paper, we discuss high-resolution UV spectra of HD 62542, obtained with the Space Telescope Imaging Spectrograph (STIS) on board the *Hubble Space Telescope* (*HST*), aimed primarily at characterizing the abundances and physical conditions in the main, largely molecular cloud in that sight line. Section 2 describes the acquisition, processing, and analysis of the spectra. Section 3 presents the derived atomic and molecular column densities and explores the excitation of some of those species. Section 4 discusses the local physical conditions and depletions characterizing the clouds toward HD 62542 (as inferred from those atomic and molecular species) and possible implications for our understanding of interstellar clouds. Section 5 provides a summary of our results and conclusions. Detailed physical/chemical models of the main cloud, based on the data presented here, will be explored in a subsequent paper.

2. OBSERVATIONS AND DATA ANALYSIS

2.1. Optical and UV Spectra

The optical and UV spectra employed in this study of the sight line toward HD 62542 are listed in Table 1. All of the optical spectra were obtained with echelle spectrographs, at high to moderately high spectral resolution (FWHM = 1.26–8.3 km s^{-1}). In each case, standard routines within IRAF were used for the initial processing of the raw data: bias correction, removal of small-scale variations in instrumental response via a normalized flat field, extraction of one-dimensional spectra from the two-dimensional CCD images, and wavelength calibration (typically using exposures of a Th-Ar lamp). More detailed descriptions of the characteristics and processing of the spectra obtained with

Table 1. Optical and UV Spectra

Date	Facility	λ Range	FWHM	S/N ^a	Code
1998 Sep	AAT / UCLES	5075–10295	5.0	70–100	a
1999 Dec	ESO 3.6m / CES+VLC	3933, 5893 ^b	2.00, 1.26	65, 85	c
2002 Dec	Keck I / HIRES	3985–6420	4.5	700–1100	h
2003 Nov	ESO VLT / UVES	3260–6680	4.5–4.9	80–250	u
2013 May	Magellan Clay / MIKE	3350–9500	6.6–8.3	300–900	m
2017 Apr	ESO VLT / UVES	3050–10422	6.5–6.8 ^c	165–625	U
2011 Apr	<i>HST</i> / STIS E140H	1206–1408	2.7	15–60	s
2011 Jun	<i>HST</i> / STIS E140H	1242–1444	2.7	15–60	s
2011 Apr	<i>HST</i> / STIS E230H	1774–2051	2.7	25–50	s
2011 Apr	<i>HST</i> / STIS E230H	2124–2401	2.7	55–85	s

Note. — The Keck I / HIRES spectra were obtained by *Ádámkóvics et al. (2003)*; the 2017 UVES spectra were obtained under program 099.C-0637 (M.-F. Nieva, PI); the other optical spectra were obtained by DEW. The *HST* spectra were obtained under guest observer program 12277 (D. Welty, PI).

^aThe S/N values are derived from the scatter in the fitted continua near the various detected absorption lines.

^bSmall intervals around the Ca II λ 3933 and Na I $\lambda\lambda$ 5889,5895 lines were observed.

^cProfile fits suggest that the actual resolution is closer to 5.1–5.3 km s⁻¹.

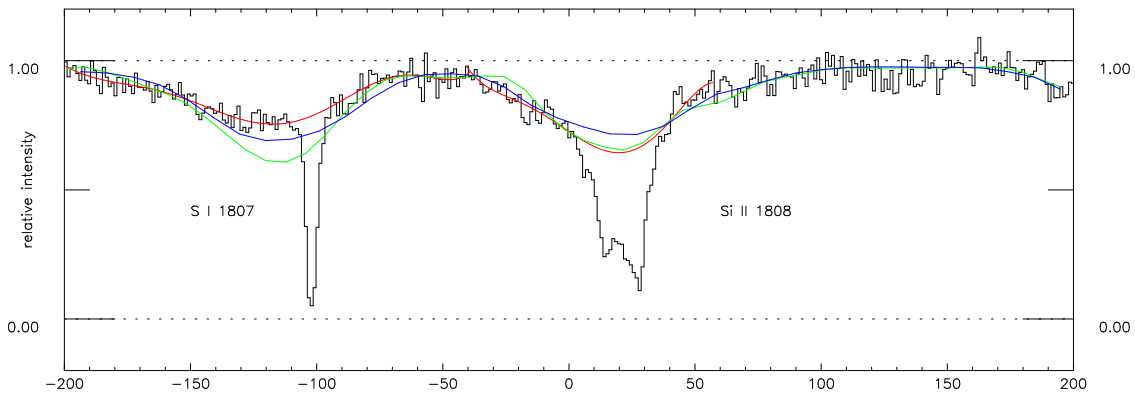


Fig. 1.— Model stellar spectra and continuum fits near the interstellar S I λ 1807 and Si II λ 1808 absorption lines toward HD 62542. The black histogram gives the observed spectrum; the blue and green curves give the predicted spectra from *Thusty* stellar models with $T_{\text{eff}} = 18,000$ K [$\log g = 3.75$, $vsini = 30$ km s⁻¹ in green; $\log g = 4.25$, $vsini = 40$ km s⁻¹ in blue], approximately matched in the stellar continuum regions; the red curves give the adopted local continuum fits around the interstellar absorption lines. As the predicted strengths of the stellar absorption lines do not perfectly match the observed line strengths, the model spectra are just taken to constrain the stellar $vsini$ (~ 35 km s⁻¹) and the curvature for “reasonable” fits to the local continua around the interstellar absorption features.

the University College London Echelle Spectrograph (UCLES; Walker & Diego 1985), the Coudé Echelle Spectrograph (CES; Enard 1982) and the Ultraviolet and Visual Echelle Spectrograph (UVES; Dekker et al. 2000) can be found in Welty et al. (2006) and D. E. Welty & P. A. Crowther (2020, in preparation); the 2017 UVES spectra are the standard pipeline data products. The High Resolution Echelle Spectrometer (HIRES; Vogt et al. 1994) spectra have been described by Ádámkóvics et al. (2003). For this study, the highest resolution CES spectra of the Na I $\lambda\lambda 5889, 5895$ and Ca II $\lambda 3933$ lines were used to identify the major interstellar velocity components in the sight line, while the higher signal-to-noise ratio (S/N) HIRES and UVES spectra (primarily) were used to obtain accurate equivalent widths of the interstellar absorption lines from various atomic and molecular species. The last column of the table gives a one-letter code used to identify the sources of the data in Appendix Tables 10, 11, and 12.

The high-resolution UV spectra were obtained with *HST*/STIS, using the E140H and E230H echelle gratings, during four visits (18 total orbits) in 2011. The four settings each covered about 200–275 Å, centered at the nominal wavelength values (1307, 1343, 1913, and 2263 Å); use of the 0.2×0.09 arcsec slit yielded a resolution of about 2.7 km s^{−1} in each case. The standard pipeline-processed spectral data (extracted, wavelength calibrated) were retrieved from the MAST archive², and the multiple individual spectra for each setting were checked for any systematic wavelength offsets via fits to relatively strong interstellar absorption features. After adjustment for those offsets (which in all cases were less than 0.3 km s^{−1}), spectra for the individual orders were combined via sinc interpolation to a common, slightly oversampled heliocentric wavelength grid. Spectral regions of overlap between adjacent orders were also combined, after checking for mutual consistency. In order to examine the broad Ly α absorption line of atomic hydrogen, the 15 spectral orders within the range 1200–1255 Å were rebinned to a coarser wavelength scale, matched in the regions of overlap, and merged into a single spectrum.

2.2. Equivalent Widths of Absorption Features

Small spectral regions around atomic and molecular lines of interest were extracted from the processed optical and UV spectra of HD 62542, in order to measure the strengths of those features and to perform detailed fits to the line profiles (where complex velocity component structure could be discerned). Those spectral segments were normalized via low-order polynomial fits to the continuum regions adjacent to the absorption features. The continuum fits required some care – particularly for the broader absorption features due to the stronger lines from some dominant species – given the relatively low projected rotational velocity ($v \sin i \sim 35$ km s^{−1}) of HD 62542³ and, in a number of cases, the presence of stellar absorption features adjacent to or overlapping the in-

²<http://archive.stsci.edu/hst>; all of the STIS spectra are available in the MAST archive at <https://doi.org/10.17909/t9-20tr-2053>.

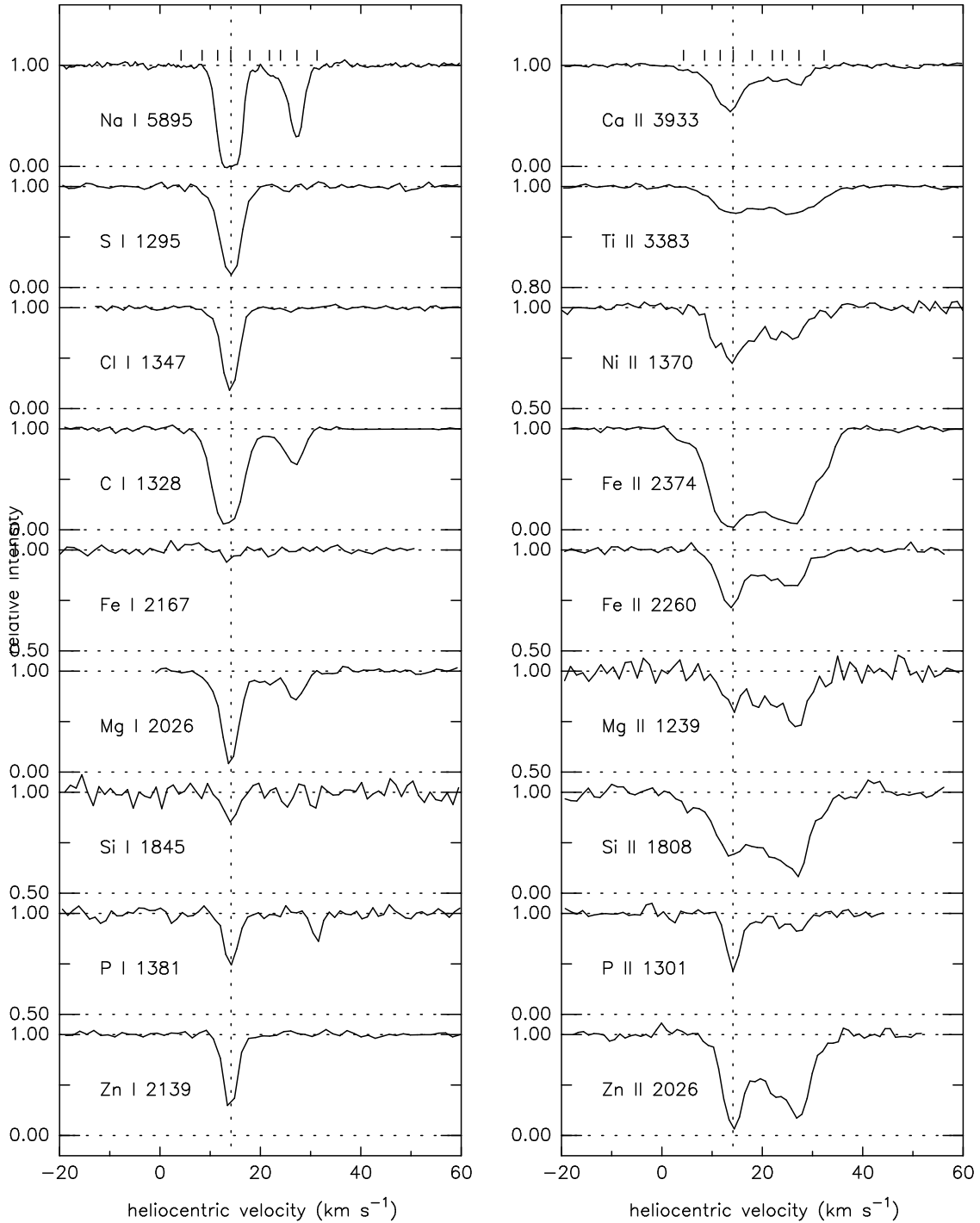


Fig. 2.— Normalized spectra of selected atomic species toward HD 62542. The UV spectra are from STIS (FWHM ~ 2.7 km s $^{-1}$); the optical spectra are from ESO/CES (FWHM ~ 1.26 – 2.0 km s $^{-1}$) or ESO/UVES (FWHM ~ 6.8 km s $^{-1}$). On the left are trace neutral species, concentrated in the main narrow component near 14 km s $^{-1}$ (vertical dotted line). On the right are singly ionized species (dominant ions in predominantly neutral gas), with contributions from components spread over velocities from about 4 to 32 km s $^{-1}$. Tick marks above the Na I $\lambda 5895$ and Ca II $\lambda 3933$ profiles indicate the individual components determined in detailed fits to those profiles. The differences in profile for the dominant species reflect both element-to-element and component-to-component differences in depletions.

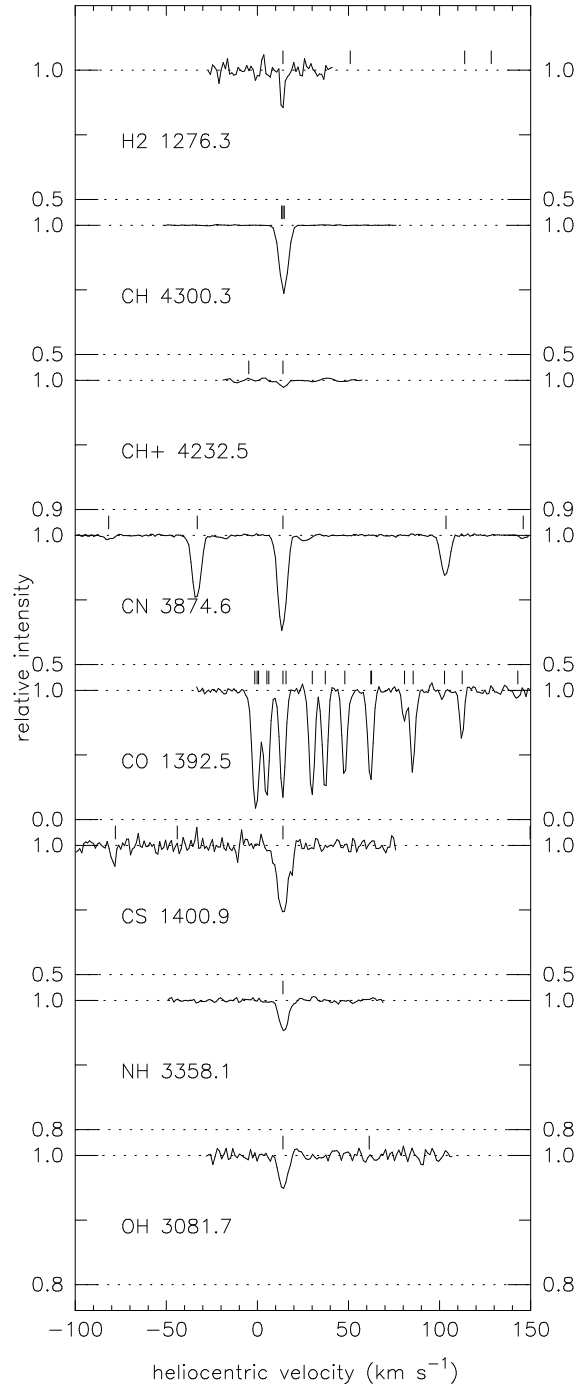


Fig. 3.— Spectra of selected molecular species toward HD 62542. The UV spectra are from STIS (FWHM $\sim 2.7 \text{ km s}^{-1}$); the optical spectra are from Keck/HIRES or VLT/UVES (FWHM $\sim 4.5\text{--}6.8 \text{ km s}^{-1}$). The tick marks above the spectra indicate absorption from the main component at 14 km s^{-1} . For CN $\lambda 3874.6$, the R2, R1, P1, and P2 lines flank the main R0 line at that velocity; the weak unmarked features just to the right of the R1 and R0 lines are due to ^{13}CN . For CO $\lambda 1392.5$, lines from rotational levels $J=0\text{--}6$ (in the R, Q, and P branches) are detected; see also Appendix Figures 21 and 22. For CS $\lambda 1400.9$, the weak line near -80 km s^{-1} is due to Sn II in the main 14 km s^{-1} component. For several other cases, the "extra" tick marks give the locations of nearby lines of other species (whether detected or not).

terstellar lines. For some of those cases, the continuum fits were checked for reasonableness via comparisons with synthetic stellar spectra generated with the *Tlusty* code (Hubeny & Lanz 1995; Lanz & Hubeny 2007), for models with $T_{\text{eff}} = 18000$ K, $\log g = 3.75$ or 4.25 , and $v \sin i = 30$ or 40 km s⁻¹ (Figure 1). As the predicted strengths of the stellar absorption lines generally do not perfectly match the observed line strengths, the model spectra are just taken to constrain the stellar $v \sin i$ and the curvature for "reasonable" fits to the local continua around the interstellar absorption features. For the Na I $\lambda\lambda 5889, 5895$ and Ca II $\lambda 3933$ line profiles, stellar contributions from Na I, C II ($\lambda 5889$), Ca II, and S II ($\lambda 3933$) – consistent with those found by Crawford (1990) around the Ca II lines but stronger than that around the Na I lines – were fitted and removed.

Figures 2 and 3 show the normalized profiles for interstellar absorption due to some of the atomic and molecular species detected toward HD 62542. The absorption from both trace neutral atomic species (left-hand column of Fig. 2) and molecules (Fig. 3) is dominated by an apparently single strong, narrow component near a heliocentric velocity of 14 km s⁻¹; several of the stronger lines from the trace neutral species show additional weaker absorption components at somewhat higher velocities. Those additional components are relatively more prominent for the various singly ionized species (which are dominant ionization states in predominantly neutral interstellar clouds), whose profiles are shown in the right-hand column of Fig. 2; in some cases (e.g., Mg II, Si II), the "main" component near 14 km s⁻¹ appears not to have the highest column density.

Both the equivalent widths of detected absorption features and apparent optical depth (AOD) estimates for the corresponding column densities (e.g., Hobbs 1969; Sembach & Savage 1992) were obtained by direct integration over the line profiles in the normalized spectra; values for lines due to various atomic and molecular species are listed in Appendix Tables 10, 11, and 12. In general, the equivalent widths measured for the CH, C₂, and CN lines found in the optical spectra agree quite well with previously reported values (Cardelli et al. 1990; Gredel et al. 1991, 1993). The tables include some lines which are present in the spectra, but which could not be measured due to blending with either stellar or other interstellar absorption lines. While transition f values were taken from Morton (2000, 2003) for most of the atomic species, the f values used for C I are those adopted by Jenkins & Tripp (2001, 2011); other exceptions are noted in Table 10. For species with measurements for multiple lines, differences in the AOD column density estimates may reflect problems with the f values (generally for weaker lines) and/or saturation effects (for stronger lines). In a few cases where the AOD column density estimates obtained from relatively weak lines seemed inconsistent, we have adopted revised f values, as noted in Table 10. In general, the AOD column densities are lower limits to the true values, and they are consistent with the total sight-line column densities obtained from detailed fits to the line profiles (see next section). The rms deviation of the scatter in the continuum regions yielded empirical estimates for the local S/N ratios (see the ranges for each data set given in Table 1), which were used to estimate both the uncertainties in the equivalent widths of detected lines and upper limits for undetected lines. The

³The $v \sin i = 113$ km s⁻¹ found by Balona (1975) is too high.

uncertainties (1σ) and upper limits (3σ) include contributions from both photon noise (Jenkins et al. 1973) and continuum placement (Sembach & Savage 1992), added in quadrature. The two sources of uncertainty are generally comparable for the narrower lines (e.g., from most trace neutral species), but the continuum uncertainties are larger (often by of order 50%) for the broader lines from dominant singly ionized species. Blending with stellar lines can also increase the effective uncertainties for some of the interstellar absorption features.

2.3. Fits to Absorption-line Profiles

Multicomponent fits to the absorption-line profiles were performed in order to determine column densities for the "individual" components discernible for the various neutral and singly ionized atomic and molecular species that trace the predominantly neutral gas toward HD 62542, using the program FITS6P (e.g., Welty et al. 2003) and a variant of that program which can simultaneously fit multiple, widely separated lines (from the same or different species) having a common component structure. Initial, independent fits to the highest resolution CES spectra of Na I and Ca II yielded very similar component velocities and line widths (b values) for those two species (columns 2 and 3 of Table 2). For the main component near 14 km s^{-1} – which strongly dominates the absorption for the molecular and trace neutral atomic species – the b value for each species was determined by requiring consistent fits to both strong and weak lines (where possible – e.g., for Na I, the strong D lines at 5890 and 5896 Å and the much weaker $\lambda 3302$ doublet). The resulting main-component b values range from 0.8 to 0.95 km s^{-1} for the trace neutral species, and from 1.0 to 1.5 km s^{-1} for the dominant singly ionized species. For neutral carbon, separate simultaneous fits were performed for the unblended lines of C I, C I*, and C I**; the adopted $b = 0.85\text{--}0.90 \text{ km s}^{-1}$ and the resulting total $\log[N(\text{C I})] = 15.41$ for the main component are in good agreement with the values (1.0 km s^{-1} , 15.46) obtained by Dirks & Meyer (2019) from the same spectra.⁴ For these small b values, even relatively weak absorption lines will yield noticeable differences in the column densities derived from the equivalent widths (assumed optically thin), from AOD integrations over the line profiles, and from fits to the line profiles. As an example, for $b = 1.0 \text{ km s}^{-1}$, the $N(\text{O I})$ obtained for the main component from the weak $\lambda 1355$ line ($W = 6.8 \text{ mÅ}$) are about 3.5, 4.5, and $5.8 \times 10^{17} \text{ cm}^{-2}$, respectively, for the three methods. Given the relatively low temperatures ($T \sim 40\text{--}43 \text{ K}$) obtained for that component from analyses of the excitation of H_2 and C_2 (Sec. 4.1.1), the line widths appear to be dominated by turbulence (or unresolved velocity structure). For all other components, both the relative velocities and the b values determined in the Na I and Ca II fits were used (with slight adjustments in some cases) in fitting the lines from other trace neutral

⁴Contributions from ^{13}C , assuming the average interstellar $^{12}\text{C}/^{13}\text{C}$ ratio ~ 70 (see Sec. 4.2.2), were considered for the C I $\lambda 1328$ multiplet, for which the difference in velocity (relative to the ^{12}C lines) is of order -2 km s^{-1} (Morton 2003; Berengut et al. 2006). Those contributions produced only slight changes in the line profiles, however. Contributions from ^{13}C were not considered for the other C I multiplets, where the velocity differences are even smaller ($\lesssim 0.25 \text{ km s}^{-1}$; Berengut et al. 2006).

Table 2. Component Structures (Atomic Species)

Comp	v (km s ⁻¹)	b (km s ⁻¹)	Na I ($\times 10^{10}$)	C I ($\times 10^{12}$)	C I* ($\times 10^{12}$)	C I** ($\times 10^{12}$)	C I _{tot} ($\times 10^{12}$)	Mg I ($\times 10^{11}$)	S I ($\times 10^{11}$)	Zn I ($\times 10^{11}$)
1	[4.2]	[1.5]	<6.0
2	[8.4]	[2.0]	<6.0	1.8±0.3	2.3±0.5	0.9±0.4	5.0±0.7	4.3±1.3
3	11.5±0.2	[1.0]	24.0±6.0	11.2±1.3	13.5±1.4	14.8±1.4	39.5±2.4	3.9±2.3	16.0±4.0	...
4	14.1±0.1	0.85±0.10	11000±2000	800±80	1260±100	490±30	2550±132	650±60	4400±200	13.5±3.5
		b	0.85	[0.9]	[0.85]	[0.85]	...	[0.95]	[0.9]	[0.8]
5	17.9±0.3	[1.0]	3.5±1.2	2.4±0.5	2.0±0.6	1.6±0.5	6.0±0.9	4.3±1.3	6.2±3.6	...
6	21.8±0.2	[1.0]	5.3±0.9	0.4±0.2	<1.5	<1.2	<3.1	7.5±1.4	<5.4	...
7	24.0±0.2	[1.0]	8.1±0.9	1.2±0.3	0.6±0.5	<1.2	1.8±0.6	<3.9	<4.8	...
8	27.3±0.1	1.4±0.1	76.0±2.0	5.3±0.3	1.2±0.5	0.9±0.4	7.4±0.7	22.9±1.7	2.6±1.5	...
9	31.3±0.3	[1.0]	1.9±0.4	<0.6	<1.5	<1.2	<3.3	<3.0	<3.9	...
Comp	v (km s ⁻¹)	b (km s ⁻¹)	Ca II ($\times 10^{10}$)	Mg II ($\times 10^{13}$)	Si II ($\times 10^{13}$)	P II ($\times 10^{12}$)	Ti II ($\times 10^{10}$)	Fe II ($\times 10^{12}$)	Ni II ($\times 10^{11}$)	Zn II ($\times 10^{11}$)
1	4.3±0.4	[1.5]	2.4±0.5	<14.3	6.5±1.7	<5.4	<0.9	4.0±1.0	<10.0	<0.8
2	8.5±0.4	[2.0]	6.8±1.0	4.9±5.9	8.7±2.3	<6.5	1.1±0.6	9.0±1.2	4.3±4.6	0.6±0.4
3	11.6±0.2	[1.5]	19.2±1.5	6.0±6.6	19.4±3.6	<9.3	5.1±1.0	45.6±6.4	32.1±8.6	1.9±0.8
4	14.2±0.1	[1.5]	25.8±1.7	25.9±6.5	30.0±4.5	73.0±5.4	4.9±0.9	65.3±8.4	39.0±6.8	74.0±14.3
		b	[1.5]	[1.2]	[1.2]	[1.2]	[1.5]	[1.2]	[1.2]	[1.2]
5	18.0±0.2	[2.5]	14.4±0.9	36.8±7.0	41.4±3.4	8.9±2.7	6.9±0.7	47.5±3.1	41.8±5.8	9.3±0.7
6	[22.0]	[1.5]	5.0±0.8	23.8±8.1	28.9±4.9	<7.7	3.2±1.0	24.3±3.8	11.9±5.4	9.5±0.9
7	[24.0]	[1.5]	5.5±0.8	13.5±8.5	21.6±5.4	7.4±2.7	3.3±0.9	26.7±4.6	17.9±5.7	5.5±1.0
8	27.3±0.1	[1.8]	12.5±0.6	61.6±7.5	81.4±9.6	16.7±2.3	8.6±0.6	64.4±5.4	28.4±5.3	31.6±2.0
9	32.3±0.6	[1.5]	1.3±0.4	5.3±4.9	9.7±1.7	<4.9	3.1±0.5	12.7±0.9	5.2±3.5	1.9±0.3

Note. — Velocites and b values for the neutral and singly ionized species were determined from fits to the higher resolution Na I and Ca II profiles, respectively. Values in square braces were fixed in the fits. Only the b value for the main component (4, in bold) was varied for different species.

and singly ionized species, respectively.

The individual component column densities derived from those detailed profile fits are given in the upper and lower parts of Table 2, respectively. As examples, the adopted fits to the absorption from the weak $\lambda 2260$ and strong $\lambda 2374$ lines of Fe II are shown in Figure 4, and the fits to the seven observed C I multiplets are shown in Appendix Figure 24. Additional very weak components between about -7 and 2 km s^{-1} and near 37 km s^{-1} may be seen in the strongest lines of some dominant species (e.g., Si II $\lambda 1304$, Fe II $\lambda 2344$), but the column densities are rather uncertain due to the difficulty in accounting for stellar lines in fitting the local continua around those weak interstellar features. Estimated column densities for those weak, outlying components are included in the total sight line and "other components" column densities in Table 3, but the individual values are not listed in Table 2. The column densities for the main component can be sensitive to b if only single, moderately strong lines are available (e.g., for Zn I and Zn II). For Zn II, decreasing the main-component b from the adopted 1.2 km s^{-1} to 1.0 km s^{-1} (which also yields acceptable fits to the line profile) increases the derived N_m by a factor of 2. The column densities for the other, generally weaker components can be uncertain if only relatively weak or very strong lines are available (e.g., for C II, O I, some of the trace neutral species, and the dominant ions of many of the heaviest elements) – due to blending with the main component and/or stellar lines and/or to uncertainties in continuum placement.

Absorption from molecular species is detected only for the main component near 14 km s^{-1} . As for the neutral atomic species, the column densities and b values listed in Table 4 for that component were determined by requiring consistent fits for both weak and strong lines. For CH (with three multiplets in the optical spectra), $b = 1.0 \text{ km s}^{-1}$ was adopted. For CN (three multiplets) and C₂ (one UV and three optical multiplets), however, the best fits were for $b = 0.7 \text{ km s}^{-1}$ – as found for CN by Gredel et al. (1991). For CO, $b = 0.5 \text{ km s}^{-1}$ gave the most consistent column densities for the many A-X band lines from rotational levels $J = 0-6$ (Appendix Table 13); the values obtained from fits assuming $b = 0.4$ and 0.7 km s^{-1} were noticeably less consistent. For $b = 0.5 \text{ km s}^{-1}$, the total $\log[N(^{12}\text{CO})] = 16.42$ obtained from the permitted CO A-X bands is consistent with the values determined from the much weaker CO intersystem bands and from the observed CO emission (van Dishoeck et al. 1991); the adopted b and derived total $\log[N(^{12}\text{CO})]$ are also in good agreement with the values (0.5 km s^{-1} , 16.49) obtained from the same STIS spectra by Dirks & Meyer (2019). The corresponding $\text{FWHM} = 1.665 \times b \sim 0.8 \text{ km s}^{-1}$ for ^{12}CO is smaller than the width of the ^{12}CO (1–0) emission line seen toward HD 62542 (1.5 km s^{-1} for a $43''$ beam; Gredel et al. 1994), but is comparable to the widths of the weaker ^{13}CO and C ^{18}O emission lines ($0.4-1.1 \text{ km s}^{-1}$). The fits to the absorption from the observed ^{12}CO and ^{13}CO bands are shown in Appendix Figures 25 and 26.

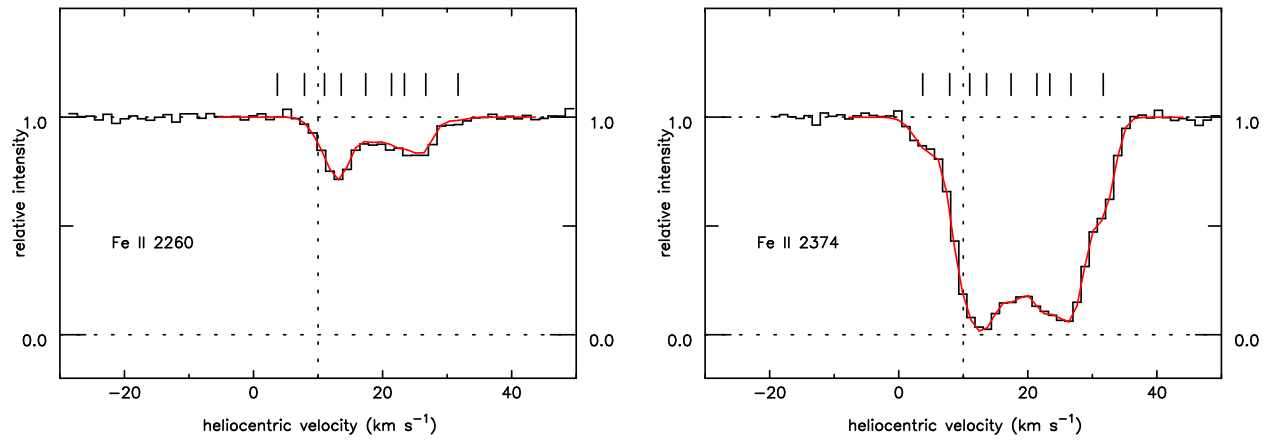


Fig. 4.— Normalized spectra of the weak $\lambda 2260$ and strong $\lambda 2374$ lines of Fe II toward HD 62542. The black histogram is the observed spectrum; the red smooth curve is the adopted fit. The tick marks give the positions of the nine components adopted in the fits (see Table 2).

Table 3. Column Densities and Depletions – Atomic Species

Species	A_{\odot}^a	Main component		All other components		Total sight line	
		$\log[N_m]$	Depletion	$\log[N_o]^b$	Depletion	$\log[N]$	Depletion
H		[20.48]	...	[20.30]	...	20.70 ± 0.18	...
H ₂		20.81 ± 0.21	...	[<18.8]	...	20.81 ± 0.21	...
H _{tot}		21.20 ± 0.17	...	[20.30]	...	21.26 ± 0.18	...
B II	2.85	<10.91	< -1.14	<11.04	< -1.07
C I	8.46	14.90 ± 0.04	...	13.35 ± 0.05	...	14.92 ± 0.04	...
C I*		15.10 ± 0.03	...	13.29 ± 0.04	...	15.11 ± 0.03	...
C I**		14.69 ± 0.03	...	13.26 ± 0.04	...	14.71 ± 0.03	...
C I (total)		15.41 ± 0.02	...	13.78 ± 0.03	...	15.42 ± 0.02	...
C II		<17.96	<18.08	< +0.36
N I	7.90	>15.02	> -2.14
O I ^c	8.76	17.76 ± 0.02	-0.20	[17.82]	[-0.20]
O I*		13.60 ± 0.05	[13.65]	...
O I**		13.32 ± 0.04	[13.37]	...
Na I	6.37	14.04 ± 0.08	...	12.07 ± 0.02	...	14.05 ± 0.08	...
Mg I	7.62	13.81 ± 0.04	...	12.63 ± 0.04	...	13.84 ± 0.04	...
Mg II		14.41 ± 0.11	-2.41	15.18 ± 0.05	-0.74	15.25 ± 0.05	-1.63
Al I	6.54	<10.62	<10.74	...
Al III		12.45 ± 0.05	...
Si I	7.61	11.60 ± 0.07	[11.61]	...
Si II		14.48 ± 0.07	-2.33	15.34 ± 0.03	-0.57	15.39 ± 0.02	-1.48
Si IV		12.83 ± 0.03	...
P I	5.54	12.01 ± 0.03	[12.02]	...
P II		13.86 ± 0.03	-0.88	13.52 ± 0.06	-0.32	14.03 ± 0.03	-0.77
S I	7.26	14.64 ± 0.02	...	12.39 ± 0.10	...	14.65 ± 0.02	...
S II		>15.62	> -0.90
Cl I	5.33	14.30 ± 0.10	-0.23	11.70 ± 0.16	...	[14.30]	...
K I	5.18	12.08 ± 0.07	...	10.26 ± 0.12	...	12.09 ± 0.07	...
Ca I	6.41	9.10 ± 0.09	[9.12]	...
Ca II		11.41 ± 0.03	-4.20	11.83 ± 0.02	...	11.97 ± 0.02	> -3.70
Ti I	5.00	<10.03	<10.15	...
Ti II		10.69 ± 0.08	-3.50	11.50 ± 0.03	-1.80	11.56 ± 0.03	-2.70
V II	4.07	<11.88	< -1.39	<12.00	< -1.33
Cr I	5.72	<9.68	<9.80	...
Mn I	5.58	<10.67	<10.79	...
Mn II		<12.72	< -2.06	<12.84	< -2.00
Fe I	7.54	11.28 ± 0.15	[11.30]	...
Fe II ^d		13.81 ± 0.06	-2.93	14.37 ± 0.02	-1.47	14.48 ± 0.02	-2.32
Co II	4.98	<12.48	< -1.70	<12.60	< -1.64
Ni I	6.29	<10.68	<10.80	...
Ni II		12.59 ± 0.08	-2.90	13.15 ± 0.05	-1.44	13.26 ± 0.04	-2.29
Cu II	4.34	11.66 ± 0.11	-1.88	11.52 ± 0.11	-1.12	11.90 ± 0.14	-1.70
Zn I	4.70	12.13 ± 0.12	[12.14]	...
Zn II		12.87 ± 0.08	-1.03	12.78 ± 0.02	-0.22	13.13 ± 0.05	-0.83
Ga II	3.17	10.53 ± 0.13	-1.84	10.70 ± 0.13	-0.77	10.92 ± 0.15	-1.51

Table 3—Continued

Species	A_{\odot}^a	Main component		All other components		Total sight line	
		$\log[N_m]$	Depletion	$\log[N_o]^b$	Depletion	$\log[N]$	Depletion
Ge II	3.70	11.89±0.06	−1.01	11.94±0.11	−1.02
As II	2.40	<11.52	< −0.08	<11.64	< −0.02
Kr I	3.36	12.36±0.06	−0.20	12.41±0.11	−0.21
Cd II	1.81	10.97±0.12	−0.03	11.18±0.14	+0.12
Sn II	2.19	10.88±0.10	−0.51	10.89±0.15	−0.55
Pb II	2.13	<11.42	< +0.09	<11.54	< +0.15

Note. — Uncertainties are 1σ ; limits are 3σ . Values in square braces are estimated / assumed. For H and H₂, see Sec. 3.1. For several trace neutral species, the total is assumed to be 0.01–0.02 dex higher than the main-component value (as found for C I, Na I, S I, and K I). For O I, the total is assumed to have the same (very mild) depletion as found for the main component. See Appendix Table 10 for the absorption lines measured for each species.

^aProtosolar abundances from Lodders (2003), which are 0.07–0.08 dex higher than the current solar photospheric values. The protosolar values are adopted here to facilitate comparisons with the surveys of Jenkins (2009) and Ritchey et al. (2018).

^bTotal for all components other than the main component near 14 km s^{−1}.

^cFor $b = 1.0 \pm 0.1$ km s^{−1}. The smaller $\log[N(\text{O I})] = 17.43$ obtained by Jensen et al. (2005) was based on equivalent widths of the very strong $\lambda 1039$ and $\lambda 1302$ lines, with $b = 18.1$ km s^{−1} for the effective curve of growth.

^dThe much larger $\log[N(\text{Fe II})] = 15.45$ obtained by Snow et al. (2002a) may be due to inclusion of some stellar absorption in the equivalent widths measured in the lower resolution, lower S/N ratio *FUSE* spectra.

Table 4. Column Densities – Molecules

Molecule	$\log[N_m]$	b	Excitation
H ₂	20.81±0.21		T ₀₁ = 43±11
CH	13.54±0.04	1.0	...
CH ⁺	11.68±0.07		...
CH ₂	(<13.01)		...
C ₂	13.98±0.04	0.7	T _k = 40±5
C ₃	13.02±0.02		T _{low} = 75
	...		T _{high} = 137
CN	13.55±0.04	0.7	T ₀₁ = 2.89±0.15
	...		T ₁₂ = 2.95±0.19
¹³ CN	11.65±0.06		...
CO	16.42±0.05	0.5	T _{ex} = 11.7±0.4
¹³ CO	14.63±0.03	0.5	T _{ex} = 7.7±0.2
C ¹⁸ O	12.87±0.08		...
CO ⁺	(<12.59)		...
CS	12.12±0.03		...
NH	12.94±0.06		...
NO	(<13.86)		...
NO ⁺	(<13.54)		...
OH	14.00±0.10		T _{ex} ~ 1.7 K
OH ⁺	<12.81		...
H ₂ O	(<12.95)		...
SH ⁺	(<13.14)		...
HCl	(<11.83)		...

Note. — Data for H₂ are from Rachford et al. (2002); data for C₃ are from Ádámkóvics et al. (2003). See Appendix Tables 11 and 12 for the absorption lines measured for each species. The total column density for C₂ includes small estimated contributions from (unmeasured) levels with $J > 18$. The total column density for ¹³CN assumes the same excitation temperature as for CN. Column density limits in parentheses are based on measurements of a single line, with no information on molecular excitation (see Table 11). Absorption from C₂⁻, C₂⁺, CN⁺, SiO, SH, and AlH was not detected (Table 11), but reliable f values are not available for those transitions.

3. INTERSTELLAR COLUMN DENSITIES

3.1. H, H₂, and H_{tot}

Fits to the STIS Ly α profile, using the usual continuum reconstruction method (e.g., Savage et al. 1977; Diplas & Savage 1994), yield a total column density of atomic hydrogen $N(\text{H}) \sim 16.5 \pm 1.5 \times 10^{20} \text{ cm}^{-2}$ for the sight line. Given the spectral type assigned to HD 62542, which has ranged from B3 V to B5 V (Feast et al. 1955; Houk 1978; Cardelli & Savage 1988), however, that measured $N(\text{H})$ likely includes a significant stellar contribution (Savage & Panek 1974; Diplas & Savage 1994). Using the photometry of Kilkenny (1978), the resulting Strömgren index $[c_1] = c_1 - 0.2(b - y) = 0.364$ implies a stellar contribution of about $11 \pm 2 \times 10^{20} \text{ cm}^{-2}$ (Fig. 2 of Diplas & Savage 1994), which would then yield a total interstellar $N(\text{H}) \sim 5.5 \pm 2.5 \times 10^{20} \text{ cm}^{-2}$ toward HD 62542.

Bearing in mind that this sight line exhibits some unusual properties, additional estimates for the interstellar $N(\text{H})$ – for the sight line as a whole, for the main component, and for the sum of the other components – may be obtained from other measured quantities and the corresponding mean relationships established for the local Galactic interstellar medium (ISM). In the following (and throughout the rest of this paper), column densities without subscripts refer to the entire sight line; subscripts "m" and "o" denote values for the main component and the sum of the other components, respectively:

1. For an average Galactic gas-to-dust ratio $N(\text{H}_{\text{tot}})/E(B - V) = 5.6 \pm 1.4 \times 10^{21} \text{ cm}^{-2}$ (e.g., Bohlin et al. 1978; Welty et al. 2012), the adopted color excess, $E(B - V) = 0.35$, would suggest a total hydrogen column density $N(\text{H}_{\text{tot}}) = N(\text{H}) + 2N(\text{H}_2) \sim 20 \pm 5 \times 10^{20} \text{ cm}^{-2}$. With the $N(\text{H}_2) = 6.5_{-2.4}^{+4.0} \times 10^{20} \text{ cm}^{-2}$ derived from *FUSE* spectra (Rachford et al. 2002), that $N(\text{H}_{\text{tot}})$ would imply $N(\text{H}) \sim 7 \times 10^{20} \text{ cm}^{-2}$ – slightly higher than the value obtained from Ly α .
2. The $N(\text{CH})$ toward HD 62542 is slightly above (but consistent with) the general good correlation with $N(\text{H}_2)$ observed in the Galactic ISM (e.g., Danks et al. 1984; Rachford et al. 2002; Sheffer et al. 2008; see Fig. 10 below). Fits to the high-S/N ratio Keck CH $\lambda 4300$ profile then suggest that the main component near 14 km s^{-1} contains at least 99 percent of the CH (and H₂) toward HD 62542. The other components in the sight line thus contain primarily atomic hydrogen.
3. The equivalent width of the $\lambda 5780.6$ diffuse interstellar band is generally fairly tightly correlated with $N(\text{H})$ in the local Galactic ISM (Herbig 1993; Friedman et al. 2011), with an average $N(\text{H})/W(5780.6) = 7.0 \pm 1.8 \times 10^{18} \text{ cm}^{-2} \text{ m}\text{\AA}^{-1}$ (Welty et al. 2006, 2012). The observed $W(5780.6) = 27 \pm 3 \text{ m}\text{\AA}$ (from the average of the UVES spectra) would thus correspond to a somewhat smaller $N(\text{H}) \sim 1.9 \pm 0.5 \times 10^{20} \text{ cm}^{-2}$. [Note, however, that there are sight lines (e.g., in the Sco-Oph and Orion Trapezium regions; Herbig 1993; Welty et al.

2006, 2012) in which the $\lambda 5780.6$ DIB is weaker than would be expected from the observed $N(\text{H})$ – so $N(\text{H})$ could be higher than that.]

4. While most of the well-known DIBs (e.g., $\lambda\lambda 4428.5, 5780.6, 6283.8$) appear to trace predominantly atomic gas, the C_2 -DIBs (and, to a lesser extent, some others such as $\lambda 5797.2$) can also be present in diffuse molecular gas (Thorburn et al. 2003; Welty 2014; Welty et al. 2014; Lan et al. 2015; Fan et al. 2017). Sight lines in which primarily molecular and primarily atomic components are separated in velocity thus may exhibit velocity shifts among those DIBs – which can then provide some indication of the relative distributions (in velocity) of the molecular and atomic gas (e.g., Cox et al. 2005; Welty et al. 2014). Figure 5 compares the UVES profiles of several DIBs toward HD 62542 with the corresponding profiles seen in HARPS spectra of the similarly reddened 20 Aql (where the DIBs are among the narrowest known – and thus may exhibit the “intrinsic” DIB profiles). In the top and bottom sections of each panel, the 20 Aql profiles are aligned at 14 and 27 km s^{-1} (i.e., with the dominant main molecular component and the generally strongest of the predominantly atomic components toward HD 62542, respectively); in the middle is a composite based on equal contributions from a 20 Aql profile at each of those two velocities. While the DIBs toward HD 62542 are fairly weak, these rather crude comparisons suggest that the $\lambda 4963.9$ C_2 -DIB is nearly all in the main component at 14 km s^{-1} , the $\lambda 5797.2$ DIB is largely in that main component, and the $\lambda 6196.0$ and $\lambda 5780.6$ DIBs may have roughly equal contributions from the two components. The profiles and velocities of the DIBs toward HD 62542 thus appear to be consistent with the H_2 being concentrated in the main 14 km s^{-1} component and with the total H being divided roughly equally between that main component and the other components (together, which are seen only in the atomic lines).

5. In the Galactic ISM, the column density of Na I exhibits a nearly quadratic dependence on $N(\text{H}_{\text{tot}})$ (Welty & Hobbs 2001), so that the total $N_{\text{o}}(\text{Na I}) \sim 11.9 \times 10^{11} \text{ cm}^{-2}$ for all the other components (Tables 2 and 3) suggests $N_{\text{o}}(\text{H}) \sim 2.5 \pm 0.6 \times 10^{20} \text{ cm}^{-2}$ for those components. The depletion indicators $\log[N(\text{Ca II})/N(\text{Na I})]$ and $\log[N(\text{Ti II})/N(\text{H}_{\text{tot}})]$ are also fairly well correlated ($r = 0.87$) in the Galactic ISM (D. E. Welty & P. A. Crowther, in preparation). The column densities of Na I, Ca II, and Ti II for all the other components then yield a very similar estimate for $N_{\text{o}}(\text{H}) \sim N_{\text{o}}(\text{H}_{\text{tot}}) \sim 2.4 \times 10^{20} \text{ cm}^{-2}$.

6. If the pattern of elemental depletions is similar to that generally found in the Galactic ISM, then an estimate for $N(\text{H}_{\text{tot}})$ may be obtained from the observed column densities of various dominant ions and the average elemental depletion coefficients derived by Jenkins (2009; eqn. 24a; see Sec. 4.3 below). Figure 6 shows the application of this procedure to the main component toward HD 62542 (left panel) and to the other components (right panel). In each case, the depletion strength factor F_* is given by the slope of the fitted line, and the estimated $\log[N(\text{H}_{\text{tot}})]$ is given by the y value at $x = 0$. For the main component toward HD 62542, the pattern of depletions is somewhat unusual (Sec. 4.3), and the observed column densities yield an estimated $N_{\text{m}}(\text{H}_{\text{tot}}) \sim 18_{-6}^{+10} \times 10^{20} \text{ cm}^{-2}$, with $F_* = 1.52 \pm 0.19$. On the whole, the

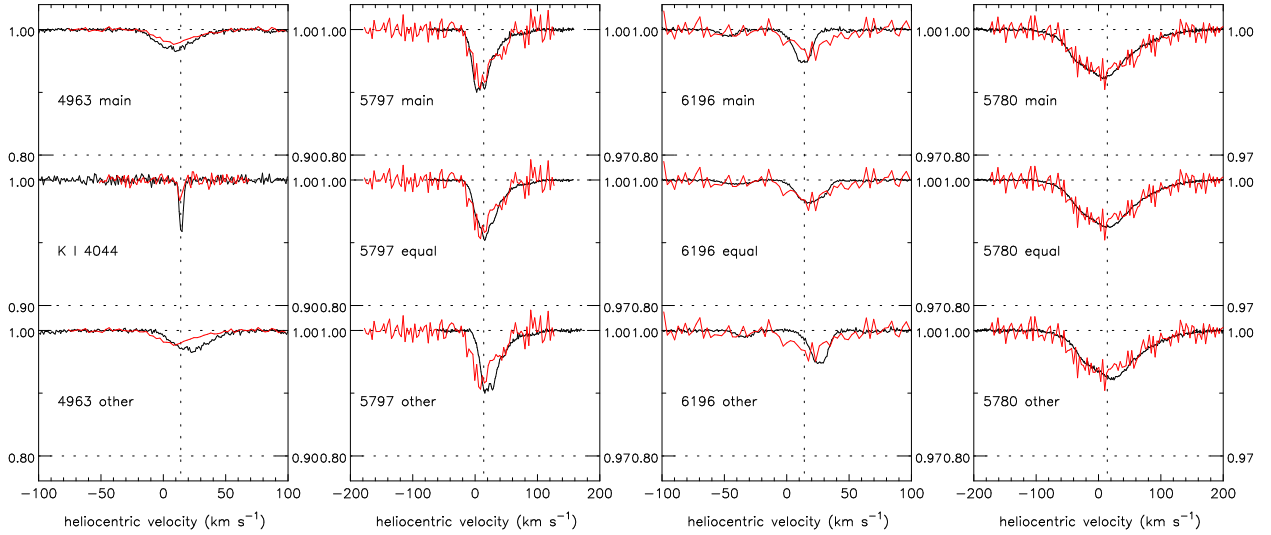


Fig. 5.— Velocity shifts of several DIBs toward HD 62542 (red; UVES spectra), relative to those toward 20 Aql (black; HARPS spectra), scaled to similar central depths [note the different y-axis scales for HD 62542 (right) and 20 Aql (left)]. On the top line of each panel, the 20 Aql profile is shifted to 14 km s^{-1} (the velocity of the main, predominantly molecular component toward HD 62542); on the bottom line of each panel, the 20 Aql profile is shifted to 27 km s^{-1} (the velocity of the generally strongest of the predominantly atomic "other" components); in the middle is a composite constructed from the 20 Aql profile, with equal contributions at 14 and 27 km s^{-1} (except in the left-most panel, which compares the aligned K I $\lambda 4044$ profiles). Toward HD 62542, the $\lambda 4963.9$ C₂-DIB (which can be present in diffuse molecular gas) appears to be concentrated almost exclusively in the main component, the $\lambda 5797.2$ DIB appears to have some contribution from the higher velocity component, and the $\lambda 6196.0$ and $\lambda 5780.6$ DIBs (which trace primarily atomic gas) appear to have roughly equal contributions from the two components.

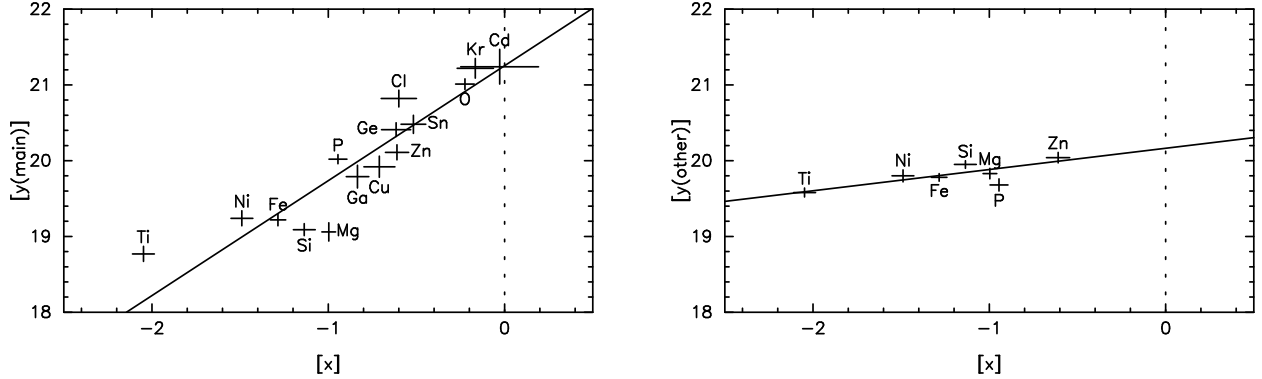


Fig. 6.— Application of equation 24a from Jenkins (2009), used to estimate the depletion strength factor F_* and $N(\text{H}_{\text{tot}})$ from the relative depletions of various species, for the main component toward HD 62542 (left panel) and the other components (right panel). The y values are derived from the column densities of dominant species listed in Table 3, the proto-solar abundances from Lodders (2003), and the coefficients derived by Jenkins (2009) and Ritchey et al. (2018). The x values are the corresponding A_X coefficients from the latter two references. The depletion factor is given by the slope of the fitted line: 1.52 ± 0.19 for the main component and 0.28 ± 0.10 for the other components. The estimate for $\log[N(\text{H}_{\text{tot}})]$ is given by the y value of the line at $x = 0.0$: 21.25 ± 0.19 for the main component and 20.16 ± 0.13 for the other components.

depletions corresponding to the sum of all of the other components are slightly more severe than the Galactic warm cloud pattern, and the observed column densities yield an estimated $N_o(\text{H}_{\text{tot}}) \sim N_o(\text{H}) \sim 1.4 \pm 0.5 \times 10^{20} \text{ cm}^{-2}$, with $F_* = 0.28 \pm 0.10$. We note, however, that application of this procedure to the sum of all the components toward HD 62542 – combining components with very different depletion properties – yields $F_* = 0.85 \pm 0.11$ (slightly less severe than the Galactic cold cloud pattern) and an estimated $N(\text{H}_{\text{tot}}) \sim 11.5_{-3.0}^{+4.0} \times 10^{20} \text{ cm}^{-2}$ – which is smaller than the sum of $N_m(\text{H}_{\text{tot}})$ and $N_o(\text{H}_{\text{tot}})$; see the discussion in Sec. 4.3 below.

In view of these various estimates for the column densities of H, H_2 , and H_{tot} , we have adopted $N(\text{H}) = 5 \pm 2 \times 10^{20} \text{ cm}^{-2}$ [from Ly α and $W(5780.6)$], with $\sim 2 \times 10^{20} \text{ cm}^{-2}$ in the other components (all together, from Na I and the depletions) and the remainder ($\sim 3 \times 10^{20} \text{ cm}^{-2}$) in the main component (Table 5). The total hydrogen column density for the sight line is then $N(\text{H}_{\text{tot}}) = 18 \pm 7 \times 10^{20} \text{ cm}^{-2}$, with $16 \times 10^{20} \text{ cm}^{-2}$ in the main component. If $N_m(\text{H})$ is of order $3 \times 10^{20} \text{ cm}^{-2}$ in the main component, then $f(\text{H}_2) \sim 0.81$ there (consistent with the estimate of Ádámkóvics et al. 2005, which was based on more limited data). The molecular fraction in the other components is $\lesssim 0.06$.

Table 5. Estimates for the Column Densities of Atomic, Molecular, and Total Hydrogen

Indicator	Main component			All other components			Total sight line		
	$N_m(\text{H})$	$N_m(\text{H}_2)$	$N_m(\text{H}_{\text{tot}})$	$N_o(\text{H})$	$N_o(\text{H}_2)$	$N_o(\text{H}_{\text{tot}})$	$N(\text{H})$	$N(\text{H}_2)$	$N(\text{H}_{\text{tot}})$
Lyman α (STIS)	5.5 ± 2.5	...	(19 ± 7)
H ₂ (FUSE)	6.5 ± 3.2	...
$E(B - V)$	(~ 7)	...	20 ± 5
$N_r(\text{Na I})$	(2.5 ± 0.6)	...	2.5 ± 0.6
$N_r(\text{Na I, Ca II, Ti II})$	(2.4 ± 0.6)	...	2.4 ± 0.6
$W(5780.6)$	$\gtrsim 1.9 \pm 0.5$...	$(\gtrsim 15 \pm 6)$
Diffuse band profiles	$\sim 0.5N(\text{H})$	$\sim 0.5N(\text{H})$
Depletions	(~ 5)	...	18_{-6}^{+10}	(1.4 ± 0.5)	...	1.4 ± 0.5	(~ 6)	...	(19 ± 8)
$N(\text{CH})$...	6.5 ± 3.2	< 0.06
Adopt	3 ± 1	6.5 ± 3.2	16 ± 6	2.0 ± 0.5	< 0.06	2.0 ± 0.5	5 ± 2	6.5 ± 3.2	18 ± 7

Note. — All column densities are $\times 10^{20} \text{ cm}^{-2}$. Values in parentheses for atomic or total hydrogen use the observed $N(\text{H}_2)$ and the estimated total or atomic hydrogen column densities, respectively.

Table 6. Component Ratios (Atomic Species)

Comp	v	Na I/Ca II tm/ds	Mg I/Mg II ts/ds	Mg II/Si II ds/ds	Si II/Zn II ds/dm	P II/Zn II dm/dm	Ti II/Zn II ds/dm	Fe II/Zn II ds/dm	Fe II/Ni II ds/ds
1	4.3	< 2.5	...	< 2.20	> 813	> 50	> 4.0
2	8.5	< 0.9	0.009:	0.56:	1450 ± 1040	< 108.3	0.18 ± 0.16	150 ± 102	21.0:
3	11.6	1.3 ± 0.3	0.007:	0.31:	1021 ± 470	< 48.9	0.27 ± 0.13	240 ± 107	14.2 ± 4.3
4	14.2	426.4 ± 82.5	0.251 ± 0.067	0.86 ± 0.25	41 ± 10	9.9 ± 2.0	0.007 ± 0.002	9 ± 2	16.7 ± 3.6
5	18.0	0.2 ± 0.1	0.0012 ± 0.0004	0.89 ± 0.18	445 ± 50	9.6 ± 3.0	0.074 ± 0.009	51 ± 5	11.4 ± 1.7
6	22.0	1.1 ± 0.2	0.0032 ± 0.0012	0.82 ± 0.31	304 ± 59	< 8.1	0.034 ± 0.011	26 ± 5	20.4 ± 9.8
7	24.0	1.5 ± 0.3	< 0.003	0.63 ± 0.42	393 ± 121	13.5 ± 5.5	0.062 ± 0.021	49 ± 12	14.9 ± 5.4
8	27.3	6.1 ± 0.3	0.0037 ± 0.0005	0.76 ± 0.13	258 ± 35	5.3 ± 0.8	0.027 ± 0.003	20 ± 2	22.7 ± 4.6
9	32.3	1.5 ± 0.5	< 0.006	0.55 ± 0.51	511 ± 120	< 25.8	0.16 ± 0.03	67 ± 12	24.4 ± 16.5

Note. — The two-letter codes in the second line of the header crudely characterize the ionization and depletion behavior of each species: t = trace, d = dominant, m = mild depletion, s = severe depletion. Pairs with similar behavior generally have similar ratios for all components, while pairs with different behavior generally exhibit different ratios for the main component (in bold) and for the other components. Colons denote very uncertain values.

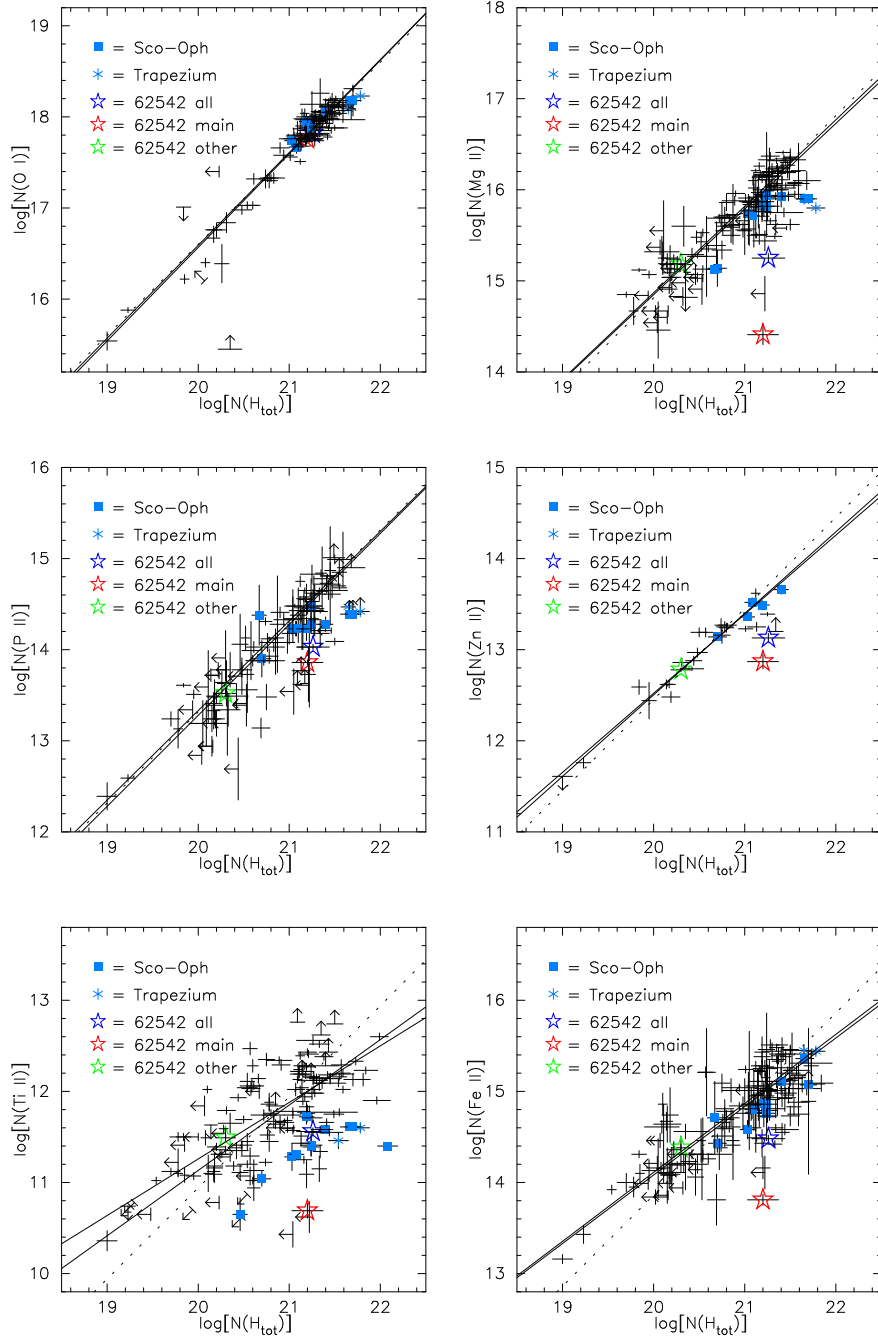


Fig. 7.— Column densities of dominant species O I, Mg II, P II, Zn II, Ti II, and Fe II vs. $N(H_{\text{tot}})$ for Galactic sight lines. The stars denote the sight line toward HD 62542: red = main (14 km s^{-1}) component; green = all other components; blue = all components. The solid lines show weighted and unweighted fits to the data (not including the Sco-Oph and Trapezium sight lines); the dotted lines have slope = 1. Toward HD 62542, the column densities of all but O I are clearly deficient, relative to the general Galactic trends – reflecting the enhanced depletions of those species in this unusual sight line. The column densities for Mg II and for the more refractory Ti II and Fe II are particularly low in the main component – indicating very severe depletions there; P II and Zn II also lie below the general trends. Note also the lower abundances of Ti II in the Sco-Oph sight lines (Welty & Crowther 2010).

3.2. Atomic Species

The combination of optical and UV spectra obtained for HD 62542 has yielded detections or useful limits for many neutral and singly ionized atomic species. For the species with potentially detectable lines covered by those spectra, Table 3 lists both the total column densities and (where discernible) the separate contributions from the main component and from the sum of all the other components, as derived from either the detailed profile fits or the AOD integrations. The table also lists values for elemental depletions, based on the adopted $N(\text{H}_{\text{tot}})$, the column densities of the dominant ions in predominantly neutral gas, and the protosolar abundances given by Lodders (2003). We have adopted the recommended protosolar abundances – which are 0.07–0.08 dex higher than the current solar values – to facilitate comparisons with the depletion parameters determined in the recent abundance surveys of Jenkins (2009) and Ritchey et al. (2018). Figures 7 and 8 show the total column densities of a few of the singly ionized and neutral atomic species (respectively), versus $N(\text{H}_{\text{tot}})$, in relation to the general trends for those species found for the local Galactic ISM. The Galactic data have been drawn from a number of sources: for Na I, C I, and H_{tot} (Welty & Hobbs 2001; Jenkins 2009; Jenkins & Tripp 2011; Welty et al. 2016); for Ca I and Fe I (Welty et al. 2003); for Ti II (Welty & Crowther 2010); for Fe II, P II, and Zn II (Jenkins 2009); and references therein; an updated compilation is maintained at <http://astro.uchicago.edu/~dwelty/coldens.html>. Some sight lines in the Sco-Oph and Orion Trapezium regions exhibit lower abundances of some trace neutral species (Welty & Hobbs 2001) and/or enhanced depletions of some refractory elements (e.g., Welty & Crowther 2010), and are noted with blue squares and blue asterisks, respectively. In several cases, the sight line toward HD 62542 (blue star) stands apart from the general trends – due largely to the unusual characteristics of the main (14 km s^{-1}) component (red star); the abundances in the other components (green star) are more similar to those in the general Galactic ISM. Differences in the absorption-line profiles of the various atomic species toward HD 62542 (Fig. 2) reflect those component-to-component differences in abundances – which are due to differences in ionization, depletion, and/or other local physical conditions – and/or (in some cases) the saturation of specific lines. Some column density ratios illustrating the effects of those differences for the individual components are given in Table 6 and are discussed in the following sections.

3.2.1. Dominant Species

For dominant ions in predominantly neutral atomic or molecular gas, the slopes of the relationships between $N(X)$ and $N(\text{H}_{\text{tot}})$ seen in Figure 7 reflect (to some degree) the depletion behavior of those species. For the typically mildly depleted oxygen, for example, the slope ~ 1.0 suggests that the depletion generally does not become much more severe at higher $N(\text{H}_{\text{tot}})$ (where there might be expected to be larger fractions of colder, denser gas). For the more severely depleted Ti and Fe, however, the slopes < 1.0 suggest that the depletions of those species do become increas-

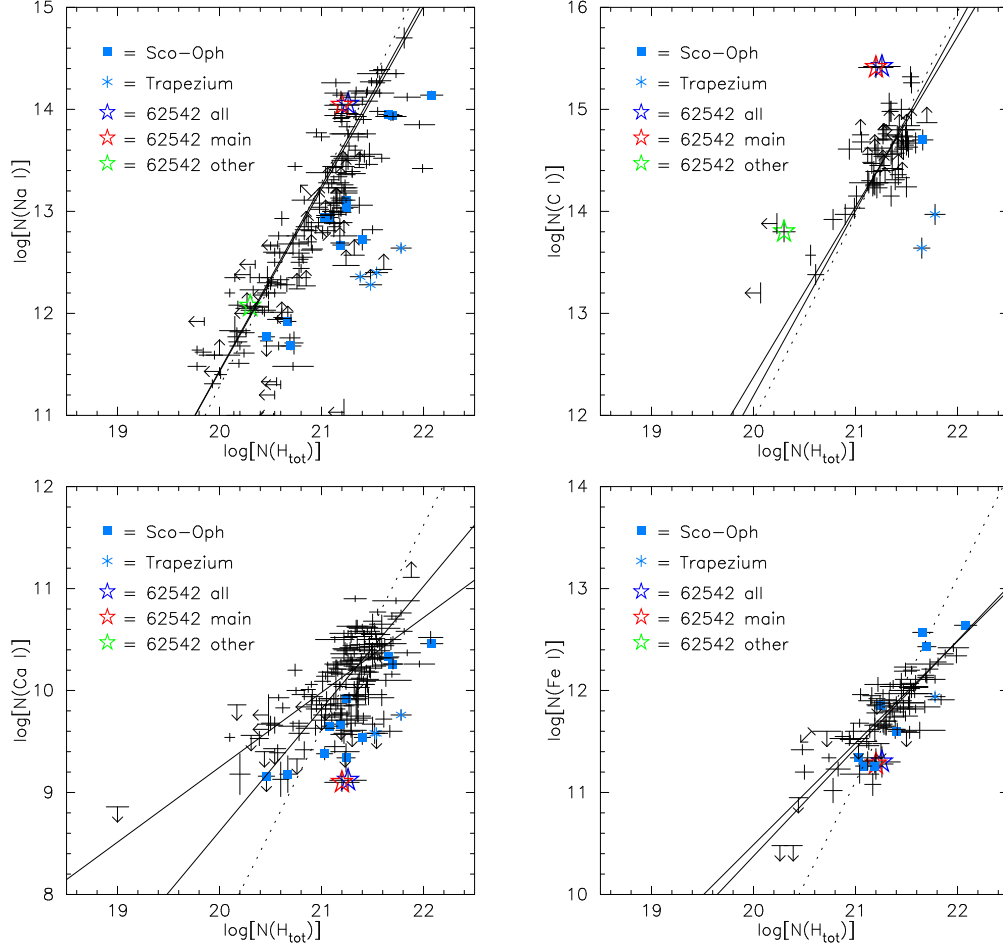


Fig. 8.— Column densities of trace neutral species Na I, C I, Ca I, and Fe I vs. $N(\text{H}_{\text{tot}})$ for Galactic sight lines. The stars denote the sight line toward HD 62542: red = main (14 km s^{-1}) component; green = all other components; blue = all components. The solid lines show weighted and unweighted fits to the data (not including the Sco-Oph and Trapezium sight lines); the dotted lines have slope = 2 (as would be expected from considerations of ionization balance). Toward HD 62542, $N(\text{Na I})$ is consistent with the general Galactic relationship, $N(\text{C I})$ is somewhat enhanced, and $N(\text{Ca I})$ and $N(\text{Fe I})$ are deficient – reflecting the specific ionization and depletion behavior of each of those species in this unusual sight line (see Sec. 4.3.3). The lower abundances of the trace neutral species in most of the Sco-Oph and Trapezium sight lines may be due to stronger than average radiation fields there (e.g., Welty & Hobbs 2001).

ingly severe at higher overall column densities.⁵ The observed differences in absorption-line profiles (right-hand panel of Fig. 2) then primarily reflect differences in those elemental depletions in the various individual components. For example, the profiles for the typically mildly depleted P II and Zn II, the typically moderately to severely depleted Mg II and Si II, and the typically more severely depleted Fe II and Ni II exhibit similarities within each pair (most obviously for lines of similar strength), but differences relative to the other pairs. Those qualitative indications are confirmed by the detailed fits to the line profiles (Table 2) and by the resulting component-by-component ratios listed in Table 6. For the mildly depleted P II and Zn II, the strongest absorption is in the main component near 14 km s⁻¹; for Mg II and Si II, the strongest absorption is in the components near 18 and 27 km s⁻¹; for the severely depleted Fe II and Ni II, the strongest absorption is spread over several components, near 12, 14, 18, and 27 km s⁻¹. While the column densities of the typically similarly depleted elements within each of those three pairs track each other fairly well, the ratios for species with different depletion properties exhibit significant variations. In the main (14 km s⁻¹) component, for example, the $N_m(\text{Si II})/N_m(\text{Zn II})$ and $N_m(\text{Fe II})/N_m(\text{Zn II})$ ratios are much lower, compared to the corresponding (and more similar) values in all the other components. As the Mg II $\lambda\lambda 1239,1240$ lines are significantly weaker than the Si II $\lambda 1808$ line, the roughly constant ratio of the column densities of Mg II and Si II – both toward HD 62542 and in other Galactic sight lines (e.g., Fitzpatrick 1997; Cartledge et al. 2006) – also provides some corroboration for the apparent relative insensitivity of the main component $N_m(\text{Si II})$ to the b value adopted in the fits. Toward HD 62542, the column densities of some of the dominant ions of depleted elements (e.g., Ti II, Fe II) fall well below the general trends versus $N(\text{H}_{\text{tot}})$ seen in the local Galactic ISM – both for the sight line as a whole and (especially) for the main component (lower two panels of Fig. 7).

In principle, the weak semiforbidden $\lambda 2325$ C II] and $\lambda 2335$ Si II] lines can provide accurate gas-phase column densities for those two species – thus providing important constraints on the composition of interstellar dust grains (e.g., Sofia et al. 2004; Miller et al. 2007). Both lines are covered in our STIS E230H spectra, but neither is convincingly detected toward HD 62542 at the S/N ratios achieved in that wavelength range. While there are weak possible absorption features near the expected positions of both of the lines in the summed spectra, the equivalent widths of those weak features are less than 3σ , they do not appear in all of the individual exposures, and their velocities do not agree with the velocities of the strongest component(s) seen for similarly distributed species. For Si II, the column densities listed in Table 3, based on the detailed fits to the $\lambda 1808$ line, are consistent with the limits derived from the nondetection of the $\lambda 2335$ line. For C II, the interstellar absorption from the strong $\lambda 1334$ line is buried in the core of the strong stellar C II line, and it is thus very difficult to obtain column densities for C II directly. A rough estimate of $N_m(\text{C II})$ in the main component may be obtained, however, from the adopted $N_m(\text{H}_{\text{tot}})$ and the carbon depletion predicted for the depletion index $F_* \sim 1.5$ found for that component. For the

⁵While the slope for zinc also appears to be < 1.0 , at least part of that trend may be due to underestimation of $N(\text{Zn II})$ at the higher $N(\text{H}_{\text{tot}})$, where the only two detectable Zn II lines (at 2026.1 and 2062.7 Å) can be significantly saturated.

depletion coefficients for carbon derived by Jenkins (2009), $N_{\text{m}}(\text{C II})$ would be of order $2.5 \times 10^{17} \text{ cm}^{-2}$ – well below the upper limit obtained from the nondetection of the $\lambda 2325$ line.

3.2.2. Trace Neutral Species

The moderately high $N(\text{H}_{\text{tot}})$ toward HD 62542, the steep far-UV extinction, and the quality and coverage of the optical and UV spectra have also yielded detections or fairly stringent limits for a number of trace neutral species – primarily in the main component at 14 km s^{-1} . The column densities of C I, Na I, Mg I, and S I, and the ratio of the column densities of Mg I and Mg II, for example, are more than an order of magnitude higher in the main component than in the other components (Tables 2, 3, and 6). In the local Galactic ISM, the column densities of trace neutral ions of mildly depleted elements (e.g., C I, Na I, K I) exhibit nearly quadratic relationships with $N(\text{H}_{\text{tot}})$, while the corresponding relationships for the neutral ions of more severely depleted elements (e.g., Ca I, Fe I) are somewhat shallower (Welty & Hobbs 2001; Welty et al. 2003; Fig. 8). Toward HD 62542, the column densities of Na I, Mg I, Si I, K I, and Cl I appear fairly "normal", relative to those local Galactic trends; the column densities of C I, P I, S I, and Zn I are somewhat enhanced; and the column densities of Ca I and Fe I are somewhat deficient (upper and lower panels of Fig. 8) – though the currently available samples for Mg I, Si I, P I, and Zn I are fairly small.⁶ As discussed below (Sec. 4.3), the observed abundances of the trace neutral species toward HD 62542 – and the deviations of some of them from the general Galactic trends – reflect both the ionization behavior and the depletion behavior of those species in the main component.

3.2.3. Higher Ions

Interstellar absorption from several of the commonly observed more highly ionized species is also detected in our STIS spectra of HD 62542 (Fig. 9). Fits to the line profiles suggest that Al III has components at 7 and 26 km s^{-1} , with $b \sim 3.3$ and 7.0 km s^{-1} , respectively, and Si IV has components at –4, 5, and 27 km s^{-1} , with $b \sim 3.3, 6.9, 5.3 \text{ km s}^{-1}$, respectively; the total column densities for those higher ions are listed in Table 3. Any absorption from interstellar Si III is blended with a strong stellar line, however, and neither the C IV $\lambda\lambda 1548, 1550$ doublet nor the $\lambda 1190$ S III line is covered by our STIS spectra.

⁶To our knowledge, column densities for P I and Zn I have not previously been reported. The values referenced here are from measurements of absorption from those trace neutral species seen in archival *HST* spectra (D. E. Welty, in preparation).

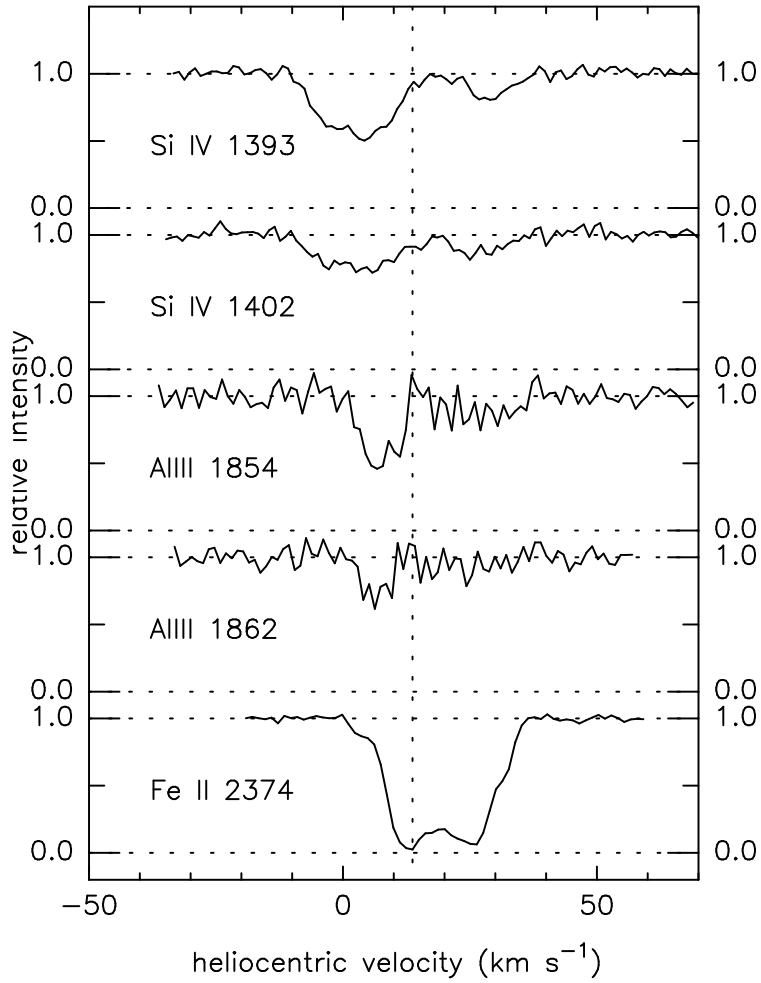


Fig. 9.— Normalized spectra of the $\lambda\lambda 1393, 1402$ Si IV and $\lambda\lambda 1854, 1862$ Al III lines toward HD 62542. The profile of the $\lambda 2374$ line of Fe II (the dominant form of Fe in primarily neutral gas) is shown for comparison. The absorption from the higher ions is not detected for the main neutral gas component near 14 km s^{-1} , but does overlap in velocity with the absorption from the other, weaker neutral gas components.

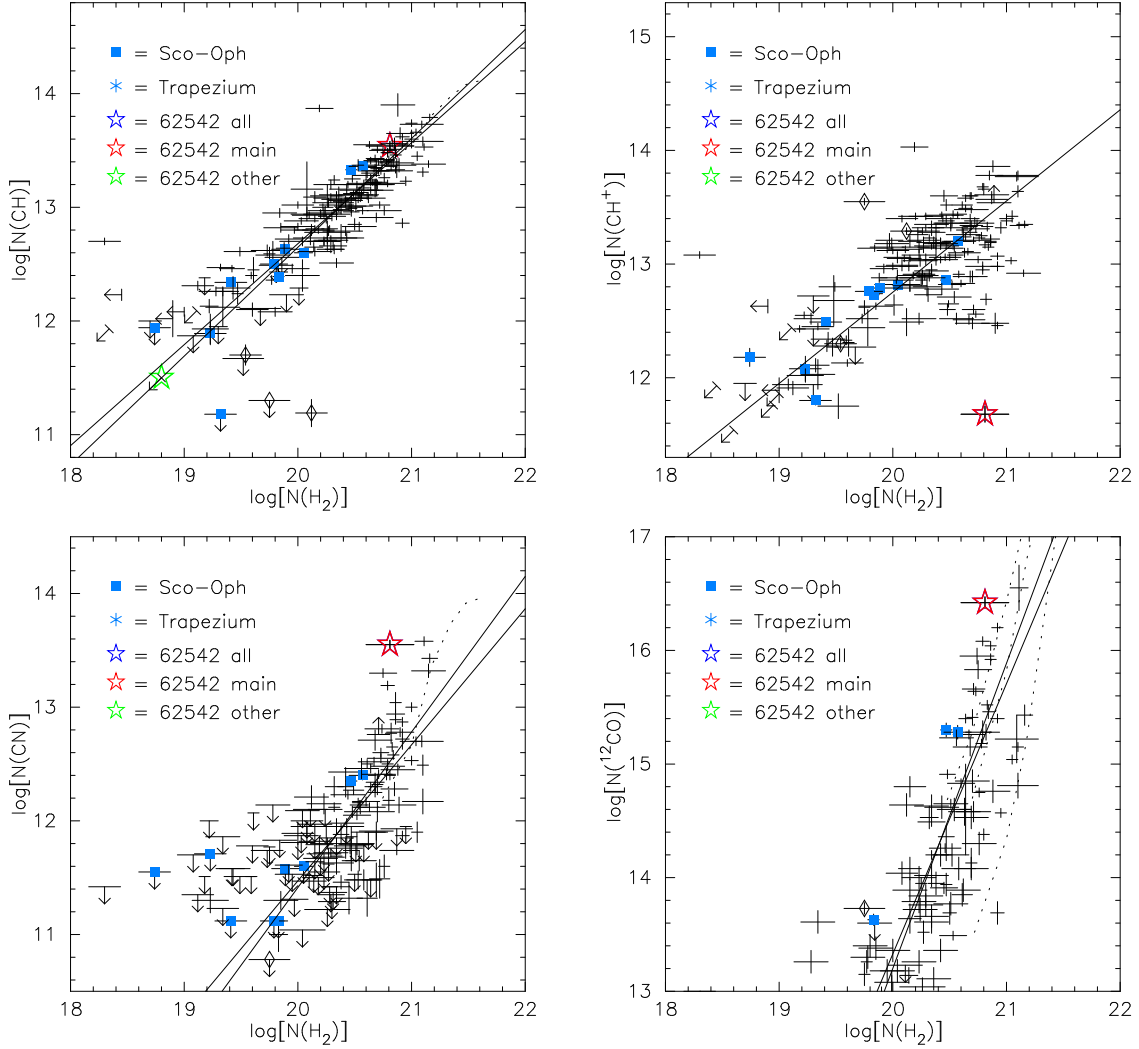


Fig. 10.— Column densities of CH, CH⁺, ¹²CO, and CN vs. $N(\text{H}_2)$, for Galactic sight lines. The large red star denotes the sight line toward HD 62542 (main component); the open diamonds denote Pleiades sight lines. The solid lines show weighted and unweighted fits to the data; the dotted lines represent the models of van Dishoeck & Black (1988, 1989); the three models for ¹²CO are (left to right) for $I_{\text{UV}} = 0.5, 1.0,$ and 10 times the average local Galactic radiation field. Relative to the mean trends with $N(\text{H}_2)$, $N_{\text{m}}(\text{CH})$ is “normal” toward HD 62542, $N_{\text{m}}(\text{CH}^+)$ is very low, and $N_{\text{m}}(^{12}\text{CO})$ and $N_{\text{m}}(\text{CN})$ are high.

3.3. Molecular Species

The available optical and UV spectra of HD 62542 have also yielded detections of a number of molecular species (H_2^* , CH, CH^+ , C_2 , C_3 , ^{12}CN , ^{13}CN , ^{12}CO , ^{13}CO , C^{18}O , CS, NH, OH), as well as limits for some others (CH_2 , C_2^+ , C_2^- , CN^+ , CO^+ , NO, NO^+ , OH^+ , H_2O , SiO, SH, SH^+ , HCl, AlH). All of the molecular species are found only in the main (14 km s^{-1}) component (Fig. 3). As noted above, fits to the high-S/N ratio Keck spectrum of the strong CH $\lambda 4300$ line yield a $3\text{-}\sigma$ upper limit of order $3 \times 10^{11} \text{ cm}^{-2}$ for the other components [i.e., less than 1% of $N_{\text{m}}(\text{CH})$], and so we take $N = N_{\text{m}}$ for the various molecular species. Table 4 lists the main-component column densities for those molecular species, derived from the AOD integrations over the line profiles and/or from detailed fits to the profiles, together with (in several cases) the b values obtained in the fits and the excitation temperatures derived from the relative rotational populations. Comparisons of the molecular column densities seen toward HD 62542 with general trends found in the local Galactic ISM reveal some distinct differences – e.g., the very low CH^+/CH ratio and the very high CN/CH and C_3/C_2 ratios known from previous studies (Cardelli et al. 1990; Gredel et al. 1991, 1993; Ádámkóvics et al. 2003). For example, the weak absorption now detected for the CH^+ $\lambda 4232$ line (Fig. 3) indicates that $N_{\text{m}}(\text{CH}^+)$ is lower by a factor of ~ 40 than for other sight lines with comparable $N(\text{H}_2)$ (Fig. 10). While the abundances of CH, OH, and CS toward HD 62542 are fairly typical, relative to H_2 , the column densities of C_2 , C_3 , NH, ^{12}CO , ^{13}CO , and (especially) CN – all of which trace somewhat denser gas – are higher than those found for other sight lines with similar $N(\text{H}_2)$ (Fig. 10).

H_2^* : A few weak lines from the lower rotational levels of the B-X (0,3) and (0,4) bands of vibrationally excited H_2 are detected in the UV spectra (Table 11). Fits to the line profiles indicate that the lines are fairly narrow ($b \sim 1.4 \text{ km s}^{-1}$) and are found at the velocity ($13.7 \pm 0.6 \text{ km s}^{-1}$) of the main cloud (Fig. 3) – as seems to be the case for the few other sight lines in which H_2^* absorption has been detected in high-resolution UV spectra [HD 37021 (Abel et al. 2016); HD 37061 (Gnaciński 2009); HD 37903 (Meyer et al. 2001); ρ Oph D (Gnaciński 2013)]. While H_2^* can be produced either by shocks or by radiative pumping (e.g., Shull & Beckwith 1982), the relatively small b value and the lack of velocity offset (relative to the other molecular species) suggest that the H_2^* is excited radiatively in relatively cool gas, rather than by shocks. The H_2^* excitation in the main component toward HD 62542 (Figure 11) is qualitatively similar to that seen toward HD 37903 (Meyer et al. 2001; Gnaciński 2011) and ρ Oph D (Gnaciński 2013) – for each vibrational level (v), the normalized populations in the lowest even- J (para) levels are higher than those in the lowest odd- J (ortho) levels, but with similar slopes (and thus similar excitation temperatures) for both even and odd J . As the column densities of the detected individual H_2^* rotational levels are typically $5\text{--}25 \times 10^{11} \text{ cm}^{-2}$, the vibrationally excited H_2 comprises only a small fraction of the total H_2 .

C_2 : Six C_2 bands are detected: the A-X (3,0), (2,0), and (1,0) bands near 7719, 8757, and 10143 Å, respectively; the D-X (0,0) band near 2313 Å; and the F-X (1,0) and (0,0) bands near 1314 and 1341 Å, respectively. Fits to the relatively strong, well-separated lines of the D-X (0,0) band

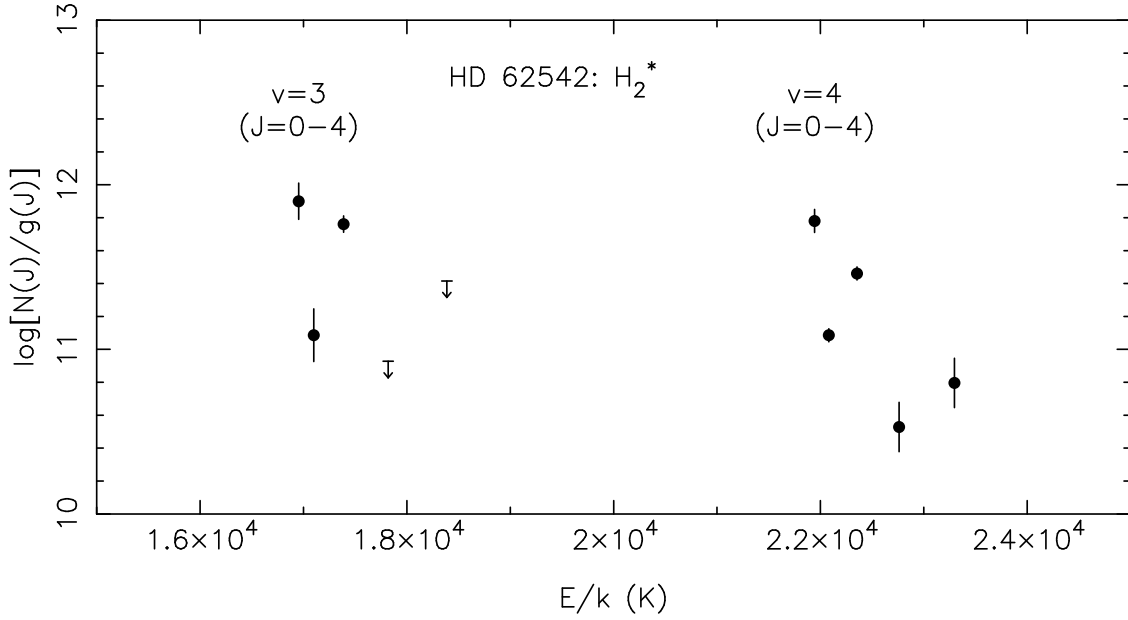


Fig. 11.— Normalized rotational populations for vibrational levels $v = 3$ and 4 of H_2^* toward HD 62542. Only a few weak lines, from rotational levels $J = 0-4$, are detected (in the main component). The excitation is qualitatively similar to that seen toward HD 37903 and HD 147888 – for each v , the normalized populations of the even- J levels lie above those for the odd- J levels, but with similar slopes (and thus similar excitation temperatures) for both.

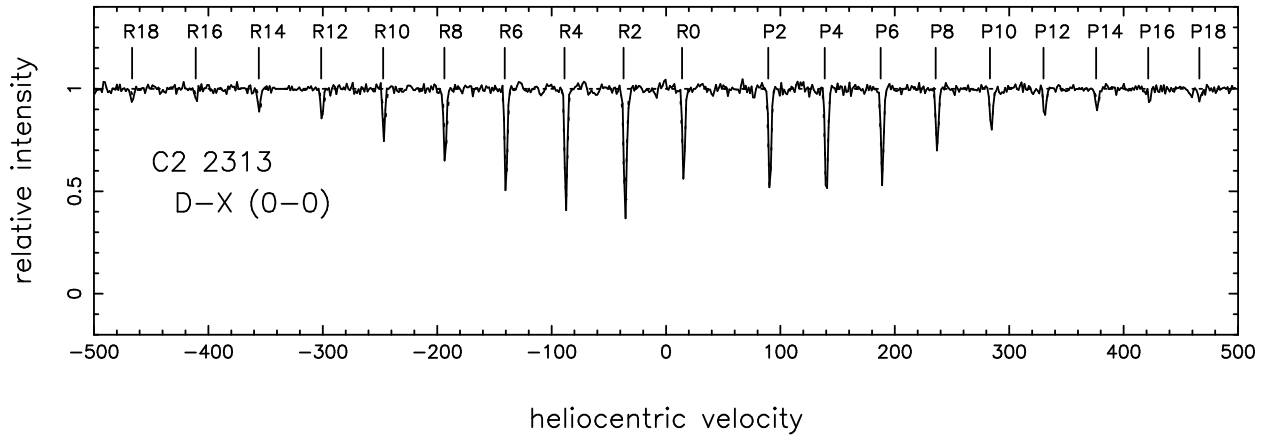


Fig. 12.— Normalized spectrum of the C_2 D-X (0-0) band near 2313 \AA toward HD 62542. The solid line is the observed spectrum; the dotted line is the fit for $b = 0.7 \text{ km s}^{-1}$. Absorption from rotational levels $J = 0-18$ (even J only) may be discerned.

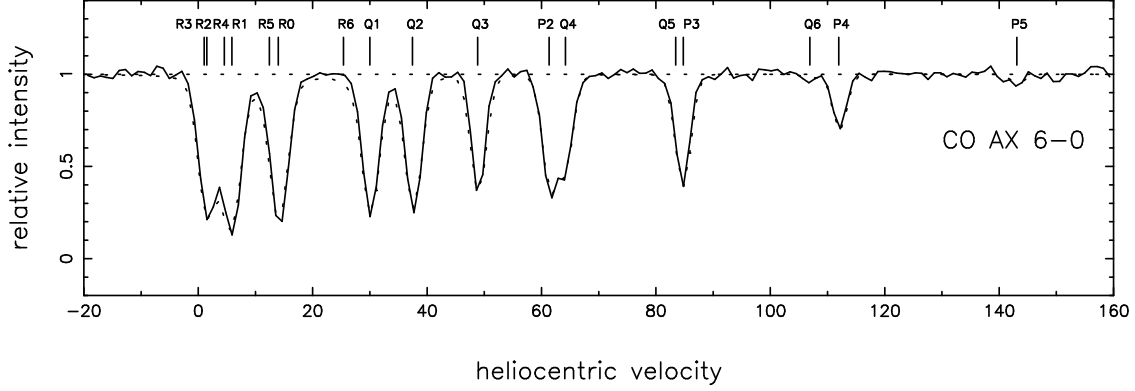


Fig. 13.— Normalized spectrum of the ^{12}CO A-X (6-0) band near 1367 \AA toward HD 62542. The solid line is the observed spectrum; the dotted line is the fit for $b = 0.5 \text{ km s}^{-1}$. Absorption from rotational levels $J = 0-6$ may be discerned.

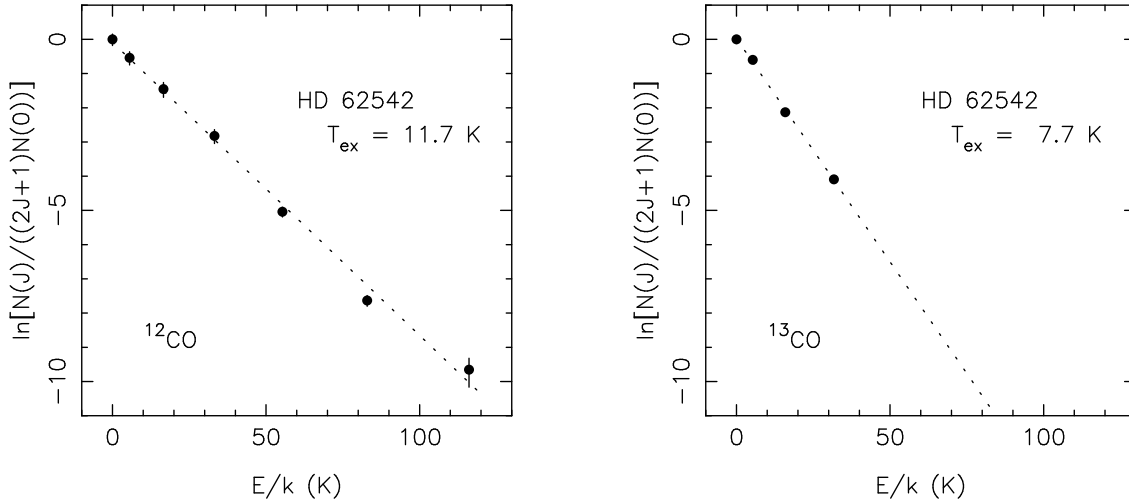


Fig. 14.— Rotational excitation of ^{12}CO (left) and ^{13}CO (right) toward HD 62542. The lines represent fits to all detected rotational levels. For both species, the corresponding excitation temperatures are both independent of rotational level and higher than the 3–5 K values typically seen in the Galactic ISM.

(Fig. 12) yield the best characterization of the rotational populations, with well-determined column densities for rotational levels $J = 0-18$ (even J only; Appendix Table 11). Fits to the weaker A-X (2,0) and (3,0) bands yield slightly lower column densities (for $J=0-8$), but the relative $N_m(J)$ are similar to those found for the D-X (0,0) band. Fits to the F-X (1,0) band yield column densities lower by about 30% (for $J=0-14$), but (again) the relative $N_m(J)$ are similar to those found for the D-X (0,0) band. Perturbations affect the positions and/or relative strengths of some of the lines in the F-X (0,0) band (Hupe et al. 2012), and there may be blending with stellar absorption around the R-branch "pile-up" near 1341.4 Å. The total $N_m(\text{C}_2) = 9.5 \times 10^{13} \text{ cm}^{-2}$ includes contributions from undetected higher rotational levels, estimated using the temperature $T_k = 40 \text{ K}$ and density of collision partners $n_c = n_{\text{H}} + n_{\text{H}_2} = 250 \text{ cm}^{-3}$ derived from the observed $J = 0-18$ levels (see Sec. 4.1.2 below). Previously available measurements of the C₂ A-X (2,0) band (Gredel et al. 1993) included only $J=0-8$, so that T_k and n_c were not as well constrained.

CN: Three CN bands are detected in the optical spectra: the B-X (1,0) and (0,0) bands, near 3580 and 3875 Å, respectively; and the A-X (2,0) band near 7906 Å (Appendix Table 11). Lines from $J=0$ and 1 are detected in all three bands, and weak lines from $J=2$ are detected in the strong B-X (0,0) band. In the main cloud toward HD 62542, the CN excitation temperature $T_{01} = 2.89 \pm 0.15 \text{ K}$ (Table 4) is slightly higher than both the $2.725 \pm 0.002 \text{ K}$ expected from excitation by the cosmic microwave background radiation (CMBR; Mather et al. 1999) and the average value $2.754 \pm 0.002 \text{ K}$ for 11 Galactic sight lines in the sample of Ritchey et al. (2011). The even-higher $T_{01} = 3.7 \pm 0.4 \text{ K}$ found by Cardelli et al. (1990) was likely due to the higher b value adopted for CN in that study (see also Gredel et al. 1991; Palazzi et al. 1992). For ¹³CN, only absorption from $J = 0$ is reliably detected; the total column density is estimated assuming the same excitation temperature found for the more abundant ¹²CN. With that assumption, the ratio $N_m(^{12}\text{CN})/N_m(^{13}\text{CN}) \sim 79 \pm 13$ is consistent with (but perhaps slightly higher than) the average local Galactic ratio $^{12}\text{C}/^{13}\text{C} \sim 70$ (e.g., Stahl & Wilson 1992; Sheffer et al. 2002b).

CO: A number of CO bands, from several isotopologs, are detected in the UV spectra (Appendix Table 13 and Figs. 25 and 26): for ¹²CO, nine of the permitted A-X bands ((4,0) through (12,0)) and some of the much weaker intersystem bands (Morton & Noreau 1994; Sheffer et al. 2002a; Eidelsberg & Rostas 2003); for ¹³CO, five of the permitted A-X bands ((4,0) through (8,0)) and the d12 intersystem band; and for C¹⁸O, the two permitted A-X (4,0) and (5,0) bands. The stronger ¹²CO A-X bands reveal absorption from rotational levels up to $J=6$ (Fig. 13), with the relative populations of all detected levels reasonably described by an excitation temperature $T_{\text{ex}} = 11.7 \text{ K}$ (Fig. 14). Rotational levels up to $J=3$ are detected for ¹³CO, with a corresponding common $T_{\text{ex}} = 7.7 \text{ K}$. Such high excitation temperatures are unusual, as most sight lines with comparable $N(\text{H}_{\text{tot}})$ and A_V in which CO has been detected have $T_{\text{ex}}(^{12}\text{CO}) \sim T_{\text{ex}}(^{13}\text{CO}) \sim 3-5 \text{ K}$; only HD 147888 exhibits a $T_{\text{ex}}(^{12}\text{CO})$ comparable to that seen toward HD 62542 (Sonnentrucker et al. 2007; Burgh et al. 2007; Sheffer et al. 2008). The $N_m(^{12}\text{CO})/N_m(^{13}\text{CO})$ ratio found toward HD 62542, $\sim 62 \pm 8$, is consistent with (but perhaps slightly lower than) the average local $^{12}\text{C}/^{13}\text{C}$ ratio.

CS: For the relatively small sample of sight lines in which the $\lambda 1400$ CS feature has been detected (Destree et al. 2009), only HD 154368 has a higher $W(1400)$ than the $9.3 \text{ m}\text{\AA}$ measured toward HD 62542. As for several other sight lines noted by Destree et al., the available rotational structure for that feature does not yield a good fit to the observed broad CS profile.

OH⁺: While a weak possible absorption feature is present in the UVES spectrum near the expected location of the strongest OH⁺ line at 3583.8 \AA , similar weak features are also seen in the spectra of several lightly reddened stars obtained on the same night; they appear to be residual detector pattern features (Porrás et al. 2014). The 3σ upper limit on the equivalent width ($W < 0.39 \text{ m}\text{\AA}$) obtained after removing that residual feature corresponds to a column density limit $N_{\text{m}}(\text{OH}^+) < 6.5 \times 10^{12} \text{ cm}^{-2}$, using the recently revised f values of Hodges et al. (2018).

UID: The unidentified line at 1300.45 \AA (Destree & Snow 2009) seems to be present particularly in sight lines with fairly strong CN absorption. As that unidentified line is stronger toward HD 62542 than toward X Per by a factor ~ 3 – similar to the differences observed for CN, C₂, and CS in the two sight lines – it may be due to some molecular species that is preferentially present in relatively dense gas.

DIBs: While most of the commonly observed DIBs are quite weak toward HD 62542, a number of the C₂-DIBs have been detected there (Snow et al. 2002b; Ádámkóvics et al. 2005). Equivalent widths for some of the DIBs that could be measured in the UCLES and UVES spectra are listed at the end of Appendix Table 11. In most cases, the equivalent widths agree reasonably well with the values obtained by Ádámkóvics et al. (2005) and Fan et al. (2017). Our values for the $\lambda 5780.6$ and $\lambda 5797.2$ DIBs are somewhat smaller, however, due to different choices for the local continua and extent of the absorption (e.g., Fan et al. 2017), and our somewhat tentative detection of the broader $\lambda 6284.1$ DIB is well above the limit given by Ádámkóvics et al.

4. DISCUSSION

4.1. Physical Conditions in the Main Cloud

In the main cloud that dominates the absorption toward HD 62542, the extensive set of measured atomic and molecular column densities yields multiple diagnostics for the temperature, local hydrogen density, and electron density. Differences in the properties inferred from the various diagnostics may either suggest shortcomings in our understanding of the diagnostics or provide information about nonuniformities in the structure of the cloud. This relatively simple, isolated cloud – which may be representative of the cores of other diffuse molecular clouds (Ádámkóvics et al. 2005) – should provide a useful test for cloud models.

4.1.1. Temperature

Estimates for the local kinetic temperature (T_k) may be obtained from observations of the rotational excitation of molecules (particularly the homonuclear H_2 and C_2), of the fine-structure excitation of O I, and of the widths of absorption (or emission) lines in high-resolution spectra.

H_2 and C_2 rotational excitation: Toward HD 62542, the ratio $N_m(J=1)/N_m(J=0)$ for H_2 yields $T_k = 43 \pm 11$ K (Rachford et al. 2002).⁷ Analysis of the rotational excitation of C_2 , for $J = 0$ –18, yields $T_k \sim 40 \pm 5$ K (Sec. 4.1.2) – consistent with a general tendency for the temperature derived from C_2 to be less than or equal to the value obtained from H_2 (Sonnentrucker et al. 2007). While these are the best estimates currently available for the average T_k in the main component toward HD 62542 (Table 4), some variations may be expected within that main cloud. The somewhat higher excitation temperature derived from the lowest ($J = 0$ –14) rotational levels of C_3 , $T_{ex} \sim 75$ K – which is not uncommon for the relatively small sample of eight lines with data for both C_2 and C_3 – may indicate a radiative contribution to the excitation (Ádámkóvics et al. 2003). The subthermal excitation temperatures obtained for the polar molecules ^{12}CO (11.7 K), ^{13}CO (7.7 K), and CN (~ 2.9 K) reflect a minimum excitation due to the CMBR, with additional excitation (from collisions and/or local CO emission) for the two CO isotopologs.

O I fine-structure excitation: In relatively cool, neutral, primarily atomic clouds, the relative populations in the excited fine-structure states of neutral oxygen are set primarily by a balance between collisional excitation (with H I) and radiative decay – and the ratio $N(O\ I^*)/N(O\ I^{**})$ can yield an estimate for T_k (e.g., Jenkins & Tripp 2011). The observed value for that ratio in the main component toward HD 62542, $\sim 1.9 \pm 0.3$ (for $b = 1.0 \pm 0.1$ km s⁻¹), corresponds to a temperature of about 110 K (from Fig. 15 in Jenkins & Tripp 2011); a slightly higher value is obtained from the

⁷Unfortunately, the S/N ratios in the available *FUSE* spectra of HD 62542 are not high enough to permit reliable measurement of the higher H_2 rotational levels, which otherwise could yield constraints on the density and ambient UV radiation field (Jensen et al. 2010).

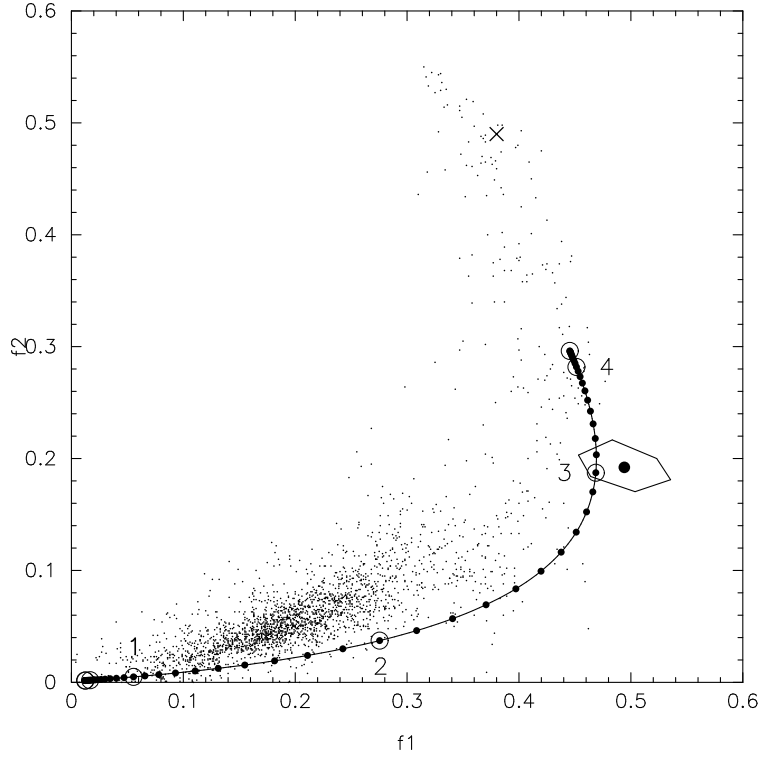


Fig. 15.— Relative C I fine-structure populations [$f_1 = N(\text{C I}^*)/N(\text{C I}_{\text{tot}})$; $f_2 = N(\text{C I}^{**})/N(\text{C I}_{\text{tot}})$] for main component toward HD 62542 (large black dot with $1\text{-}\sigma$ error box), compared to Galactic values from Jenkins & Tripp (2011) (small black dots). The curve gives theoretical predictions for $T = 43$ K (from H_2) and the WJ1 radiation field; the small circles along the curve indicate steps in $\log(n_{\text{H}})$ of 0.1 dex; the larger open circles indicate $\log(n_{\text{H}}) = 4.0, 3.0, 2.0, 1.0$, etc. The slightly stronger radiation field estimated for the main cloud toward HD 62542 would only affect the predictions at the lowest densities. The excitation in the main component toward HD 62542 is consistent with $n_{\text{H}} \sim 1500 \text{ cm}^{-3}$ (adjusted to the scale of Jenkins & Tripp).

more recent analysis of Ritchey et al. (2019; see Sec. 4.1.2).

Line widths: The widths of interstellar absorption features are usually considered to be due to a combination of thermal and internal turbulent broadening, with the line-width parameter $b = (2kT_k/m + 2v_t^2)^{1/2}$, where m is the atomic or molecular weight and v_t is the "turbulent" velocity. While the main-component b values measured for various atomic and molecular species toward HD 62542 are all fairly small – ranging from about 0.5 km s^{-1} (for CO) to about 1.5 km s^{-1} (for Ca II) – the strongest constraint on the temperature comes from the weak lines of vibrationally excited H_2 (the lightest species for which accurate line widths could be determined). The width derived from fits to the H_2^* line profiles, $b = 1.4 \text{ km s}^{-1}$, corresponds to a maximum temperature of about 230 K; the actual T_k would be smaller if turbulent broadening contributes to the line widths. For the component near 27 km s^{-1} the larger b value for Na I (1.4 km s^{-1} , compared to 0.85 km s^{-1} for the main component) suggests that the gas there is somewhat warmer, but less than about 2700 K (for purely thermal broadening of the Na I lines). While the thermal and turbulent contributions to the line broadening of a particular component may (in principle) be separated by comparing the line widths for species of sufficiently different mass, such comparisons are less straightforward if the various species are not entirely coextensive.

4.1.2. Hydrogen Density

Estimates for the local total hydrogen density $n_{\text{H}} = n_{\text{H}^0} + 2n_{\text{H}_2}$ may be obtained from observations of the fine-structure excitation of C I, of the rotational excitation of C_2 and CO, and (via simple chemical models) of the abundances of CH, C_2 , CN, and CO. For clouds with a significant molecular fraction, the densities obtained from C I fine-structure excitation are often significantly smaller than those estimated from molecular diagnostics such as CN or C_2 . Such a difference could arise if C I traces primarily more diffuse atomic gas, but cloud models (e.g., Warin et al. 1996; Le Petit et al. 2006; Visser et al. 2009) suggest that the C I abundance rises with the CO abundance, at least to $A_V \sim 0.8$. In principle, observations of C I, CO, CN, and C_2 in the main component toward HD 62542 – with minimal contributions from diffuse atomic gas – could indicate whether the differences seen in other sight lines are due to sampling mixtures of diffuse and denser gas or to inadequate understanding of the various density diagnostics.

C I fine-structure excitation: In predominantly neutral interstellar clouds, the relative populations in the two upper fine-structure levels in the ground electronic state of C I (denoted C I* and C I**) reflect a balance between collisional excitation, collisional de-excitation, and radiative decays (Jenkins & Shaya 1979; Jenkins & Tripp 2001, 2011). Analyses of the excitation of those C I levels can yield estimates for the local thermal pressures $p/k = n_{\text{H}}T_k$ – and thus n_{H} , if T_k is known. The solid curve in Figure 15 shows the predicted relationship between $f_2 = N(\text{C I}^{**})/N(\text{C I}_{\text{tot}})$ (the fraction of neutral carbon in the second excited state) and $f_1 = N(\text{C I}^*)/N(\text{C I}_{\text{tot}})$ (the fraction in the first excited state), for $T_k = 43 \text{ K}$, the average interstellar UV radiation field, and $\log(n_{\text{H}})$ increasing from -2 (near the origin) to $+5$ (Jenkins & Tripp 2011; Welty et al. 2016).

Corresponding curves for other temperatures follow similar trajectories in the f_1 – f_2 plane; stronger ambient UV radiation fields would move the "origins" of the curves (at the lowest densities) to higher f_1 (and slightly higher f_2), but have little effect at higher densities (see, e.g., Jenkins & Shaya 1979). The small filled circles along the curve indicate steps in $\log(n_{\text{H}})$ of 0.1 dex; the larger open circles mark integer values of $\log(n_{\text{H}})$. The many small black dots show the values found for small velocity intervals along 89 Galactic sight lines in the C I survey of Jenkins & Tripp (2011, hereafter JT11). Their location – often slightly above and/or to the left of the theoretical curves for "reasonable" temperatures for cool, neutral gas – suggests that some high-pressure gas may generally be associated with the more abundant gas at relatively low pressures along many sight lines (Jenkins & Shaya 1979; Jenkins & Tripp 2001, 2011).

The larger black dot at $(f_1, f_2) = (0.49, 0.19)$ in Figure 15 indicates the relative populations found for the main component toward HD 62542 (Table 2); the hexagonal box enclosing that dot gives the 1σ uncertainties (due to the uncertainties in the column densities of the three levels). Within the uncertainties, the C I excitation in that main component apparently can be characterized by a single density (and thermal pressure): $n_{\text{H}} \sim 1500 \text{ cm}^{-3}$ (adjusted to the scale of Jenkins & Tripp 2011; see Welty et al. 2016). The corresponding pressure, $\log(p/k) = \log(n_{\text{H}}T) \sim 4.8$ ($\text{cm}^{-3} \text{ K}$), is more than an order of magnitude higher than the value $\log(p/k)_{\text{low}} = 3.60$ ($\text{cm}^{-3} \text{ K}$) associated with the "center of mass" of the distribution of Galactic points in the Jenkins & Tripp (2011) survey, which is at $(f_1, f_2) \sim (0.21, 0.07)$. The relative excited state populations are lower for the component at 27 km s^{-1} , with $(f_1, f_2) = (0.16, 0.12)$. While that lies above most of the Galactic points in Figure 15 – suggestive of a mixture of gas at high and low pressures – the projection onto the curve predicted for a representative $T = 80 \text{ K}$ (for Galactic diffuse, primarily atomic clouds) would correspond to a density of about 20 cm^{-3} for the majority of the gas at that velocity (and still lower values for higher temperatures). The densities and thermal pressures derived from C I fine-structure excitation should be the most accurate values for this sight line – as they are fairly insensitive to the (relatively poorly constrained) ambient radiation field.

O I fine-structure excitation: Ritchey et al. (2019) have developed a method for estimating both the temperature and the density from the observed fine-structure excitation of O I, by comparing the ratio of the excited state populations $N(\text{O I}^*)/N(\text{O I}^{**})$ with the ratio of excited to total O I [$N(\text{O I}^*)+N(\text{O I}^{**})$]/[$N(\text{O I})+N(\text{O I}^*)+N(\text{O I}^{**})$]. For the main cloud toward HD 62542, comparison of the two ratios yields $T \sim 140 \text{ K}$ (dependent primarily on the excited state ratio) and $n_{\text{H}} \sim 350 \text{ cm}^{-3}$ (dependent primarily on the ratio of excited to total O I), with relatively little sensitivity to $f(\text{H}_2)$.

C₂ rotational excitation: As both radiative and collisional processes contribute to the rotational excitation of C₂ in interstellar clouds, comparison of the observed $N(J)$ with models for the excitation can yield estimates for both the cloud kinetic temperature T_{k} and the local density of collision partners $n_{\text{c}} = n_{\text{H}^0} + n_{\text{H}_2}$ (van Dishoeck & Black 1982; van Dishoeck & de Zeeuw 1984; Sonnentrucker et al. 2007). In general, the lowest rotational levels provide the strongest constraints on T_{k} , while the higher rotational levels provide the strongest constraints on the density. Figure 16

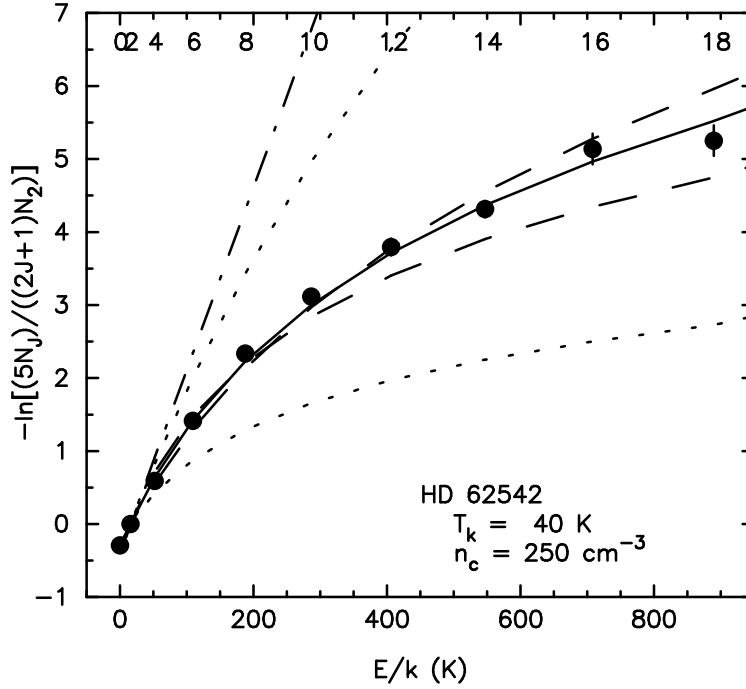


Fig. 16.— Rotational excitation of C_2 toward HD 62542, based on the $N_m(J)$ derived from the D-X (0-0) band, compared to values predicted by the analysis of van Dishoeck & Black (1982) (adjusted for our adopted C_2 f values; see Sonnentrucker et al. 2007). The solid curve represents the best-fit theoretical model (to the nearest 5 K in the kinetic temperature T_k and 50 cm^{-3} in the density of collision partners (H and H_2) n_c). The straight dotted-dashed line shows the thermal equilibrium distribution for the best-fit T_k ; the two dotted curves show the distributions for that T_k and $n_c = 1000$ and 100 cm^{-3} . The two dashed curves show the distributions for $(T_k - 10, n_c - 50)$ and $(T_k + 10, n_c + 50)$. If $f(H_2) = 0.81$ (and assuming an average near-IR radiation field), then the local density of hydrogen nuclei would be $n_H \sim 430 \text{ cm}^{-3}$.

compares the observed relative C₂ rotational populations, for $J = 0$ –18, with several theoretical curves. If the ambient near-IR radiation field (which is primarily responsible for the initial excitation of the C₂) incident on the main cloud toward HD 62542 is of "average" strength, then the observed $N_m(J)$ are most consistent with $T_k \sim 40 \pm 5$ K and $n_c \sim 250_{-25}^{+50}$ cm⁻³ (solid curve); n_c would be proportionally higher (lower) if the ambient near-IR field is stronger (weaker) than average. The straight dotted-dashed line shows the thermal equilibrium distribution for the best-fit T_k ; the two dotted curves show the distributions for that T_k and $n_c = 1000$ and 100 cm⁻³ (steeper and shallower, respectively); the two dashed curves show the distributions for $(T_k - 10, n_c - 50)$ and $(T_k + 10, n_c + 50)$.⁸ The inferred $T_k = 40$ K and $n_c = 250$ cm⁻³ are fairly typical of the values found for Galactic sight lines where C₂ is detected (e.g., Sonnentrucker et al. 2007). As the hydrogen in the main cloud is mostly molecular [$f(\text{H}_2) = 0.81$], the local density of hydrogen nuclei n_{H} is then ~ 430 cm⁻³ (a factor of 3–4 lower than the density inferred from C I fine-structure excitation).

CO rotational excitation: In diffuse molecular gas in the Galactic ISM, the excitation temperatures for both ¹²CO and ¹³CO are typically 3–5 K (Sonnentrucker et al. 2007; Sheffer et al. 2008), with the minimum T_{ex} set by the CMBR. Goldsmith (2013) derived estimates for the density in sight lines where the CO excitation (obtained from UV absorption) exceeds that minimum. For sight lines in common with the C I survey of JT11, those density estimates can be compared with the values obtained from C I fine-structure excitation (assuming T_k from H₂), for the velocity intervals over which CO absorption is seen (and where the available C I lines are not severely saturated). The velocity information comes from component fits tabulated by Sheffer et al. (2008), from our own fits to available high-resolution optical spectra of CH and/or CN, or from simple comparisons of the CO and C I profiles in STIS echelle spectra. In general, the density estimates derived from CO and from C I are consistent within a factor of ~ 2 , though the values from CO appear to be systematically lower where the UV radiation field estimated from the C I excitation is stronger than average (e.g., toward HD 37903) and higher where the UV field is weaker (e.g., toward HD 27778, HD 206267). In the main cloud toward HD 62542, however, $T_{\text{ex}}(^{12}\text{CO}) = 11.7$ K and $T_{\text{ex}}(^{13}\text{CO}) = 7.7$ K. Those higher than typical CO excitation temperatures – beyond the range shown by Goldsmith (2013) – would seem to imply a very high density in the main cloud, but the constancy of T_{ex} with J , for both ¹²CO and ¹³CO, is inconsistent with the predictions of those models (see also Liszt 2007).

Alternatively, the CO in the main cloud may be excited radiatively (Wannier et al. 1997), as there is fairly strong CO emission in the vicinity of the cloud, with $T_{\text{A}}(^{12}\text{CO}) \sim 8$ K along the sight

⁸The relationships between the C₂ rotational populations and T_k and n_c are based on the models of van Dishoeck & Black (1982), as calculated by B. J. McCall (<http://dib.uiuc.edu/c2/>), on a grid with $\Delta T = 5$ K and $\Delta n_c = 60$ cm⁻³ – but with the densities reduced by a factor of 1.2 to reflect the smaller C₂ f values adopted in this study (see van Dishoeck & de Zeeuw 1984 and Sonnentrucker et al. 2007) and using all of the observed rotational populations. More recent determinations of the C₂ collisional rates (Najar et al. 2008, 2009) suggest that the densities obtained assuming a constant collisional de-excitation cross-section $\sigma = 2 \times 10^{-16}$ cm² may be slightly overestimated (e.g., Casu & Cecchi-Pestellini 2012; Welty et al. 2013).

line to HD 62542 and ~ 15 K in several nearby peaks in the emission (Gredel et al. 1994). Figure 2 in Wannier et al. (1997), indicates, for example, that $T_{\text{ex}} \sim 11.5$ K could be obtained for $n(\text{H}_2) = 750 \text{ cm}^{-3}$, $T_{\text{k}} = 30$ K, a CO(1-0) brightness temperature of 10 K, and a filling factor of order 0.2 – which seems not unreasonable, given the distribution of CO emission near HD 62542 (Gredel et al. 1994). The uniform excitation temperatures found for both CO isotopologs and the somewhat lower value found for ^{13}CO would also be consistent with radiative excitation of the CO (Wannier et al. 1997; Sonnentrucker et al. 2007).

Chemical models: Simple chemical models, assuming steady-state gas-phase chemistry and incorporating only the most significant reactions, can yield estimates for the local hydrogen density from the observed abundances of CH, C₂, and CN (e.g., Federman et al. 1994, 1997; see also Welty et al. 2006). For example, a simplified equation for CH, balancing creation (initiated by C⁺ + H₂) against destruction (via photodissociation and reactions with C⁺ and O⁰), can be written as

$$N(\text{CH}) \sim \frac{0.67 k(\text{C}^+, \text{H}_2) x(\text{C}^+) N(\text{H}_2) n_{\text{H}}}{I_{\text{UV}} G_0(\text{CH}) + [k(\text{C}^+, \text{CH}) x(\text{C}^+) + k(\text{O}^0, \text{CH}) x(\text{O}^0)] n_{\text{H}}}. \quad (1)$$

The k values are reaction rate coefficients (with updates given by Pan et al. 2001), the x values are fractional abundances (1.6×10^{-4} for C⁺, 3.0×10^{-4} for O), and $I_{\text{UV}}G_0(\text{CH})$ is the photodissociation rate for CH (approximately adjusted for dust extinction using $\tau_{\text{UV}} = 3 \times A_{\text{V}}$, given the steep far-UV extinction seen toward HD 62542). For relatively low densities, photodissociation dominates the destruction, but the reactions with C⁺ and O⁰ can be comparable for $n_{\text{H}}/I_{\text{UV}}$ greater than a few hundred per cm³. If $I_{\text{UV}} = 1$, and for $A_{\text{V}} = 0.9\text{--}1.0$ in the main component toward HD 62542, then the simplified equations for CH, C₂, and CN yield estimated $n_{\text{H}} \sim 750 \pm 100$, 450 ± 60 , and $315 \pm 45 \text{ cm}^{-3}$, respectively, for that component. A stronger UV field would imply proportionally higher densities. The lower density inferred from CN is somewhat surprising – as the chemical reaction networks (e.g., Federman et al. 1994) generally suggest that CN should trace denser gas than CH. More detailed modeling of the cloud (e.g., using the specific UV extinction curve for this sight line and incorporating a more extensive reaction network) may be needed to obtain more concordant density estimates from the various molecular species detected there.

Summary: In the main component toward HD 62542, the density obtained from C I fine-structure excitation ($\sim 1500 \text{ cm}^{-3}$) is greater, by factors of 2–4, than those obtained from C₂ rotational excitation and from the simple chemical models. Because the latter depend (linearly) on the ambient NIR and UV radiation fields (respectively) but the former does not, the apparent differences in inferred density could be reconciled if the radiation field were enhanced by a factor of 2–4, relative to the average interstellar field. As discussed below (Secs. 4.1.3 and 4.1.4), such an enhancement in the radiation field is quite plausible, given the relative proximity of ζ Pup and γ^2 Vel. The lower density (and higher temperature) inferred from O I fine-structure excitation may be due to the O I tracing somewhat warmer, less dense regions of the cloud than the C I and the molecular species – an issue which will be explored more quantitatively in constructing detailed models of the cloud. For a density $n_{\text{H}} \sim 1500 \text{ cm}^{-3}$, the thickness of the main cloud would be $N(\text{H}_{\text{tot}})/n_{\text{H}} \sim 0.34 \text{ pc}$.

A total density of hydrogen nuclei of order 1500 cm^{-3} would be consistent with three other, independent estimates for the density and/or pressure characterizing the main cloud toward HD 62542. Velusamy et al. (2017) used *Herschel* HIFI observations of the $158 \mu\text{m}$ C II] emission toward HD 62542 to infer a pressure $p/k = 3.11 \pm 0.21 \times 10^4 \text{ K cm}^{-3}$ and a density of molecular hydrogen $n(\text{H}_2) = 720 \pm 50 \text{ cm}^{-3}$ (corresponding to $n_{\text{H}} = 1440 \pm 100 \text{ cm}^{-3}$). van Dishoeck et al. (1991) obtained a "preferred" density of 1500 cm^{-3} (with a range of $500\text{--}3000 \text{ cm}^{-3}$) from the ^{12}CO (1-0)/(3-2) ratio. Cardelli & Savage (1988) obtained a very similar estimate for the pressure for the main cloud, of order $3 \times 10^4 \text{ K cm}^{-3}$, based on considerations of pressure balance with the stellar wind from γ^2 Vel (at an assumed star-cloud distance of 50 pc). Both the moderately high density and the minimal atomic envelope associated with the main cloud may thus be due to the effects of the winds (and radiation pressure?) from ζ Pup and γ^2 Vel (Cardelli et al. 1990).

4.1.3. Radiation Field

Indications that the material in the IRAS Vela shell near the main cloud toward HD 62542 has been shaped by the winds from ζ Pup and γ^2 Vel (Cardelli & Savage 1988; Sahu 1992; Churchwell et al. 1996; Pereyra & Magalhaes 2002) and the differences in the densities derived from C I fine-structure excitation, C₂ rotational excitation, and simple chemical models both suggest that those two bright, early-type stars may also significantly affect the radiation field surrounding that cloud. The O5 Iaf star ζ Pup, at a distance of 330 pc, is about 4.5 degrees away from the sight line to HD 62542, and so is at least 26 pc away from the cloud; the WC8+O9 I binary γ^2 Vel, at a distance of 340 pc, is about 7.1 degrees away from the sight line, and so is at least 42 pc away from the cloud. While the distance to the cloud itself is not known, there are hints that it is at least slightly closer than those two stars (Churchwell et al. 1996). UV spectra obtained with *IUE* indicate that the two stars have observed fluxes of order 1.0 and $1.4 \times 10^{-8} \text{ erg cm}^{-2} \text{ s}^{-1} \text{ \AA}^{-1}$ at 2000 \AA , respectively. Neglecting the modest reddening toward the two stars and scaling those observed fluxes to the respective minimum distances to the cloud yields values of order 1.6 and $0.9 \times 10^{-6} \text{ erg cm}^{-2} \text{ s}^{-1} \text{ \AA}^{-1}$ at the cloud – which are quite comparable to the flux characterizing the Draine (1978, hereafter D78) field at 2000 \AA (but higher at shorter wavelengths). Roughly equal contributions from the average (D78) field and from each of the two stars would thus appear to be reasonably consistent with the factor of 2–4 enhancement over the average field suggested by the various estimates for the local hydrogen density. While an enhanced UV field would tend to depress the abundances of various trace neutral and molecular species, the observed abundances of those species suggest that the relatively high density and the unusually steep far-UV extinction characterizing the cloud have (to some degree) counteracted those effects of the radiation field.

Table 7. Photoionization and Recombination Coefficients

Element	A_{\odot}	χ_{ion} (eV)	Γ_0^{a} ($\times 10^{-11}$)	$\Gamma_{\text{K50}}/\Gamma_0^{\text{b}}$	$\Gamma/\Gamma_0^{\text{c}}$	$\alpha_{\text{r}}^{\text{d}}$ ($\times 10^{-12}$)	η^{d}	$\alpha_{\text{d}}^{\text{e}}$ ($\times 10^{-12}$)	$\alpha_{\text{t}}^{\text{e}}$ ($\times 10^{-12}$)	$\alpha_{\text{g}}^{\text{f}}$ ($\times 10^{-14}$)	S^{f}
C	8.46	11.26	35.0	4.9	0.25	8.29	0.621	10.30	18.87	3.63	0.2
Na	6.37	5.14	1.4	2.2	0.41	5.82	0.682	0.00	6.23	1.91	0.2
Mg	7.62	7.65	6.6	1.6	0.49	5.87	0.681	0.00	7.59	2.13	0.95
Si	7.61	8.15	450.0	1.9	0.44	8.42	0.617	81.60	89.73	1.94	0.95
P	5.54	10.49	190.0	4.1	0.31	6.98	0.645	53.30	64.17	[2.16]	0.2
S	7.26	10.36	110.0	4.1	0.27	10.50	0.593	0.00	10.50	2.12	0.2
K	5.18	4.34	3.9	1.9	0.45	5.54	0.683	0.00	4.31	1.43	0.2
Ca	6.41	6.11	35.0	1.3	0.46	5.58	0.683	0.00	5.58	1.50	0.95
Ti	5.00	6.82	24.0	[2.0]	0.39	5.50	0.684			[1.58]	0.95
Cr	5.72	6.77	160.0	[2.0]	0.47	6.00	[0.685]	0.00	6.00	[1.32]	0.95
Mn	5.58	7.43	3.3	[2.0]	0.51	5.45	0.686	0.00	5.45	1.48	0.95
Fe	7.54	7.90	47.0	2.2	0.47	5.45	0.686			1.42	0.95
Ni	6.29	7.63	9.8	[2.0]	0.50	5.56	0.681			[1.37]	0.95
Zn	4.70	9.39	41.0	4.0	0.28	4.52	0.700	0.00	4.52	[1.48]	0.2

^aPhotoionization rate Γ_0 at cloud edge, for Draine (1978) radiation field (D78; Heays et al. 2017).

^bMultiplier for the photoionization rate for the radiation field from a Kurucz (1993) model with $T = 50,000$ K (K50), scaled to have equal flux to the D78 field at 2000 \AA .

^cAttenuation factor (Γ/Γ_0) due to extinction within the cloud, obtained from the coefficients tabulated by van Dishoeck (1988), for $A_V = 0.5$ (cloud center).

^dRadiative recombination rate coefficient is given by $\alpha_{\text{r}}(T/100)^{-\eta}$ [Péquignot & Aldrovandi 1986; S. Nahar 2008, private communication (Cr); Mazzitelli & Mattioli 2002 (Zn)].

^eDielectronic and total recombination rate coefficients, at $T = 100$ K [Badnell et al. 2003; Badnell 2006 (C, Na, Mg, K); Abdel-Naby et al. 2012 (Si); Kaur et al. 2018 (P)]; Péquignot & Aldrovandi 1986 (other elements).

^fGrain-assisted recombination rate coefficient (α_{g}) is calculated from the fitting coefficients tabulated by Weingartner & Draine (2001), for a grain charging parameter $\psi \sim 50 \text{ K}^{1/2} \text{ cm}^3$; values in square braces are estimated (see text). The sticking parameter S reflects the depletion behavior (0 = no depletion, 1 = complete depletion).

Table 8. Electron Densities (Main Component)

Element	Γ ($\times 10^{-11}$) ^a		α_r ^b	α_d ^b	α_t ^b	α_g ^c	S ^c	$N(X\text{ I})$	$N(X\text{ II})$	X I/X II	$n_e(\text{rad})$ ^d	$n_e(\text{tot})$ ^d	$n_e(\text{ga})$ ^d
	D78	D+2K50	($\times 10^{-12}$)	($\times 10^{-12}$)	($\times 10^{-12}$)	($\times 10^{-14}$)		(cm^{-2})	(cm^{-2})		D78	D+2K	(cm^{-3})
C	8.8	94.5	14.36	23.2	37.6	3.63	0.2	15.41	[17.40]	[-1.99]	[0.06]	[0.26]	...
Na	0.6	3.1	10.81	0.0	10.8	1.91	0.2	14.04
Mg	3.2	13.6	12.88	0.0	12.9	2.13	0.95	13.81	14.41	-0.60	0.62	2.65	2.06
Si	198.0	950.4	13.78	102.2	116.0	1.94	0.95	11.60	14.48	-2.88	0.19	0.11	0.10
P	58.9	541.9	16.13	131.3	147.5	[2.16]	0.2	12.01	13.86	-1.85	0.52	0.52	[0.34]
S	29.7	273.2	16.82	0.0	16.8	2.12	0.2	14.64	[16.10]	[-1.46]	[0.61]	[5.63]	[4.11]
K	1.8	8.4	7.92	0.0	7.9	1.43	0.2	12.08
Ca	16.1	58.0	9.93	0.0	9.9	1.50	0.95	9.10	11.41	-2.31	0.08	0.29	0.16
Ti	9.4	46.8	9.80	...	[25.0]	[1.58]	0.95	<10.03	10.69	< -0.66	<2.1	<4.1	...
Cr	75.2	376.0	10.70	0.0	10.7	[1.32]	0.95	<9.68
Mn	1.7	8.4	9.72	0.0	9.7	1.48	0.95	<10.67	<12.72
Fe	22.1	119.3	9.72	...	[25.0]	1.42	0.95	11.28	13.81	-2.53	0.07	[0.14]	[0.10]
Ni	4.9	24.5	9.88	...	[25.0]	[1.37]	0.95	<10.68	12.59	< -1.91	<0.06	<0.12	...
Zn	11.5	103.3	8.16	0.0	8.2	[1.48]	0.2	12.13	12.87	-0.74	2.56	23.0	[20.8]

^aPhotoionization rate Γ at cloud center ($A_V = 0.5$), for the Draine (1978) radiation field and for that D78 field plus 2 times the scaled K50 field – both attenuated by the factor Γ/Γ_0 from Table 7.

^bRadiative, dielectronic, and total recombination rate coefficients, for $T = 43$ K. C, Na, Mg, Si, P, and K are from Badnell (2006), Abdel-Naby et al. (2012), and Kaur et al. (2018); Cr is from S. Nahar 2008, private communication; Zn is from Mazzitelli & Mattioli (2002); all others are from Péquignot & Aldrovandi (1986).

^cGrain-assisted recombination rate coefficient (α_g) and sticking coefficient (S) (Weingartner & Draine 2001).

^dElectron densities calculated assuming only radiative recombination (for the D78 field) and radiative plus dielectronic recombination (for the D78 field + 2 \times the K50 field) or including grain-assisted recombination (for the D78 + 2 \times the K50 field).

4.1.4. Electron Density

It has often been assumed that the free electrons present in diffuse clouds are due primarily to the photoionization of carbon, so that the fractional electron abundance n_e/n_H can be approximated by the gas-phase carbon abundance (typically $\sim 1.4\text{--}1.6 \times 10^{-4}$; e.g., Sofia et al. 2004). There are indications, however, that photoionization and radiative recombination are not the only processes significantly affecting the ionization balance in such clouds, and that the electron fractions can often be larger than the value that would be expected from carbon alone (e.g., Welty et al. 1999, 2003; Welty & Hobbs 2001; Weingartner & Draine 2001; Liszt 2003). In particular, grain-assisted recombination – where an atomic ion is neutralized via charge exchange with a neutral or negatively charged small dust grain (or large molecule) – can be more significant than radiative recombination for some elements (Weingartner & Draine 2001), and cosmic-ray ionization of H can be a significant source of electrons (e.g., Liszt 2003; Indriolo et al. 2007, 2009). For the main cloud toward HD 62542, a likely lower limit for the electron density may be obtained from the inferred values of $n_H \sim 1500 \text{ cm}^{-3}$ and $N_m(\text{C}^+)/N_m(\text{H}_{\text{tot}}) \sim 1.6 \times 10^{-4}$ – yielding $n_e \gtrsim 0.24 \text{ cm}^{-3}$ – but the available absorption-line data provide several other avenues for estimating the electron density.

CN excitation: The rotational excitation of CN is typically dominated by the CMBR (e.g., Roth & Meyer 1995; Ritchey et al. 2011), but collisions (primarily with electrons) can increase the excitation at higher densities (Thaddeus 1972; Black & van Dishoeck 1991). The analysis of Ritchey et al. suggests that the excess in excitation temperature is proportional to the local electron density n_e times the rate coefficient for electron excitation of CN (e.g., Allison & Dalgarno 1971). Using the rate of electron excitation of CN at 40 K (Allison & Dalgarno 1971), the observed excess excitation ($T_{01} - T_{\text{CMBR}} = 0.16 \pm 0.15 \text{ K}$) implies $n_e \sim 0.43 \pm 0.40 \text{ cm}^{-3}$ – somewhat lower than the $1\text{--}2 \text{ cm}^{-3}$ estimated by Cardelli et al. (1990) from their adopted $T_{01} = 3.7 \pm 0.4 \text{ K}$. Given the large relative uncertainty, we adopt the 3σ upper limit $n_e < 1.2 \text{ cm}^{-3}$ from the CN excitation.

Fine-structure excitation of ionized species: Observations of the excited fine-structure states of ions such as C II and Si II can yield estimates for n_e , as collisions with electrons are primarily responsible for the excitation; IR radiation and UV fluorescence may also contribute (Bahcall & Wolf 1968; York & Kinahan 1978; Fitzpatrick & Spitzer 1997; see also Vreeswijk et al. 2007 and Prochaska et al. 2006 for applications to GRB absorbers). Unfortunately, it is difficult to obtain accurate values for $N_m(\text{C II})$, $N_m(\text{C II}^*)$, and $N_m(\text{Si II}^*)$ toward HD 62542, as the interstellar lines are blended with strong, relatively narrow stellar lines, and no excited fine-structure lines are detected for Fe^+ or Ni^+ .

Ionization equilibrium: Ratios of the column densities of trace neutral species and the corresponding dominant first ions $N(\text{X I})/N(\text{X II})$ are often used to estimate n_e , under the usual assumption of photoionization equilibrium. Detailed studies of several individual sight lines, however, have found that the n_e inferred in that way from different elements can be quite different (e.g., Fitzpatrick & Spitzer 1997; Welty et al. 1999); moreover, the pattern of those differences can vary from one sight line to another (Welty et al. 2003). The incorporation of grain-assisted recombina-

tion into the ionization balance may reduce some (but not all) of those differences (Weingartner & Draine 2001; Liszt 2003; Welty et al. 2003). As many trace neutral species are detected in the main cloud toward HD 62542, a number of different X I/X II ratios can be used to further investigate those element-to-element differences in estimated n_e in what appears to be a single cloud. Table 7 compiles the various parameters used to compute the photoionization rates and recombination rate coefficients for 14 elements detected in the main cloud toward HD 62542. Table 8 lists the adopted photoionization rates (at cloud center) and recombination rate coefficients (for $T = 43$ K), the measured or estimated column densities for the neutral and singly ionized forms of those elements (Table 3), and several estimates for the electron density in the main cloud.

The photoionization rate depends on the shape and amplitude of the radiation field incident on the cloud and on the attenuation of that field within the cloud. In order to gauge the effects of different radiation fields on the relative photoionization rates for different elements (and thus on the corresponding inferred relative n_e), we calculated the rates at the outer edge of the cloud (Γ_0) for the D78 and Mathis et al. (1983, hereafter MMP) fields, and also for the fields produced by Kurucz (1993) model atmospheres with $T_{\text{eff}} = 12,000, 26,000, \text{ and } 50,000$ K (K12, K26, and K50; corresponding roughly to late-B, early-B, and mid-O stars, respectively), matched to the D78 flux at 2000 \AA . For most of the elements considered, we used the photoionization cross sections given by Verner et al. (1996) and by Bautista et al. (1998), which are based on fits to experimental or theoretical values, averaged over resonances. In most cases, the Γ_0 values calculated for the D78, MMP, and K26 fields are fairly similar [e.g., the $\Gamma_0(\text{MMP})/\Gamma_0(\text{D78})$ ratio is typically ~ 0.7], and the new values for Γ_0 generally agree with those calculated for the WJ1 field (e.g., Péquignot & Aldrovandi 1986) to within factors of 2–3. The higher FUV flux produced by the hotter K50 model – which would be more similar to the spectra of ζ Pup and γ^2 Vel – yields somewhat higher Γ_0 for neutrals with high χ_{ion} (C, P, S, Zn) (column 5 of Table 7). The table lists the values for Γ_0 for the D78 field, as tabulated by Heays et al. (2017), along with a multiplicative factor ($\Gamma_{\text{K50}}/\Gamma_0$) for the rates that would be due to the K50 field, scaled to have equal flux to the D78 field at 2000 \AA . The reductions in the photoionization rates at cloud center (Γ/Γ_0 , for $A_V \sim 0.5$), obtained from the coefficients tabulated by van Dishoeck (1988), range from 0.25 to 0.31 for elements with ionization potentials $\chi_{\text{ion}} \sim 9\text{--}13$ eV (i.e., those most sensitive to the steep far-UV extinction) and from 0.39 to 0.51 for elements with lower χ_{ion} . We note that the increased photoionization in the harder K50 field for those elements with high χ_{ion} would thus be offset somewhat by the effects of selective extinction within the cloud.

Several different recombination processes can contribute to the total recombination rates for the different elements. For temperatures below about 1000 K, the radiative recombination rate coefficients can be given by $\alpha_r(T/100)^{-\eta}$, with η typically about 0.7 [Péquignot & Aldrovandi 1986 (most elements); S. Nahar 2008, private communication (Cr); Mazzitelli & Mattioli 2002 (Zn)]. While the contributions of dielectronic recombination have long been recognized at temperatures above 1000 K (e.g., Burgess 1964; Shull & van Steenberg 1982; Nussbaumer & Storey 1983; Arnaud & Rothenflug 1985), more recent calculations have indicated a significant contribution at much lower

temperatures for ions with fine-structure splitting in the ground state (Badnell et al. 2003; Bryans et al. 2009). Of the elements listed in Tables 7 and 8, dielectronic recombination would thus be expected to be significant in cold interstellar clouds for C, Si, P, Ti, Fe, and Ni, but not for Na, Mg, S, K, Ca, Cr, Mn, or Zn. Those expectations are borne out for C, Na, Mg, Si, P, and K by the calculations of Badnell et al. (2003), Badnell (2006), Abdel-Naby et al. (2012), and Kaur et al. (2018), which include the contributions from the excited fine-structure levels.⁹ At $T = 100$ K, for example, the dielectronic rate is roughly 8–10 times higher than the radiative rate for Si and P, about equal to the radiative rate for C, and negligible for Na, Mg, and K. As no such calculations have been made as yet (to our knowledge) for S, Ca, Ti, Cr, Mn, Fe, Ni, or Zn, we have assumed that the dielectronic rate is slightly higher than the radiative rate for Ti, Fe, and Ni, but can be neglected for S, Ca, Cr, Mn, and Zn. As the radiative recombination rates recently calculated by Badnell and collaborators generally agree well with those obtained from the parameters listed by Péquignot & Aldrovandi (1986), we have adopted the latter values for elements not considered by Badnell et al. The grain-assisted recombination rate coefficients (α_g) are calculated from the fitting coefficients tabulated by Weingartner & Draine (2001), for a charging parameter $\psi = G T^{1/2} / n_e \sim 50 \text{ K}^{1/2} \text{ cm}^3$ (assuming a radiation field parameter $G \sim 4$, $T = 43$ K, and $n_e \sim 0.5 \text{ cm}^{-3}$). For P, Ti, Cr, Ni, and Zn (which were not considered by Weingartner & Draine), we have used the fitting coefficients for the element nearest in ionization potential, scaling C_0 (only) by the square root of the ratio of atomic weights (B. Draine 2017, private communication). The assumed sticking factors (S), used in the subsequent calculation of the electron densities, reflect the depletion behavior of each element (0 = no depletion, 1 = complete depletion).

Where information for both X I and X II is available, the $n_e(\text{rad})$ – obtained by assuming only radiative recombination (at $T = 43$ K) and using the attenuated Γ at the center of the cloud – range from less than 0.2 cm^{-3} (for C, Si, Ca, Fe, and Ni) to 2.6 cm^{-3} (for Zn); intermediate values are obtained for Mg, P, and S. If the radiation field is stronger than average (as suggested by the discussions above), then the $n_e(\text{rad})$ would all be correspondingly higher (with some relative differences, if the shape of the field differs from the standard D78 field). For both the D78 and MMP fields, the individual values for $n_e(\text{rad})$ range over a factor of more than 40, but there are no obvious trends with either χ_{ion} or depletion. The n_e estimates in the next-to-last column of Table 8 correspond to an ambient radiation field characterized by roughly equal contributions at 2000 \AA from the D78 field, from ζ Pup, and from γ^2 Vel (both approximated by the K50 field; see Sec. 4.1.3 above), but also include the effects of low-temperature dielectronic recombination. For that stronger composite field, the increases in n_e are offset to varying degrees by the dielectronic recombination, and the range in relative n_e is larger than for the D78 field (and radiative recombination) alone. The n_e estimates in the last column of the table, which include the effects of grain-assisted recombination according to eqn. 16 in Weingartner & Draine (2001) for $\psi \sim 50 \text{ K}^{1/2} \text{ cm}^3$, are somewhat lower than the values in the previous column, with larger differences for the less-depleted elements. Iterative

⁹Parameters for calculating the radiative and dielectronic rates are tabulated at <http://amdpp.phys.strath.ac.uk/tamoc/DATA/>

solutions for n_e for the individual elements yield a wide range in ψ and n_e , and do not qualitatively change the relative n_e . The pattern of relative n_e toward HD 62542 seen in the last three columns of Table 8 does not resemble those seen for the few other sight lines where such comparisons have been made (Welty et al. 2003); in particular, the n_e obtained from the Ca I/Ca II ratio is not higher than the values determined from the corresponding ratios for other elements. The values from Mg, S, and (especially) Zn exceed the upper limit estimated from CN excitation, while the values from Si, Fe, and Ni are below the lower limit estimated from the carbon abundance.

Estimates for the cosmic-ray ionization rate (ζ_p) in relatively low-density, predominantly atomic gas may be obtained from observations of OH^+ (e.g., Hollenbach et al. 2012; Porras et al. 2014; Bacalla et al. 2019). The simple chemical model described by Porras et al., for example, which balances the most significant production and destruction processes, leads to $\zeta_p \sim 1.3 \times 10^{-10} n_H N_m(\text{OH}^+)/N_m(\text{H})$. If our observed limit for the OH^+ abundance toward HD 62542 applies to the outer, primarily atomic layer of the main cloud, with $N_m(\text{H}) \sim 3 \times 10^{20} \text{ cm}^{-2}$ (Table 3) and $n_H \sim 20 \text{ cm}^{-3}$ (as estimated for the diffuse component at 27 km s^{-1} ; Sec. 4.1.2), and assuming $T = 80 \text{ K}$ there (as in Porras et al.), then that relationship between ζ_p and the OH^+ abundance yields $\zeta_p < 5.6 \times 10^{-17} \text{ s}^{-1}$. Inclusion of the effects of polycyclic aromatic hydrocarbons (PAHs) on the ionization (Hollenbach et al. 2012; Bacalla et al. 2019) then would imply $\zeta_p < 1.9\text{--}2.8 \times 10^{-16} \text{ s}^{-1}$. These limits fall within the range of ionization rates (from several references) tabulated by Bacalla et al. (2019) (all adjusted for the f value for the OH^+ $\lambda 3583.8$ line from Hodges et al. (2018)).

4.1.5. Summary of Physical Conditions

Snow & McCall (2006) proposed characterizing cloud regimes (diffuse, diffuse molecular, translucent, dense) on the basis of local chemical properties — principally $f(\text{H}_2)$ and the relative abundances of C II, C I, and CO — reflecting the importance of those species for chemistry and cooling. In that picture, the transition from H to H_2 takes place in the diffuse molecular gas, and the transition from C II to C I and CO takes place in the translucent regime (where $f(\text{H}_2)$ is ~ 1). While cloud models appear able to reproduce the observed dependence of $N(\text{CO})$ on $N(\text{H}_2)$ (Sonnentrucker et al. 2007; Sheffer et al. 2008; Visser et al. 2009), those same models are less successful in describing the relative behavior of C I and CO, which can be very sensitive to both density and radiation field (Burgh et al. 2010). In the main cloud which dominates the absorption toward HD 62542, most of the carbon is singly ionized [with $N_m(\text{C II}) > N_m(\text{CO}) > N_m(\text{C I})$]¹⁰, the depletions of the more refractory elements are severe (remarkably so for Mg and Si; see below), the molecular abundances are generally consistent with expectations for moderately dense gas (e.g., strong C_2 , C_3 , CO, and CN, but weak CH^+ and OH^+), and the extensive set of measured atomic and molecular column densities has yielded multiple diagnostics for the temperature, local hydro-

gen density, and electron density. Those diagnostics indicate that $f(\text{H}_2) = 0.8\text{--}1.0$, $T_k = 40\text{--}43$ K, and $n_{\text{H}} \sim 1500 \text{ cm}^{-3}$ – i.e., the cloud is cool, relatively dense, and primarily molecular – placing it within the translucent regime. The ambient radiation field appears to be two to four times stronger than the average local Galactic field, with contributions from ζ Pup and γ^2 Vel each comparable to that of the average field. The electron density is rather uncertain, but may be of order 0.5 cm^{-3} .

Burgh et al. (2010) have suggested that translucent material can be characterized by the ratios $N(\text{CO})/N(\text{H}_2) \gtrsim 10^{-6}$ and $N(\text{CO})/N(\text{C I}) \gtrsim 1$. Both ratios increase with $f(\text{H}_2)$, and they exhibit a fairly tight, nearly linear relationship with each other over nearly three orders of magnitude. For the main cloud toward HD 62542, the derived $\log[N_{\text{m}}(\text{CO})/N_{\text{m}}(\text{H}_2)] = -4.39$ (dex) and $N_{\text{m}}(\text{CO})/N_{\text{m}}(\text{C I}) = 10.2$ are among the highest known values for both ratios – again suggesting that the cloud may be classified as translucent. Dirks & Meyer (2019) obtained $N(\text{CO})$ and $N(\text{C I})$ from fits to UV absorption profiles and estimated $N(\text{H}_2)$ for 25 sight lines (including HD 62542) near *Planck* Galactic Cold Clump sources (PGCC; Planck Collaboration 2016), then used the two ratios suggested by Burgh et al. (2010) in an attempt to characterize the properties and spatial structure of those sources. They found systematic declines in $N(\text{CO})$, $N(\text{CO})/N(\text{C I})$, and $N(\text{CO})/N(\text{H}_2)$ with the (relative) separation between the source and the stellar sight line for the eight sight lines with $N(\text{CO}) > 10^{15} \text{ cm}^{-2}$ in the sample, but saw no such trend for the 17 sight lines with smaller $N(\text{CO})$. Examination of the thermal pressures available for three of the high $N(\text{CO})$ and nine of the lower $N(\text{CO})$ sight lines (Jenkins & Tripp 2011; this paper) indicates that all but two have $\log(n_{\text{H}}T) \sim 3.3\text{--}3.7 \text{ cm}^{-3} \text{ K}$ at the velocities of the main components seen in CO and C I – consistent with typical values in the Galactic ISM (Jenkins & Tripp 2011) – with no obvious dependence on separation. While HD 62542 has both the smallest separation from the nominal clump center and the largest $N(\text{CO})$, $N(\text{C I})$, $N(\text{CO})/N(\text{C I})$, $N(\text{CO})/N(\text{H}_2)$, and thermal pressure among the eight high $N(\text{CO})$ sight lines, those values likely are largely driven by the enhanced density (due to the special environmental circumstances) and steep far-UV extinction rather than by cloud structure (as might be characterized by separation/proximity).

Much more limited information is available for assessing the physical conditions in the other, lower $N(\text{H}_{\text{tot}})$ components toward HD 62542, as no molecular species and few of the trace neutral species are detected there. If the strongest of those lower $N(\text{H}_{\text{tot}})$, primarily atomic components (at $\sim 27 \text{ km s}^{-1}$) is taken as representative, then the measured line widths and the C I fine-structure excitation suggest that they are likely to be warmer and much less dense than the main component.

¹⁰Based on the estimate for $\log[N_{\text{m}}(\text{C II})] \sim 17.4$ given in Sec. 3.2.1 and the measured values for $\log[N_{\text{m}}(\text{CO})] = 16.42$ and $\log[N_{\text{m}}(\text{C I})] = 15.41$

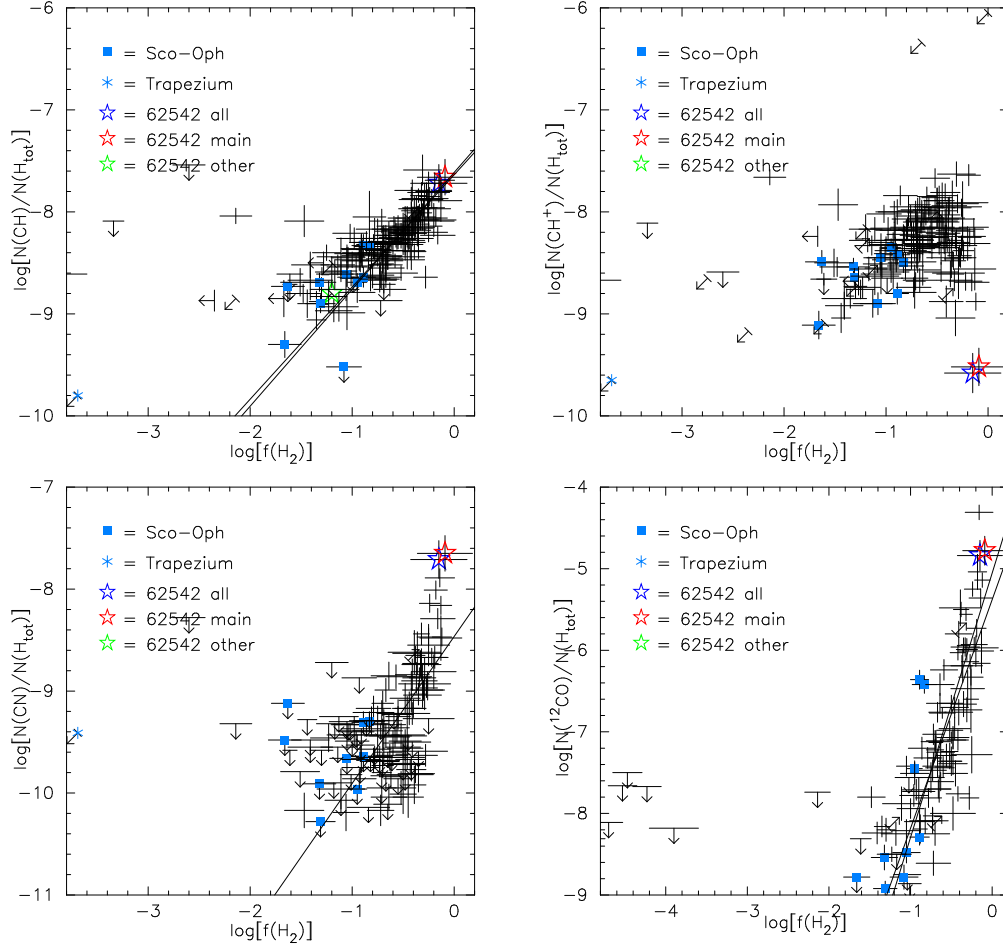


Fig. 17.— Normalized abundances $N(X)/N(H_{\text{tot}})$ for molecular species CH, CH^+ , CN, and ^{12}CO versus molecular fraction $f(\text{H}_2)$. The stars denote the sight line toward HD 62542: red = main (14 km s^{-1}) component; green = all other components; blue = all components. The other symbols are for sight lines in the Galactic ISM – mostly from Sonnentrucker et al. (2007) and Sheffer et al. (2008). The solid lines represent weighted and unweighted fits to the data, for $f(\text{H}_2) > 0.1$. The normalized abundances of CH, CN, and CO increase with molecular fraction for $f(\text{H}_2) > 0.1$; the normalized abundance of CH^+ exhibits an initial increase, but then decreases for $f(\text{H}_2) \gtrsim 0.3$.

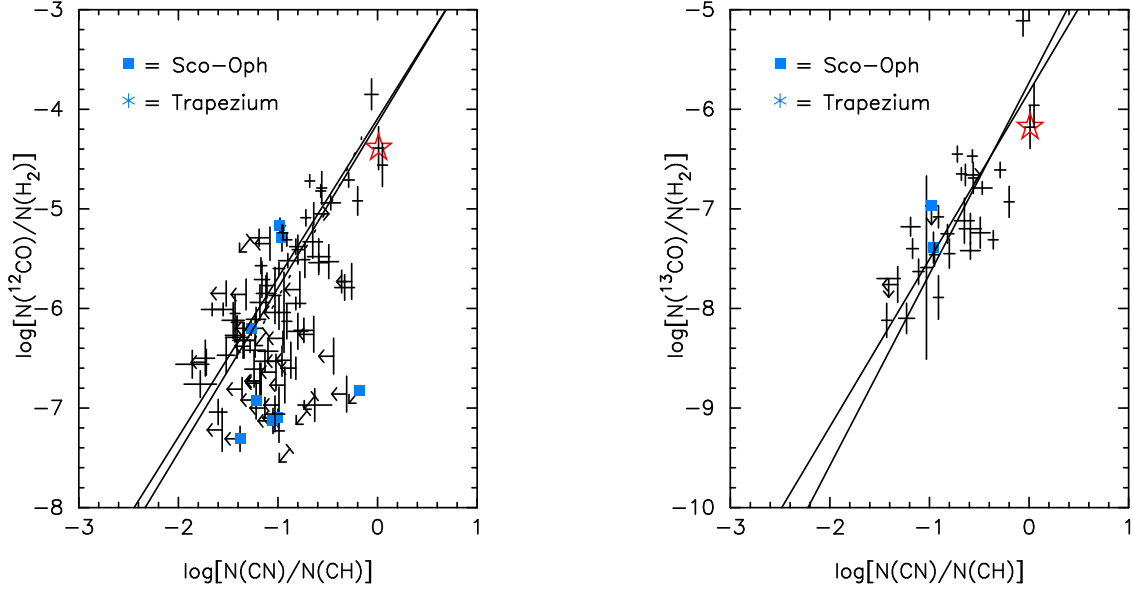


Fig. 18.— $N(^{12}\text{CO})/N(\text{H}_2)$ (*left*) and $N(^{13}\text{CO})/N(\text{H}_2)$ (*right*) vs. $N(\text{CN})/N(\text{CH})$. The sight line to HD 62542 is denoted by the open star. The $N(\text{CN})/N(\text{CH})$ ratio is thought to be a density indicator; the abundances of both CO isotopologs increase nearly quadratically with that ratio.

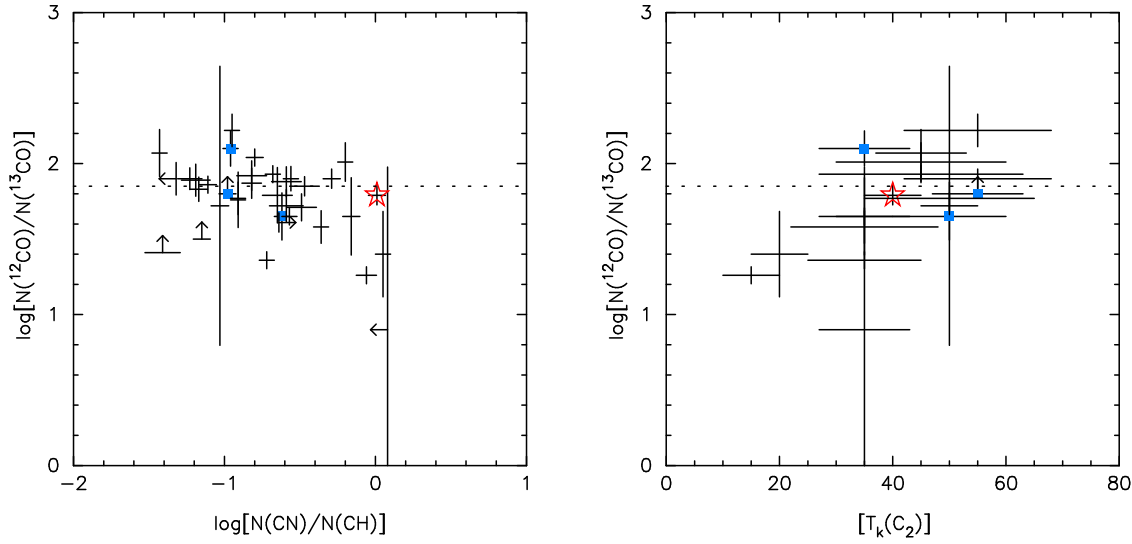


Fig. 19.— $N(^{12}\text{CO})/N(^{13}\text{CO})$ vs. $N(\text{CN})/N(\text{CH})$ (*left*) and $T_k(\text{C}_2)$ (*right*). The sight line to HD 62542 is denoted by the open star. The ratio of the two CO isotopologs decreases with the density indicator $N(\text{CN})/N(\text{CH})$ and increases with $T_k(\text{C}_2)$. Ratios less than the local Galactic $^{12}\text{C}/^{13}\text{C}$ ratio ~ 70 (dotted line) are likely due to isotopic charge exchange, which favors ^{13}CO at temperatures below about 35 K; higher ratios are likely due to selective photodissociation of ^{13}CO , as the more abundant ^{12}CO can self shield.

4.2. Molecular Abundances / Chemistry / Cloud Models

As discussed above, the optical/UV absorption lines detected for a number of molecular species in the main cloud toward HD 62542 have indicated high abundances of CH, CN, C₂, C₃, CS, NH, OH, and CO, but a very low abundance of CH⁺; those molecular detections have provided both qualitative and quantitative diagnostics for the conditions in and around that cloud. The fairly high (average) density suggested by both the high $f(\text{H}_2)$ and the relatively high observed C₃/C₂ and CN/CH ratios in the main cloud has been confirmed both by simple chemical models for the abundances of CH, C₂, and CN and by analyses of the excitation of C I, C₂, and CO (Sec. 4.1.2 above). The differences in b for CH, CN, C₂, and the CO isotopologs may indicate, however, that those molecular species are somewhat stratified within that primarily molecular cloud – with the species with smaller b progressively more centrally concentrated in colder, less turbulent inner regions of the cloud.

Figure 17 gives a slightly different view of the relationships between CH, CH⁺, CN, and CO and H₂ depicted above in Fig. 10, with both abscissa and ordinate in each case divided by $N(\text{H}_{\text{tot}})$ to yield some discrimination between sight lines containing gas with a significant molecular fraction and sight lines dominated by more diffuse, primarily atomic gas. The relationships for those normalized abundances of CH, CN, and CO versus $f(\text{H}_2)$ are similar to those seen for the unnormalized abundances versus $N(\text{H}_2)$, and the normalized abundances of those molecules in the main cloud toward HD 62542 are quite consistent with the trends seen for other sight lines with relatively high $f(\text{H}_2)$ (thought to be indicative of higher local densities). For CH⁺, however, the normalization reveals the "lambda-shaped" behavior noted by Fan et al. (2017) for many of the DIBs and for some atomic and molecular species. An initial rise in the CH⁺ abundance with increasing $f(\text{H}_2)$ is followed by a steep decline for $f(\text{H}_2) \gtrsim 0.3$ – likely reflecting the rapid destruction of CH⁺ in denser gas.

The presence of a single narrow, dominant component (at the same velocity) for both the absorption and the emission toward HD 62542 and the agreement between the CO column densities derived from the absorption and emission spectra suggest that both the absorption and emission are due to the same main cloud, foreground to the star. The availability of abundances for a number of atomic and molecular species (yielding multiple diagnostics), the constraints on the radiation field and the cosmic-ray ionization rate, and the observations of molecular emission from both the line of sight and the surrounding region (Gredel et al. 1994) suggest that detailed models of that main cloud could be both reasonably well constrained and quite informative. While we defer the exploration and discussion of such detailed physical/chemical models to a subsequent paper, we will briefly note some implications of the unusually low observed CH⁺ abundance and of the isotopic ratios observed for CO.

4.2.1. CH^+ Abundance

Because of its slow formation in steady-state chemical models and its rapid destruction (via collisions with H, H_2 , and electrons), various nonthermal processes have been proposed to account for the large observed interstellar abundances of CH^+ (e.g., Elitzur & Watson 1978; Draine & Katz 1986; Falgarone et al. 1995; Federman et al. 1996; Godard et al. 2009, 2014; Agundez et al. 2010; Myers et al. 2015; Valdivia et al. 2017). While the CH^+ abundance observed toward HD 62542 is a factor ~ 30 below the "typical" $N(CH^+)/N(H_{\text{tot}}) \sim 10^{-8}$ (e.g., Godard et al. 2014), even that small amount of CH^+ may be difficult to explain. Despite the apparent effects of stellar winds on the gas and dust in the vicinity of HD 62542, the lack of velocity differences among the various atomic and molecular species and the observed severe depletions suggest that the CH^+ is not produced by shocks. Both CH^+ and (undetected) SH^+ can be enhanced in the presence of H_2^* (e.g., Agundez et al. 2010), but those models suggest that more H_2^* than is seen toward HD 62542 would be needed to produce the observed CH^+ . Turbulent dissipation has been suggested to produce CH^+ (e.g., Godard et al. 2014), but that process is inefficient at densities above about 300 cm^{-3} . While the main cloud toward HD 62542 is much denser ($n_H \sim 1500 \text{ cm}^{-3}$), the weak observed CH^+ could be concentrated in its thin, lower density outer layers.

4.2.2. Isotopic Ratios

While CO and its isotopologs are often used to estimate the amount of molecular gas when H_2 cannot be measured directly via far-UV absorption, interpretation of the mm-wave CO emission-line data can be uncertain, due to differences in distribution, saturation, and fractionation among the isotopologs. Interpretation of the CO absorption lines observed in UV spectra is fairly straightforward, however. In the absence of fractionation, the $^{12}\text{CO}/^{13}\text{CO}$ ratio would equal the typical Galactic $^{12}\text{C}/^{13}\text{C}$ ratio of about 70. Because CO is photodissociated via line absorption in various UV and far-UV bands, $N(\text{CO})$ will increase rapidly if those lines either become saturated or are shielded by other strong lines (e.g., of H I or H_2). This shielding is quite effective for the more abundant ^{12}CO , but not for the other isotopologs. In denser, colder gas ($T_k \lesssim 35 \text{ K}$), however, isotope exchange reactions favor the production of ^{13}CO (Watson et al. 1976; Federman et al. 2003). Translucent cloud models (Warin et al. 1996; Visser et al. 2009) predict a somewhat complex dependence of the $^{12}\text{CO}/^{13}\text{CO}$ ratio on n_H , T_k , and A_V , with $^{12}\text{CO}/^{13}\text{CO}$ reaching a minimum value of about one-fifth the typical interstellar value for n_H of order 1000 cm^{-3} and $A_V \sim 1.5\text{--}2.0$, but then returning gradually to the typical interstellar value for thicker clouds.

Absorption from ^{12}CO , ^{13}CO , and C^{18}O has been detected in the main component toward HD 62542, with $^{12}\text{CO}/^{13}\text{CO}$ ($\sim 62 \pm 8$) and $^{12}\text{CO}/\text{C}^{18}\text{O}$ ($\sim 3550 \pm 780$); both ratios are similar to those found toward X Per (Sheffer et al. 2002b). Figures 18 and 19 show the observed abundances of ^{12}CO and ^{13}CO and the ratio $^{12}\text{CO}/^{13}\text{CO}$ versus the CN/CH ratio (thought to be $\propto n_H^2$). The abundances of both CO isotopologs appear to increase fairly strongly with density, so that ^{12}CO

may contain $\sim 10\%$ of the total gas-phase carbon toward HD 62542 and HD 73882 – both with $\log(\text{CN}/\text{CH}) \sim 0$ and $f(\text{H}_2) > 0.65$. For the three points in Figure 19 with the largest $^{12}\text{CO}/^{13}\text{CO}$ ratios (and small CN/CH ratios), Federman et al. (2003) proposed that the $^{12}\text{CO}/^{13}\text{CO}$ ratio is controlled largely by selective photodissociation — dependent on the ratio of $N(\text{CO})$ to the strength of the ambient radiation field. Inclusion of additional data, however, suggests some dependence on the density (from the CN/CH ratio) and T_k (from C_2 excitation; Sonnentrucker et al. 2007) – and the importance of isotope exchange reactions – with a minimum value similar to that predicted by the models. In both Figures 18 and 19, however, many of the points at highest CN/CH (and lowest $^{12}\text{CO}/^{13}\text{CO}$) are based on CO column densities derived from *IUE* data, and thus are somewhat uncertain. For $T_k \sim 40$ K, isotope exchange should not be significant in the main cloud toward HD 62542. The $N_m(^{12}\text{CO})/N_m(^{13}\text{CO}) \sim 62 \pm 8$ and $N_m(^{12}\text{CN})/N_m(^{13}\text{CN}) \sim 79 \pm 13$ ratios toward HD 62542 (versus the average $^{12}\text{C}/^{13}\text{C} \sim 70$) are consistent with the general anticorrelation between the two found by Ritchey et al. (2011) and ascribed to a ”competition” for the available ^{13}C between CN and the more abundant CO.

4.3. Depletions in Dense Gas

In the Galactic ISM, the apparent association of more severe depletions with both high $f(\text{H}_2)$ and high average sight-line densities $\langle n_{\text{H}} \rangle$ (Jenkins 1987, 2009; Cardelli 1994; Cartledge et al. 2006) is usually taken to indicate a relationship between the depletions and the *local* n_{H} . Moreover, consideration of the time scales for grain formation (e.g., in stellar outflows) and grain destruction (e.g., in interstellar (IS) shocks) seems to require significant (re)construction of grains in the denser IS clouds (e.g., Draine 1990). It was therefore initially somewhat surprising that the Fe depletions found for sight lines in the *FUSE* translucent cloud sample were not more severe than the highest values determined from *Copernicus* observations of less-reddened sight lines (Snow et al. 2002a). It has become apparent, however, that most ”translucent” sight lines actually contain mixtures of dense and diffuse gas – and that both the high $f(\text{H}_2)$ and the very severe depletions expected for any dense, translucent gas can be masked by blending in integrated sight-line averages (Rachford et al. 2002, 2009; Sonnentrucker et al. 2002, 2003). For example, if a sight line contains 20% diffuse H I gas with a ”warm, diffuse cloud” iron depletion $D(\text{Fe}) = -1.4$ dex and 80% dense molecular gas with *no* Fe in the gas phase, the average sight-line $D(\text{Fe}) = -2.1$ dex — slightly *less* severe than that observed for the “cold clouds” toward ζ Oph. The sight line toward HD 62542 – dominated by a single relatively dense, primarily molecular core – may provide one of the best current opportunities for finding the more extreme depletions expected if grains grow in dense clouds.

In a survey of the abundances of 17 elements in 243 sight lines primarily probing the relatively local Galactic ISM, Jenkins (2009) proposed a single parameter (F_*), based on the depletions found for the various elements in a given sight line (and an assumption of similar relative depletion patterns), to describe the overall level of depletion in that sight line. Ritchey et al. (2018) have extended the sample to include the abundances of five additional heavier neutron-capture elements

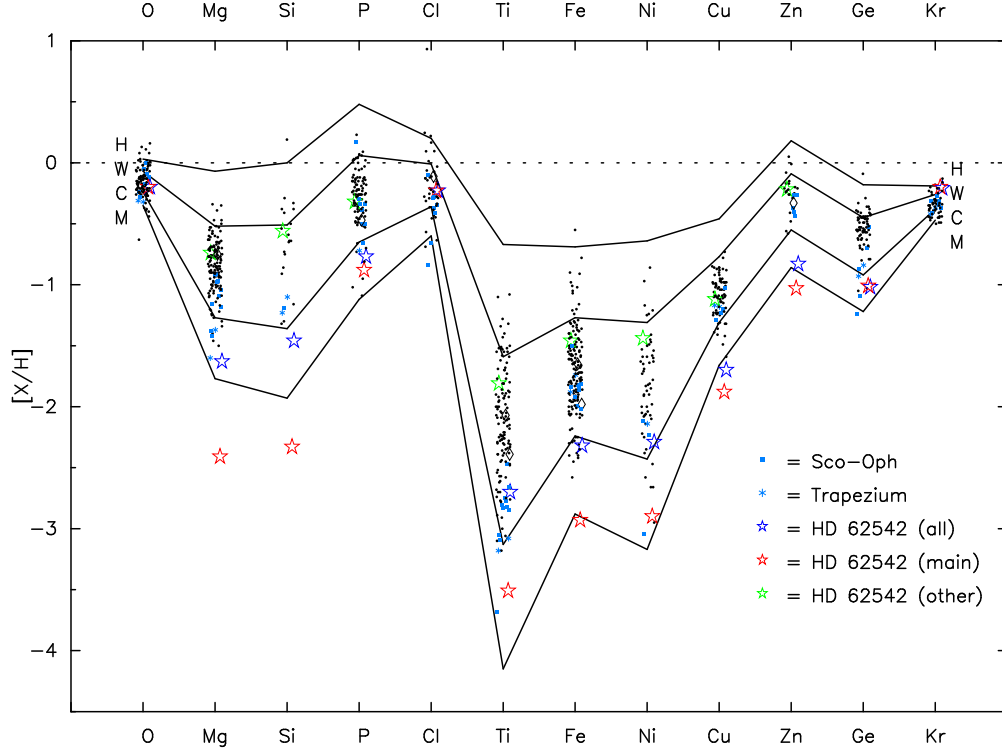


Fig. 20.— Depletions of selected elements ($[X/H] = \log(X/H)_{\text{obs}} - \log(X/H)_{\odot}$) toward HD 62542. The red stars are for the main component near 14 km s^{-1} ; the green stars are for the sum of the other components; the blue stars are for the whole sight line. The other symbols are for other Galactic sight lines, mostly from Welty & Crowther (2010; Ti) and Jenkins (2009; all other elements). The solid lines give representative depletion patterns for depletion parameters $F^* = -0.2, 0.25, 1.0,$ and 1.5 (Jenkins 2009) – loosely characterized as “halo cloud” (H), “warm cloud” (W), “cold cloud” (C), and “molecular cloud” (M), respectively; the first three of those are similar to previous empirically defined patterns (e.g., Savage & Sembach 1996; Welty et al. 1999). The main component is assumed to contain all the observed H_2 (and some H); the other components contain primarily atomic hydrogen. While many of the main-component depletions lie between the “cold cloud” and “molecular cloud” values, the depletions of Mg and Si are more severe than the ‘molecular cloud’ values and the depletions of Cl and Kr are less severe than the “cold cloud” values. The average depletions for the other components are generally slightly more severe than the “warm cloud” values, with $F_* \sim 0.28$.

(Ga, As, Cd, Sn, Pb), plus the light element boron, in 118 sight lines. In the formulation of Jenkins (2009), the logarithmic depletions of individual elements appear to be roughly linearly related to F_* , with slopes A_X (obtained from the data for the entire sample) ranging from about 0.0 for little-depleted nitrogen and cadmium to about -2.0 for severely depleted titanium (with some scatter). For well-defined F_* , the values range from about -0.4 [for the very mild depletions in the low- $N(\text{H}_{\text{tot}})$ sight line toward β CMa] to about 1.15 (for the severe depletions found toward HD 37903 and HD 110432). Previously used representative Galactic "halo cloud", "warm cloud", and "cold cloud" depletion patterns (e.g., Savage & Sembach 1996; Welty et al. 1999) correspond (roughly) to depletion levels $F_* \sim -0.20, 0.25,$ and 1.0 , respectively. For comparison with the more severe depletions seen toward HD 62542, we adopt a fourth pattern, defined by $F_* = 1.5$, for "molecular clouds".

For this study, we have also adopted a somewhat different depletion slope for chlorine than that derived by Jenkins (2009). While Cl^+ is the dominant form of chlorine in primarily atomic gas (and was the only form of chlorine considered in Jenkins 2009), Cl^0 can become dominant in gas with an appreciable molecular fraction, due to a reaction between Cl^+ and H_2 (e.g., Jura 1974). Using a set of sight lines with data for both Cl^0 and Cl^+ , we have therefore estimated the depletion slope for the total amount of chlorine in the predominantly neutral gas in those sight lines. The resulting value, $A_{\text{Cl}} = -0.60$, fits the general trend of A_X with condensation temperature (Fig. 15 in Jenkins 2009) much better than the previous value (-1.24). In view of the high $f(\text{H}_2)$ in the main component toward HD 62542, we assume that Cl^0 is the dominant form of chlorine there; any Cl^+ in that component would only increase the total chlorine abundance (making the depletion even milder). In addition, consideration of larger samples of data for Ti II (Welty & Crowther 2010) and Kr I (Ritchey et al. 2018) suggests that the A_X derived by Jenkins (2009) for those two elements may also be too small, by ~ 0.2 and 0.1 , respectively – especially if the apparently somewhat anomalous Sco-Oph sight lines (e.g., Figs. 7 and 21; Sec. 4.3.2) are excluded from the fits. Slightly higher A_X values for Ti and Kr would be in better agreement with the slopes for the depletions of those two elements versus $f(\text{H}_2)$, as seems to be the case for a number of other elements (see Fig. 23 and Sec. 4.3.2 below).

4.3.1. HD 62542 – Dominant Species

Figure 20 shows the depletions toward HD 62542 for most of the elements considered by Jenkins (2009) – for the main component near 14 km s^{-1} (red star), for the sum of the other predominantly neutral components (green star), and for the sight line as a whole (blue star; Table 3), compared with those found for other Galactic sight lines and with the four representative Galactic depletion patterns. The small black circles represent the integrated sight-line values for the other Galactic sight lines (Jenkins 2009; Welty & Crowther 2010); their concentration between the "warm cloud" and "cold cloud" patterns is likely due (at least in part) to the averaging over all the individual components in each sight line. For the main component toward HD 62542, in which most of the

hydrogen is in molecular form, the depletions range from very mild (~ -0.3 dex for O, Cl, and Kr) to very severe ($\lesssim -2.3$ dex for the more refractory elements Mg, Si, Ti, Fe, and Ni). Using the coefficients listed in Table 4 of Jenkins (2009; except for Cl) and Table 8 of Ritchey et al. (2018), the depletions toward HD 62542 may be converted to corresponding F_* values for elements exhibiting significant ranges in depletion in those surveys. For the main component P, Ti, and Ni, F_* ranges from about 1.2 to 1.3, corresponding to "cold cloud" depletions. For the main component Mg, Si, Fe, Cu, Ga, and Ge, however, F_* ranges from about 1.5 to 2.1 – more consistent with the "molecular cloud" depletions. The ratio $N_m(\text{Ca I})/N_m(\text{Ca II}) \sim 0.005$ for the main component suggests that most of the calcium there is in Ca^+ – and thus that calcium is severely depleted there as well (Table 3; see Welty et al. 2003). Taken together, the depletions of the more refractory elements in the main cloud toward HD 62542 thus are more severe than those found (so far) in typical Galactic "cold clouds" – by nearly a factor of 10 for Mg and Si – and are more severe than nearly all of the depletions for those elements in the Jenkins (2009) and Ritchey et al. (2018) samples. For most of the elements detected in the main component – including undepleted Cd and modestly depleted O, Zn, and Sn – the depletions are reasonably consistent with the $F_* \sim 1.52$ estimated above (Sec. 3.1; Fig. 6); the upper limits for B, As, and Pb are also consistent (but not very restrictive), given the trends for those elements found by Ritchey et al. (2018). Curiously, however, the main-component depletions of both Mg and Si are more severe, and those of Cl and Kr are milder, than would be expected for that F_* . Those differences for Mg, Si, Cl, and Kr (and, to a lesser extent, for P, Ti, and Ni) indicate that the detailed pattern of depletions in the main component toward HD 62542 differs somewhat from those previously defined from general trends in the Galactic interstellar abundances. The depletions in the other components toward HD 62542 are much less severe than those in the main component – generally slightly more severe than the "warm cloud" pattern, consistent with the $F_* = 0.28$ estimated above (Sec. 3.1; Fig. 6).

The significant differences in depletions between the main component and the other components toward HD 62542 suggest that care must be taken in interpreting total, integrated sight-line values for this sight line. While the depletions for the sight line as a whole are broadly similar to the "cold cloud" pattern (with estimated $F_* \sim 0.85$ – i.e., between the depletions found for the main component and for the other components), the $N(\text{H}_{\text{tot}})$ predicted from the total-sight line column densities via the procedure described in Jenkins (2009) is nearly a factor of 2 smaller than the sum of the values obtained separately for the main component and for the other components (Sec. 3.1). In this particular case, the total column densities for the least-depleted elements (O, Kr, Cd) are dominated by the contributions from the main component, while the total column densities for the more severely depleted elements (Ti, Fe, Ni) are dominated by the contributions from the other, lower $N(\text{H}_{\text{tot}})$ components – so that the relationship used to estimate F_* and $N(\text{H}_{\text{tot}})$ (as in Fig. 6) is not consistent with a single value of the slope F_* (see also section 7.2 and figure 9 in Jenkins 2009). Even though the main component dominates the total H_{tot} toward HD 62542, both the unusually severe depletions and the deviations from the typical Galactic patterns found for that component might not have been suspected if only the integrated sight-line values were available.

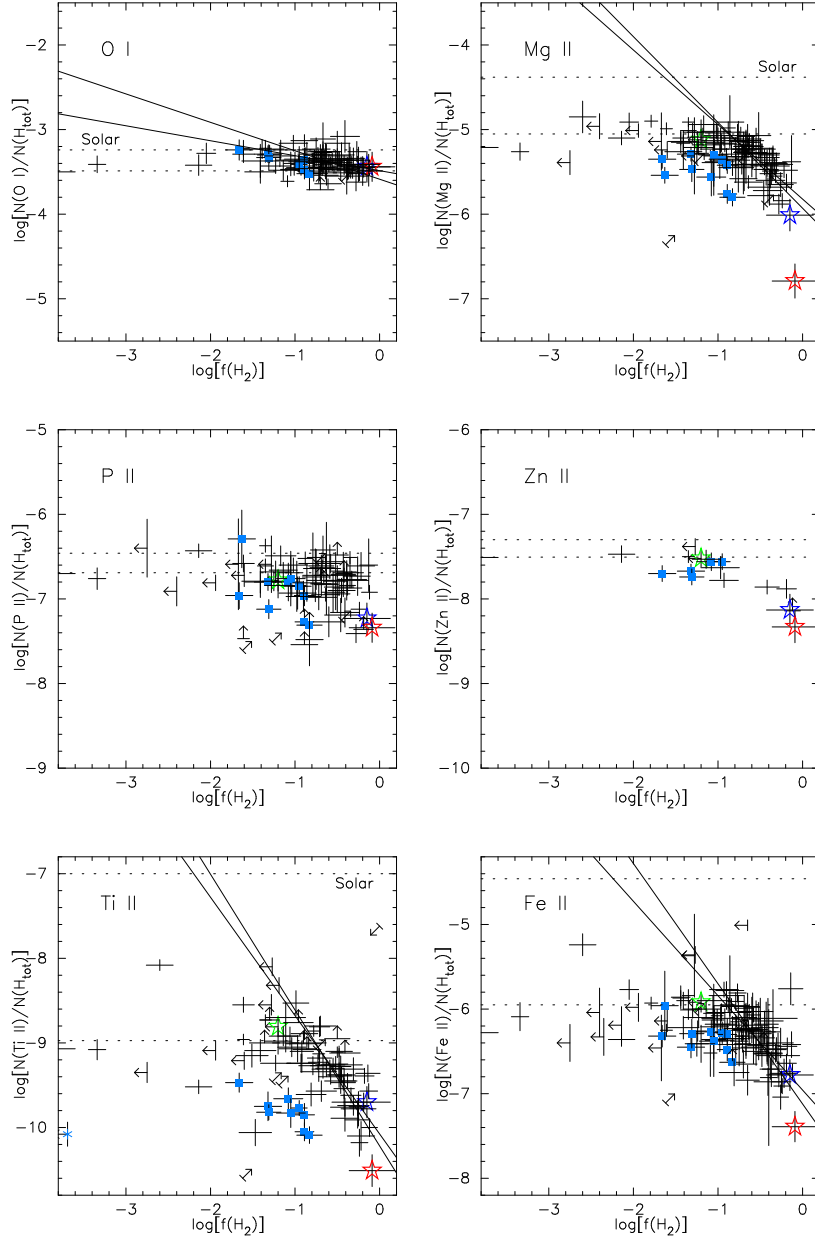


Fig. 21.— Normalized abundances of six dominant atomic species $N(X)/N(H_{\text{tot}})$ versus molecular fraction $f(H_2)$ (a proxy for the local hydrogen density). The stars denote the sight line toward HD 62542: red = main (14 km s^{-1}) component; green = all other components; blue = all components. The other symbols are for sight lines in the Galactic ISM – mostly from Welty & Crowther (2010) for Ti II and from Jenkins (2009) for the other species. The solid lines represent weighted and unweighted fits to the trends for $f(H_2) > 0.1$ (not including the Sco-Oph or Trapezium sight lines); the upper horizontal dotted lines mark the protosolar photospheric abundances (Lodders 2003); the lower horizontal dotted lines give the average values for $f(H_2) < 0.01$. The declines in the normalized abundances for $f(H_2) > 0.1$ reflect increasingly severe depletions in denser gas – particularly for Mg, Ti, and Fe. The depletions of several of these elements are more severe than usual for some Sco-Oph sight lines (blue squares) – and are even more severe in the main component toward HD 62542 (red stars).

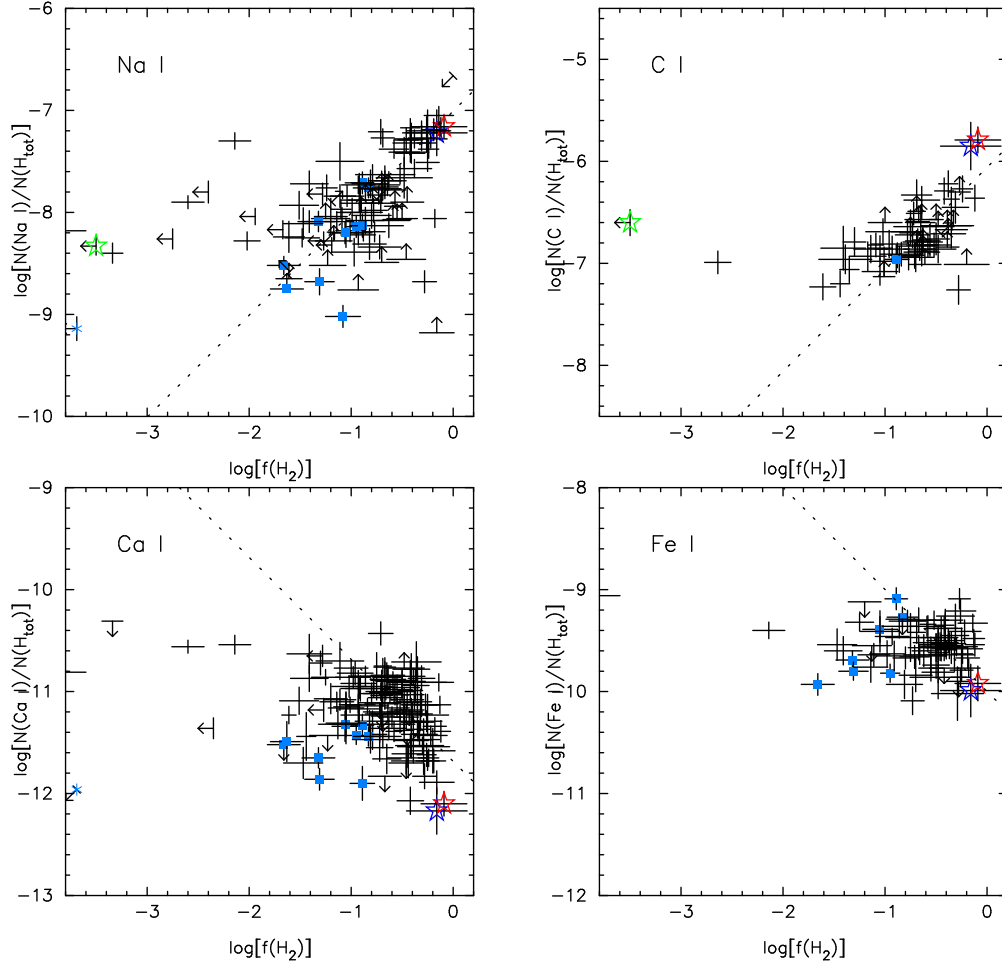


Fig. 22.— Normalized abundances of four trace neutral atomic species $N(\text{X})/N(\text{H}_{\text{tot}})$ versus molecular fraction $f(\text{H}_2)$. The stars denote the sight line toward HD 62542: red = main (14 km s^{-1}) component; green = all other components; blue = all components. The other symbols are for sight lines in the Galactic ISM – mostly from Welty & Hobbs (2001), Jenkins & Tripp (2011), and Welty et al. (2016) for Na I and C I and from Welty et al. (2003) for Ca I and Fe I. The dotted lines have slopes of 1 (Na I, C I) or -1 (Ca I, Fe I). The differences in the behavior of those trace species for $f(\text{H}_2) > 0.1$ reflect differences in their ionization and depletion in denser gas.

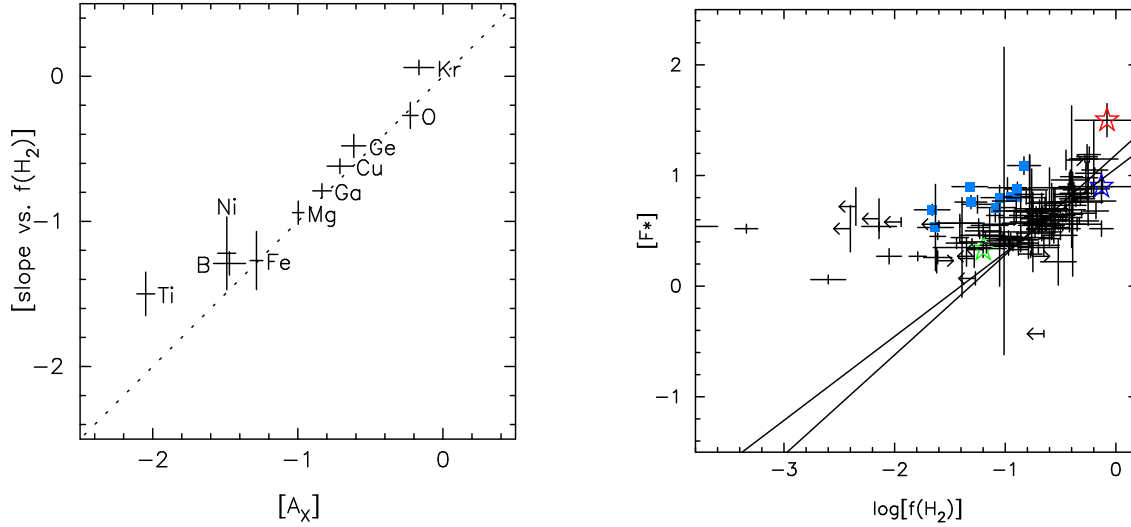


Fig. 23.— Comparisons of the slopes of the normalized column densities $N(X)/N(H_{\text{tot}})$ with respect to the molecular fraction $f(H_2)$ vs. the depletion slope parameter A_X (Jenkins 2009) (*left*) and the depletion index F_* (Jenkins 2009) vs. $f(H_2)$ (*right*). For the left-hand panel, the slopes for $N(X)/N(H_{\text{tot}})$ were determined for sight lines with $f(H_2) \geq 0.1$ (as in Fig. 21); the somewhat anomalous Sco-Oph sight lines were excluded from the fits. The values for most elements fall close to the dotted line denoting equality; the A_X values for Ti and Kr may be slightly too small (see Sec. 4.3). Elements not shown (e.g., C, Si, Mn, Zn) have too few accurate abundance determinations at high $f(H_2)$ for reliable slopes to be determined. In the right-hand panel, the open stars denote the values for HD 62542: main component (red), the sum of the other components (green), all components (blue). The fits (weighted and unweighted) again are for $f(H_2) \geq 0.1$, where the two quantities appear to be fairly well correlated. The Sco-Oph sight lines (solid blue squares) either have more severe depletions than other sight lines with comparable $f(H_2)$ or lower molecular fractions than other sight lines with comparable depletions.

Table 9. Ratios of Trace Neutral Species X I/K I (Main Component)

Element	A_{\odot}	χ_{ion} (eV)	$\Gamma/\alpha_t^{\text{a}}$		$N_{\text{m}}(\text{X I})$ (cm^{-2})	$N_{\text{m}}(\text{X II})$ (cm^{-2})	X I/K I		Diff ^c	D(main) ^d	
			D78	D78+2K50			Obs	(predicted) ^b (D78) (D78+2K50)			
C	8.46	11.26	2.3	25.1	15.41	[17.40]	3.33	3.26	2.91	0.42	[−0.25]
Na	6.37	5.14	0.5	2.9	14.04	...	1.96	1.81	1.76	0.20	...
Mg	7.62	7.65	2.5	10.5	13.81	14.41	1.73	2.39	2.44	−0.71	−2.40
Si	7.61	8.15	17.1	81.9	11.60	14.48	−0.48	1.54	1.54	−2.02	−2.32
P	5.54	10.49	4.0	36.7	12.01	13.86	−0.07	0.10	−0.18	0.11	−0.87
S	7.26	10.36	17.7	162.4	14.64	[16.10]	2.56	1.18	0.90	1.66	[−0.35]
K	5.18	4.34	2.2	10.6	12.08
Ca	6.41	6.11	16.2	58.4	9.10	11.41	−2.98	0.37	0.49	−3.47	...
Ti	5.00	6.82	3.7	18.7	<10.03	10.95	< −2.05	−0.41	−0.43	< −1.62	−3.50
Cr	5.72	6.77	70.3	351.4	<9.68	...	< −2.40	−0.96	−0.98	< −1.42	...
Mn	5.58	7.43	1.7	8.7	<10.67	<12.72	< −1.41	0.51	0.49	< −1.90	< −2.05
Fe	7.54	7.90	8.8	47.7	11.28	13.81	−0.80	1.76	1.71	−2.51	−2.92
Ni	6.29	7.63	2.0	9.8	<10.68	12.59	< −1.40	1.16	1.15	< −2.55	−2.89
Zn	4.70	9.39	14.1	126.6	12.13	12.87	0.05	−1.28	−1.56	1.61	−1.02

^aRatio of photoionization rate to radiative plus dielectronic recombination rate, at cloud center and for $T = 43$ K, for the Draine (1978) and the D78 plus $2 \times$ K50 radiation fields.

^bObserved ratios X I/K I and predicted ratios (assuming photoionization equilibrium and no depletion), for the D78 and D78+2K50 fields.

^cDifference between observed X I/K I and predicted value for D78+2K50 field.

^dObserved depletion in the main component (Table 3).

4.3.2. Depletions versus $f(\text{H}_2)$

Other aspects of the behavior of the depletions of various elements may be seen via plots of the normalized abundances $N(\text{X})/N(\text{H}_{\text{tot}})$ versus the molecular fraction $f(\text{H}_2)$, which can be taken as a rough proxy for the local density n_{H} (e.g., Cardelli 1994; Sofia et al. 1999; Cartledge et al. 2006; Fan et al. 2017). Figures 21 and 22 show examples of such comparisons for selected dominant and trace species, respectively. At low molecular fractions [$f(\text{H}_2) \lesssim 0.1$], the depletions exhibited by the dominant species are relatively constant (as marked by the lower horizontal dotted lines; though with considerable scatter), at levels broadly similar to the "warm cloud" values – so that $f(\text{H}_2)$ is not a good discriminant in that regime. For higher molecular fractions [$f(\text{H}_2) \gtrsim 0.1$], however, the depletions generally become more severe with increasing $f(\text{H}_2)$ – so that the molecular fraction does appear to provide a good discriminant where H_2 is significant – whether or not there is a direct relationship between the two quantities. Moreover, steeper slopes [fitting only sight lines with $f(\text{H}_2) \geq 0.1$] are found for the more refractory elements (compare Mg II, Ti II, Fe II versus O I, P II). Intriguingly, those slope values for $f(\text{H}_2) \geq 0.1$ are generally very similar to the corresponding A_{X} coefficients (the slopes of depletion versus F_*) in the Jenkins (2009) formalism (left-hand panel of Fig. 23) – though the samples are still small for some elements. That similarity likely reflects the fairly good correlation between F_* and $f(\text{H}_2)$ over that range in $f(\text{H}_2)$ (right-hand panel of Fig. 23) – though that relationship flattens out for smaller $f(\text{H}_2)$ (as in Fig. 16 of Jenkins 2009¹¹). Figure 22 shows that the normalized abundances of little-depleted trace species (C I, Na I) tend to increase monotonically with increasing molecular fraction for $f(\text{H}_2) \gtrsim 0.1$, while the normalized abundances of severely depleted trace species (Ca I, Fe I) tend to decline with molecular fraction (though not as severely as the corresponding dominant species; e.g., Fe I in Fig. 22 versus Fe II in Fig. 21). The figures also reveal the distinct behavior of the depletions and/or the molecular fractions in the Sco-Oph region (solid blue squares), where either the depletions of the more refractory species are more severe than for other sight lines with similar $f(\text{H}_2)$ or the molecular fractions are smaller than for other sight lines with similar levels of depletion. Some of the scatter seen in these comparisons is thus likely to reflect local/regional differences in environmental conditions. The locations of the HD 62542 main, other, and total sight-line values provide vivid illustrations of both the increasingly severe depletions at higher molecular fractions (higher densities?) and the tendency for the variations in the depletions among the individual components within a given sight line to be obscured in the integrated sight-line values.

4.3.3. HD 62542 – Trace Species

Additional information on the relative depletions of some elements may be obtained from ratios of the respective trace neutral species, which should preferentially trace the denser parts

¹¹Note that the values of $f(\text{H}_2)$ in that figure should all be multiplied by 2 (E. B. Jenkins 2020, private communication).

of interstellar clouds. In general, the relative abundances $N(X \text{ I})/N(Y \text{ I})$ should be relatively insensitive to n_e (which largely cancels in taking the ratios), T_k (due to most elements having similar temperature dependences for radiative recombination), and the overall strength (but perhaps not the shape) of the ambient UV radiation field (e.g., Snow 1984; Welty & Hobbs 2001; Welty et al. 2003). The column densities of the various trace neutral species are generally fairly well correlated with each other in the Galactic ISM (e.g., Jenkins & Shaya 1979), with slopes in $\log[N(X \text{ I})]$ versus $\log[N(K \text{ I})]$ (for example) of order 1.0 ± 0.5 (Welty & Hobbs 2001; Welty et al. 2003). The shallower slopes seen for Fe I and Ca I likely reflect the increasingly severe depletions of Fe and Ca in sight lines with higher $N(H_{\text{tot}})$. In the main component toward HD 62542, the trace neutral species with high ionization potentials $\chi_{\text{ion}} > 9 \text{ eV}$ (C I, P I, S I, Zn I) are all enhanced, relative to both K I (Table 9) and H_{tot} (Fig. 8) – likely due to selective suppression of ionizing photons by the steep far-UV extinction.¹² The trace neutral ions of the more refractory elements (Mg I, Si I, Ca I, Ti I, Cr I, Mn I, Fe I, Ni I), however, are all less abundant than "expected" or "usual" – consistent with the enhanced depletions of those elements inferred from the corresponding dominant first ions. The abundances of the trace neutral species thus reflect the effects of both the unusually severe depletions and the unusually steep far-UV extinction in the main component toward HD 62542.

4.3.4. Depletions and UV Extinction

There have been a number of attempts to tie unusual UV extinction to specific environmental conditions and/or other properties of the sight lines, in order to understand the size distribution and/or composition of interstellar dust grains. In a homogeneous survey of 417 Galactic sight lines observed with *IUE*, Valencic et al. (2004) identified four sight lines whose UV extinction curves could not be well fitted with the R_V -dependent parameterization developed by Cardelli et al. (1989): HD 29647, HD 62542, HD 204827, and HD 210121. All four of those "discrepant" sight lines exhibit both steep far-UV extinction and strong absorption from various molecular lines – suggestive of relatively high densities in the clouds. They appear to sample rather different environments, however – from apparently quiescent clouds in the disk (HD 29647) or low halo (HD 210121) to clouds that may have been subjected to shocks and/or stronger than average radiation fields (HD 62542, HD 204827). Because such steep UV extinction curves have been difficult to model with "standard" mixtures of graphite and silicate grains, they have been used to test more complex models for the interstellar dust – e.g., incorporating polycyclic aromatic hydrocarbons (PAHs) (e.g., Zonca et al. 2011) or nanodiamonds (Rai & Rastogi 2012). For HD 62542, those more complex models appear to prefer rather different mixtures of the silicate and total carbonaceous components. The observed very severe depletion of silicon in the main cloud toward HD 62542 indicates that silicates are likely to be major constituents of the dust

¹²While Cl I also has a fairly high ionization potential, its abundance is controlled by a reaction between H_2 and Cl II (Jura 1974). Given the high column density of Cl I (and the corresponding apparent negligible depletion of chlorine), the high molecular fraction in the main component appears to have driven most of the chlorine into Cl I.

there. Voshchinnikov & Henning (2010) noted a possible association between higher dust-phase abundances (i.e., more severe depletions) of Mg and Si, increased R_V , and flatter far-UV extinction for a few sight lines in the Sco-Oph region, which might be taken as evidence for growth of Mg-Si grains due to accretion. Although the depletions of Mg and Si are very severe in the main component toward HD 62542 – and coagulation and/or mantling of the grains might be expected in that relatively dense cloud – the overall $R_V \sim 2.9$ is close to the average local value, and the far-UV extinction is steep. Such steep far-UV extinction is often assumed to reflect an enhanced population of small grains – perhaps due to erosion of the grains by shocks or strong UV radiation – but the severe depletions of many elements (especially Mg and Si) and the absence of velocity offsets among the various atomic and molecular absorption lines suggests that the main cloud toward HD 62542 has not been strongly shocked, and the ambient UV field there appears to be only mildly enhanced. Voshchinnikov et al. (2012) then reported a weak correlation between the dust-phase abundance of Si and the interstellar polarization, suggesting that the silicate component of the grains would be primarily responsible for the polarization. Despite the severe depletions of Mg and Si in the main cloud toward HD 62542 (and the relative simplicity of the sight line), however, the measured polarization ($P = 1.42 \pm 0.01$ %; Voshchinnikov et al. 2012) due to that main cloud is unremarkable.

5. SUMMARY / CONCLUSIONS

High-resolution optical and UV spectra of the moderately reddened B3-5 V star HD 62542, located behind a ridge of gas and dust in the *IRAS* Vela shell, have yielded detections of interstellar absorption from many neutral and singly ionized atomic and molecular species. The interstellar material in this unusual sight line is dominated by an apparently single narrow "main" component near $v_{\odot} = 14 \text{ km s}^{-1}$ containing nearly 90% of the total $N(\text{H}_{\text{tot}})$ (seen most prominently in the molecular and trace neutral atomic species), but with a number of "other" components between about 4 and 33 km s^{-1} (seen primarily in some of the dominant singly ionized atomic species). The main component contains at least 99% of the H_2 (and other molecules) and roughly half of the atomic hydrogen (as estimated from several indicators) in the sight line, and is characterized by a very high molecular fraction $f(\text{H}_2) \sim 0.81$; it appears to be dominated by a relatively dense, mostly molecular core, with much of the usual more diffuse outer, primarily atomic gas having been stripped away by stellar winds and/or radiation from ζ Pup and γ^2 Vel. The rest of the atomic hydrogen in the sight line is distributed among the other components, with average $f(\text{H}_2) < 0.06$. Striking differences in the absorption-line profiles for lines from the various dominant species suggest large component-to-component differences in the relative abundances – and thus significant differences in the depletions of the more refractory elements.

The many atomic and molecular species detected in the main component provide multiple, independent diagnostics of the physical conditions in that primarily molecular cloud:

1. Analyses of the rotational excitation of H_2 (Rachford et al. 2002) and C_2 yield similar values for the kinetic temperature $T_{\text{k}} = 40\text{--}43 \text{ K}$; the higher value estimated from the low- J levels of C_3 (Ádámkóvics et al. 2003) likely reflects a radiative contribution to the excitation. Consistent upper limits on T_{k} are obtained from the $N(\text{O I}^*)/N(\text{O I}^{**})$ fine-structure ratio and from the b value (1.4 km s^{-1}) obtained from fits to the profiles of several lines from vibrationally excited H_2 . The unusually high (but subthermal) and uniform excitation temperatures T_{ex} found for both ^{12}CO (11.7 K; for $J=0\text{--}6$) and ^{13}CO (7.7 K; for $J = 0\text{--}3$) may be due to radiative (rather than collisional) excitation.
2. Analysis of the C I fine-structure excitation yields a well-constrained total hydrogen density $n_{\text{H}} \sim 1500 \text{ cm}^{-3}$, consistent with recent observations of C II] emission at $158 \mu\text{m}$ (Velusamy et al. 2017). The C_2 rotational excitation, for $J = 0\text{--}18$, is most consistent with $T_{\text{k}} \sim 40 \text{ K}$ and a density of collision partners (H and H_2) $n_{\text{c}} \sim 250 \text{ cm}^{-3}$ (for the average interstellar NIR radiation field); for $f(\text{H}_2) = 0.81$, that n_{c} implies $n_{\text{H}}/I_{\text{NIR}} \sim 430 \text{ cm}^{-3}$. Simple chemical models for the column densities of CH, C_2 , and CN suggest values for $n_{\text{H}}/I_{\text{UV}}$ ranging from $315\text{--}750 \text{ cm}^{-3}$. The lower densities inferred from C_2 and the chemical models may be reconciled with the 1500 cm^{-3} obtained from C I if the ambient radiation field is two to four times stronger than the average interstellar field (both in the near-IR and in the UV). Such an enhancement would be consistent with estimated contributions from ζ Pup and γ^2 Vel (whose stellar winds also appear to have shaped the ISM in the region).

3. The various available X I/X II ratios yield a wide range in implied n_e , from <0.1 to 2.6 cm^{-3} (assuming photoionization equilibrium in the average interstellar field); somewhat larger values of n_e – and larger ranges in n_e – are found if grain-assisted recombination, low-temperature dielectronic recombination, and an enhanced radiation field are considered. The pattern of relative n_e is not like those seen in many other sight lines, however; e.g., the value inferred from Ca (which is often anomalously high) is at the low end of the range toward HD 62542. The excitation of CN may be slightly higher than that expected from the CMBR, and yields an upper limit for $n_e < 1.2 \text{ cm}^{-3}$; the observed $n_H \sim 1500 \text{ cm}^{-3}$ would imply a lower limit of $n_e \gtrsim 0.24 \text{ cm}^{-3}$, assuming that most of the electrons come from ionization of carbon. The non-detection of OH^+ yields an upper limit on the cosmic-ray ionization rate, $\zeta_p < 3 \times 10^{-16} \text{ s}^{-1}$, that falls within the range seen for a number of other Galactic sight lines.

The strong observed absorption from CH, CN, C_2 , C_3 , and CO had hinted that the main cloud is relatively dense; the high CO/ H_2 and CO/C I ratios (as well as the high molecular fraction) suggest that it may be categorized as translucent (Burgh et al. 2010). The carbon in this largely molecular core is still primarily singly ionized, however, with $N(\text{C II}):N(\text{CO}):N(\text{C I})$ roughly 100:10:1. While the absorption from CH^+ is quite weak, relative to H_2 , even that small amount cannot be explained by reactions involving H_2^* (there is not enough present) or turbulent diffusion (which is ineffective at the high density characterizing the main cloud); the weak CH^+ may be concentrated in the remnant lower density, mostly atomic outer layers of the cloud. The $^{12}\text{C}/^{13}\text{C}$ isotopolog ratios for CO (~ 62) and CN (~ 79) appear to bracket the average local Galactic ratio ($^{12}\text{C}/^{13}\text{C} \sim 70$), consistent with the anticorrelation between those two isotopolog ratios noted by Ritchey et al. (2011) and ascribed to a competition between CO and CN for the available ^{13}C . The derived $T_k \sim 40\text{-}43 \text{ K}$ is not low enough for ^{13}CO to be significantly enhanced via isotope exchange.

For a number of the more refractory elements, the abundances of both trace and dominant ions indicate that the depletions characterizing the main component toward HD 62542 are more severe than those previously seen in any other Galactic sight line. We have thus adopted a new ”molecular cloud” pattern for the depletions, characterized by a depletion index $F_* = 1.5$ (in the formalism of Jenkins 2009) – but find that the detailed pattern of depletions in the main component is somewhat unusual (with respect to that pattern), with even more severe depletions for Mg and Si but very mild depletions for Cl and Kr. Neither those extreme depletions and nor the deviations from the typical Galactic pattern would have been noticed if we had considered only the total sight line abundances – for which the depletions are reasonably consistent with the well known ”cold cloud” pattern. Detailed, component-by-component analyses of high-resolution optical and UV spectra are needed to gauge the full range of relative abundances in the ISM (as well as to determine accurate physical conditions from the various diagnostics based on those abundances). Declining trends of the normalized abundances (X/H_{tot}) with $f(\text{H}_2)$ (taken as a rough proxy for the density), for $f(\text{H}_2) \gtrsim 0.1$, suggest that the depletions are more severe at higher densities; the slopes of those trends agree remarkably well with the depletion slopes determined by Jenkins (2009) and Ritchey et al. (2018). There is no obvious connection between the very severe depletions for Mg and Si in

the main component and either the extinction characterizing the sight line (steep far-UV rise, but normal R_V) or the optical/UV polarization (which is unremarkable). The severe depletions and the lack of velocity offsets among the various atomic and molecular species suggest that strong shocks have not significantly affected the main cloud; the normal R_V suggests that coagulation has not significantly enlarged the dust grains (despite the fairly high local density in that cloud).

The relative simplicity of this sight line and the wealth of available information (and diagnostics) make the main cloud toward HD 62542 a good candidate for detailed modeling. The differences in the b values determined for CO (0.5 km s^{-1}), CN and C₂ (0.7 km s^{-1}), and CH (1 km s^{-1}) suggest that those molecular species are somewhat stratified within the main cloud – with the species with smaller b more concentrated in the denser and/or less turbulent part(s) of the cloud – so that inhomogeneous models will be needed. Detailed consideration of the radiation field (UV, near-IR, submm) will also be necessary, given the likely contributions from ζ Pup and γ^2 Vel, the unusually steep far-UV extinction, and the possible radiative excitation of CO and C₃. Such models, using the Cloudy and Meudon PDR codes, are being explored; it will be very interesting to see if those models can both account for the molecular abundances and reconcile the various observed X I/X II ratios – to better understand both the various diagnostics and the chemistry and ionization equilibrium in such interstellar clouds.

Support for *HST* guest observer program 12277 was provided by NASA through grant HST-GO-12277.008-A from the Space Telescope Science Institute, which is operated by the Association of Universities for Research in Astronomy, Inc., under NASA contract NAS 5-26555. We thank Ed Jenkins for pointing out recent work on low-temperature dielectronic recombination and for providing his code for computing O I fine-structure excitation, Bruce Draine for advice regarding the estimation of grain-assisted recombination rates, Adam Ritchey for comments on O I, and Steve Federman for alerting us to an updated f value for CS and for useful comments.

Facilities: *HST* (STIS), ESO: 3.6m (CES), VLT: Kueyen (UVES), Keck:I (HIRES), AAT (UCLES), Magellan: Clay (MIKE)

REFERENCES

- Abdel-Naby, Sh. A., Nicolić, D., Gorczyca, T. W., Korista, K. T., & Badnell, N. R. 2012, *A&A*, 537, A40
- Abel, N. P., Ferland, G. J., O’Dell, C. R., & Troland, T. H. 2016, *ApJ*, 819, 136
- Abgrall, H., Roueff, E., Launay, F., & Roncin, J.-Y. 1994, *CaJPh*, 72, 856
- Ádámkóvics, M., Blake, G. A., & McCall, B. J. 2003, *ApJ*, 595, 235
- Ádámkóvics, M., Blake, G. A., & McCall, B. J. 2005, *ApJ*, 625, 857
- Agundez, M., Goicoechea, J. R., Cernicharo, J., Faure, A., & Roueff, E. 2010, *ApJ*, 713, 662
- Allison, A. C., & Dalgarno, A. 1971, *A&A*, 13, 331
- Andersson, B.-G., Wannier, P. G., & Morris, M. 1991, *ApJ*, 366, 464
- Arnaud, M., & Rothenflug, R. 1985, *A&AS*, 60, 425
- Bacalla, X. L., Linnartz, H., Cox, Nick L. J., et al. 2019, *A&A*, 622, A31
- Badnell, N. R. 2006, *ApJS*, 167, 334
- Badnell, N. R., O’Mullane, M. G., Summers, H. P. et al. 2003, *A&A*, 406, 1151
- Bahcall, J. N., & Wolf, R. A. 1968, *ApJ*, 152, 701
- Balona, L. A. 1975, *Mem. R. Astron. Soc.*, 78, 51
- Bautista, M. A., Romano, P., & Pradhan, A. K. 1998, *ApJS*, 118, 259
- Berengut, J. C., Flambaum, V. V., & Kozlov, M. G. 2006, *Phys. Rev. A*, 73, 012504
- Black, J. H., & van Dishoeck, E. F. 1991, *ApJ*, 369, L9
- Bohlin, R. C., Savage, B. D., & Drake, J. F. 1978, *ApJ*, 224, 132
- Brooke, J. S. A., Ram, R. S., Western, C. M. et al. 2014, *ApJS*, 210, 23
- Bryans, P., Kreckel, H., Roueff, E., Wakelam, V., & Savin, D. W. 2009, *ApJ*, 694, 286
- Burgess, A. 1964, *ApJ*, 139, 776
- Burgh, E., France, K., & Jenkins, E. B. 2010, *ApJ*, 708, 334
- Burgh, E., France, K., & McCandliss, S. 2007, *ApJ*, 658, 446
- Cardelli, J. A. 1994, *Sci*, 265, 209
- Cardelli, J. A., Clayton, G. C., & Mathis, J. S. 1989, *ApJ*, 345, 245
- Cardelli, J. A., & Savage, B. D. 1988, *ApJ*, 325, 864
- Cardelli, J. A., Suntzeff, N. B., Edgar, R. J., & Savage, B. D. 1990, *ApJ*, 362, 551
- Cartledge, S. I. B., Lauroesch, J. T., Meyer, D. M., & Sofia, U. J. 2006, *ApJ*, 641, 327
- Casu, S., & Cecchi-Pestellini, C. 2012, *ApJ*, 749, A48
- Chappell, D., & Scalo, J. 2001, *ApJ*, 551, 712

- Churchwell, E., Winnberg, A., Cardelli, J., Cooper, G., & Suntzeff, N. B. 1996, *ApJ*, 469, 209
- Cox, N. L. J., Kaper, L., Foing, B. H., & Ehrenfreund, P. 2005, *A&A*, 438, 187
- Crawford, I. A. 1990, *Observatory*, 110, 145
- Danks, A. C., Federman, S. R., & Lambert, D. L. 1984, *A&A*, 130, 62
- Dekker, H., D’Odorico, S., Kaufer, A., Delabre, B., & Kotzlowski, H. 2000, *Proc. SPIE*, 4008, 534
- Destree, J. D., & Snow, T. P. 2009, *ApJ*, 697, 684
- Destree, J. D., Snow, T. P., & Black, J. H. 2009, *ApJ*, 693, 804
- Diplas, A., & Savage, B. D. 1994, *ApJS*, 93, 211
- Dirks, C, & Meyer, D. M. 2019, *ApJ*, 872, 140
- Draine, B, T. 1978, *ApJS*, 36, 595 (D78)
- Draine, B. T. 1990, in *Evolution of the Interstellar Medium*, ed. L. Blitz, (Astron. Soc. Pacific), p. 193
- Draine, B. T., & Katz, N. 1986, *ApJ*, 310, 392
- Eidelsberg, M., & Rostas, F. 2003, *ApJS*, 145, 89
- Elitzur, M., & Watson, W. D. 1978, *ApJ*, 222, L41
- Enard, D. 1982, *SPIE*, 331, 232
- Falgarone, E., Pineau des Forêts, G., & Roueff, E. 1995, *A&A*, 300, 870
- Fan, H., Welty, D. E., York, D. G. et al. 2017, *ApJ*, 850, 194
- Feast, M. W., Thackeray, A. D., & Wesselink, A. J. 1955, *MmRAS*, 67, 51
- Federman, S. R., Cardelli, J. A., van Dishoeck, E. F., Lambert, D. L., & Black, J. H. 1995, *ApJ*, 445, 325
- Federman, S. R., Knauth, D. C., Lambert, D. L., & Andersson, B.-G. 1997, *ApJ*, 489, 758
- Federman, S. R., Rawlings, J. M. C., Taylor, S. D., & Williams, D. A. 1996, *MNRAS*, 279, L41
- Federman, S. R., Lambert, D. L., Sheffer, Y., et al. 2003, *ApJ*, 591, 986
- Federman, S. R., Strom, C. J., Lambert, D. L. et al. 1994, *ApJ*, 424, 772
- Felenbok, P., & Roueff, E. 1996, *ApJ*, 465, L57
- Fitzpatrick, E. L. 1997, *ApJ*, 482, L199
- Fitzpatrick, E. L., & Massa, D. 2007, *ApJ*, 663, 320
- Fitzpatrick, E. L., & Spitzer, L. 1997, *ApJ*, 475, 623
- Friedman, S. D., York, D. G., McCall, B. J. et al. 2011, *ApJ*, 727, 33
- Gnaciński, P. 2009, *Acta Astron.*, 59, 325
- Gnaciński, P. 2011, *A&A*, 532, A122

- Gnaciński, P. 2013, *A&A*, 549, A37
- Godard, B., Falgarone, E., & Pineau des Forêts, G. 2009, *A&A*, 495, 847
- Godard, B., Falgarone, E., & Pineau des Forêts, G. 2014, *A&A*, 570, A27
- Goldsmith, P. F. 2013, *ApJ*, 774, 134
- Gordon, K. D., Cartledge, S., & Clayton, G. C. 2009, *ApJ*, 705, 1320
- Gredel, R., van Dishoeck, E. F., & Black, J. H. 1991, *A&A*, 251, 625
- Gredel, R., van Dishoeck, E. F., & Black, J. H. 1993, *A&A*, 269, 477
- Gredel, R., van Dishoeck, E. F., & Black, J. H. 1994, *A&A*, 285, 300
- Heays, A. N., Bosman, A. D., & van Dishoeck, E. F. 2017, *A&A*, 602, A105
- Heidarian, N., Irving, R. E., Federman, S. R. et al. 2017, *JPhB*, 50, 155007
- Heidarian, N., Irving, R. E., Ritchey, A. M. et al. 2015, *ApJ*, 808, 112
- Heiles, C., & Troland, T. H. 2003, *ApJ*, 586, 1067
- Herbig, G. H. 1968, *ZAp*, 68, 243
- Herbig, G. H. 1993, *ApJ*, 407, 142
- Hobbs, L. M. 1969, *ApJ*, 157, 135
- Hodges, J. N., Bittner, D. M., & Bernath, P. F. 2018, *ApJ*, 855, 21
- Hollenbach, D., Kaufman, M. J., Neufeld, D., Wolfire, M., & Goicoechea, J. R. 2012, *ApJ*, 754, 105
- Houk, N. 1978, Michigan catalogue of two-dimensional spectral types for the HD stars (Ann Arbor: Dept. of Astronomy, Univ. of Michigan)
- Hubeny, I., & Lanz, T. 1995, *ApJ*, 439, 875
- Hupe, R. C. Sheffer, Y., & Federman, S. R. 2012, *ApJ*, 761, 38
- Indriolo, N., Fields, B. D., & McCall, B. J. 2009, *ApJ*, 694, 257
- Indriolo, N., Geballe, T. R., Oka, T., & McCall, B. J. 2007, *ApJ*, 671, 1736
- Jenkins, E. B. 1987, in *Interstellar Processes*, ed. D. J. Hollenbach & H. A. Thronson, (Kluwer), p. 533
- Jenkins, E. B. 1996, *ApJ*, 471, 292
- Jenkins, E. B. 2009, *ApJ*, 700, 1299
- Jenkins, E. B., & Shaya, E. J. 1979, *ApJ*, 231, 55
- Jenkins, E. B., & Tripp, T. M. 2001, *ApJS*, 137, 297
- Jenkins, E. B., & Tripp, T. M. 2006, *ApJ*, 637, 548
- Jenkins, E. B., & Tripp, T. M. 2011, *ApJ*, 734, 65 (JT11)
- Jenkins, E. B., Drake, J. F., Morton, D. C. et al. 1973, *ApJ*, 181, L122

- Jensen, A. G., Rachford, B. L., & Snow, T. P. 2005, *ApJ*, 619, 891
- Jensen, A. G., Snow, T. P., Sonneborn, G., & Rachford, B. L. 2010, *ApJ*, 711, 1236
- Jura, M. 1974, *ApJ*, 190, L33
- Kalberla, P. M. W., Kerp, J., Haud, U., et al. 2016, *ApJ*, 821, 117
- Kaur, J., Gorczyca, T. W., & Badnell, N. R. 2018, *A&A*, 610, A41
- Kilkenny, D. 1978, *MNRAS*, 182, 629
- Kurucz, R. 1993, CD-ROM No. 13 (available at <http://archive.stsci.edu/hlsps/reference-atlases/cdbs/grid/k93mod>)
- Lan, T.-W., Ménard, B., & Zhu, G. 2015, *MNRAS*, 452, 3629
- Lanz, T., & Hubeny, I. 2007, *ApJS*, 169, 83
- Larsson & Siegbahn 1983a, *J. Chem. Phys.*, 79, 2270; 85, 4208
- Larsson & Siegbahn 1983b, *CP*, 76, 175
- Le Petit, F., Nehmé, C., Le Bourlot, J., & Roueff, E. 2006, *ApJS*, 164, 506
- Lien, D. J. 1984, *ApJ*, 284, 578
- Liszt, H. 2003, *A&A*, 398, 621
- Liszt, H. S. 2007, *A&A*, 476, 291
- Lodders, K. 2003, *ApJ*, 591, 1220
- Lyu, C.-H., Smith, A. M., & Bruhweiler, F. C. 2001, *ApJ*, 560, 865
- Mather, J. C., Fixsen, D. J., Shafer, R. A., Mosier, C., & Wilkinson, D. T. 1999, *ApJ*, 512, 511
- Mathis, J. S., Mezger, P. G., & Panagia, N. 1983, *A&A*, 128, 212 (MMP)
- Mazzitelli, G., & Mattioli, M. 2002, *Atomic Data and Nuclear Data Tables*, 82, 313
- Meyer, D. M., Lauroesch, J. T., Sofia, U. J., Draine, B. T., & Bertoldi, F. 2001, *ApJ*, 553, 59
- Meyer, D. M., & Roth, K. C. 1990, *ApJ*, 349, 91
- Meyer, D. M., & Roth, K. C. 1991, *ApJ*, 376, L49
- Miller, A., Lauroesch, J. T., Sofia, U. J., Cartledge, S. I. B., & Meyer, D. M. 2007, *ApJ*, 659, 441
- Morton, D. C. 1991, *ApJS*, 77, 119
- Morton, D. C. 2000, *ApJS*, 130, 403
- Morton, D. C. 2003, *ApJS*, 149, 205
- Morton, D. C., & Noreau, L. 1994, *ApJS*, 95, 301
- Myers, A. T., McKee, C. F., & Li, P. S. 2015, *MNRAS*, 453, 2747
- Najar, F., Ben Abdallah, D., Jaidane, N., & Ben Lakhdar, Z. 2008, *CPL*, 460, 31
- Najar, F., Ben Abdallah, D., Jaidane, N., et al. 2009, *J. Chem. Phys.*, 130, 204305
- Nussbaumer, H., & Storey, P. J. 1983, *A&A*, 126, 75

- O'Donnell, J. E., Cardelli, J. A., & Churchwell, E. 1992, *AJ*, 104, 2161
- Palazzi, E., Mandolesi, N., & Crane, P. 1992, *ApJ*, 398, 53
- Pan, K., Federman, S. R., Sheffer, Y., & Andersson, B.-G. 2005, *ApJ*, 633, 986
- Pan, K., Federman, S. R., & Welty, D. E. 2001, *ApJ*, 558, L105
- Péquignot, D., & Aldrovandi, S. M. V. 1986, *A&A*, 161, 169
- Pereyra, A., & Magalhaes, A. M., 2002, *ApJS*, 141, 469
- Pineau des Forêts, G., Roueff, E., & Flower, D. R. 1986, *MNRAS*, 223, 743
- Planck Collaboration, Ade, P. A. R., Aghanim, N., et al. 2016, *A&A*, 594, A28
- Porras, A. J., Federman, S. R., Welty, D. E., & Ritchey, A. M. 2014, *ApJ*, 781, L8
- Prochaska, J. X., Chen, H.-W., & Bloom, J. S. 2006, *ApJ*, 648, 95
- Rachford, B. L., Snow, T. P., Destree, J. D. et al. 2009, *ApJS*, 180, 125
- Rachford, B. L., Snow, T. P., Tumlinson, J. et al. 2002, *ApJ*, 577, 221
- Rai, R. K., & Rastogi, S. 2012, *MNRAS*, 423, 2941
- Ritchey, A. M., Federman, S. R., & Lambert, D. L. 2011, *ApJ*, 728, 36
- Ritchey, A. M., Federman, S. R., & Lambert, D. L. 2018, *ApJS*, 236, 36
- Ritchey, A., Jenkins, E., & Federman, S. 2019, AAS meeting 233, 411.07
- Roth, K. C., & Meyer, D. M. 1995, *ApJ*, 441, 129
- Roueff, E. 1996, *MNRAS*, 279, L37
- Sahu, M. 1992, Ph.D. Thesis, University of Groningen
- Savage, B. D., Bohlin, R. C., Drake, J. F., & Budich, W. 1977, *ApJ*, 216, 291
- Savage, B. D., & Panek, R. J. 1974, *ApJ*, 191, 659
- Savage, B. D., & Sembach, K. R. 1996, *ARA&A*, 34, 279
- Sembach, K. R., & Savage, B. D. 1992, *ApJS*, 83, 147
- Sheffer, Y., & Federman, S. R. 2007, *ApJ*, 659, 1352
- Sheffer, Y., Federman, S. R., & Lambert, D. L. 2002a, *ApJ*, 572, L95
- Sheffer, Y., Lambert, D. L., & Federman, S. R. 2002b, *ApJ*, 574, L171
- Sheffer, Y., Rogers, M., Federman, S. R. et al. 2008, *ApJ*, 687, 1075
- Shull, J. M., & Beckwith, S. 1982, *ARA&A*, 20, 163
- Shull, J. M., & Van Steenberg, M. 1982, *ApJS*, 48, 95
- Smith, P. L., & Parkinson, W. H. 1978, *ApJ*, 223, L127
- Snow, T. P. 1984, *ApJ*, 287, 238
- Snow, T. P., & McCall, B. J. 2006, *ARA&A*, 44, 367

- Snow, T. P., Rachford, B. L., & Figoski 2002a, *ApJ*, 573, 662
- Snow, T. P., Welty, D. E., Thorburn, J. et al. 2002b, *ApJ*, 573, 670
- Sofia, U. J., Lauroesch, J. T., Meyer, D. M., & Cartledge, S. I. B. 2004, *ApJ*, 605, 272
- Sofia, U. J., Meyer, D. M., & Cardelli, J. A. 1999, *ApJ*, 522, L137
- Sonnentrucker, P., Friedman, S. D., Welty, D. E., York, D. G., & Snow, T. P. 2002, *ApJ*, 576, 241
- Sonnentrucker, P., Friedman, S. D., Welty, D. E., York, D. G., & Snow, T. P. 2003, *ApJ*, 596, 350
- Sonnentrucker, P., Welty, D. E., Thorburn, J. A., & York, D. G. 2007, *ApJS*, 168, 58
- Stahl, O., & Wilson, T. L. 1992, *A&A*, 254, 327
- Thaddeus, P. 1972, *ARA&A*, 10, 305
- Thorburn, J. A., Hobbs, L. M., McCall, B. J. et al. 2003, *ApJ*, 584, 339
- Valdivia, V., Godard, B., Hennebelle, P. et al. 2017, *A&A*, 600, A114
- Valencic, L. A., Clayton, G. C., & Gordon, K. D. 2004, *ApJ*, 616, 912
- van Dishoeck, E. F. 1988, in *Rate coefficients in astrochemistry*, ed. T. J. Millar & D. A. Williams, (Dordrecht: Kluwer), p. 49
- van Dishoeck, E. F., & Black, J. H. 1982, *ApJ*, 258, 533
- van Dishoeck, E. F., & Black, J. H. 1988, *ApJ*, 334, 771
- van Dishoeck, E. F., & Black, J. H. 1989, *ApJ*, 340, 273
- van Dishoeck, E. F., Black, J. H., Phillips, T. G., & Gredel, R. 1991, *ApJ*, 366, 141
- van Dishoeck, E. F., & de Zeeuw, T. 1984, *MNRAS*, 206, 383
- Velusamy, T., Langer, W. D., Goldsmith, P. F., & Pineda, J. L. 2017, *ApJ*, 838, 165
- Verner, D. A., Ferland, G. J., Korista, K. T., & Yakovlev, D. G. 1996, *ApJ*, 465, 487
- Visser, van Dishoeck, E. F., & Black, J. H. 2009, *A&A*, 503, 323
- Vogt, S. S., Allen, S. L., Bigelow, B. C. et al. 1994, *Proc. SPIE*, 2198, 362
- Voshchinnikov, N. V., & Henning, Th. 2010, *A&A*, 517, A45
- Voshchinnikov, N. V., Henning, Th., Prokopjeva, M. S., & Das, H. K. 2012, *A&A*, 541, A52
- Vreeswijk, P. M., Ledoux, C., Smette, A. et al. 2007, *A&A*, 468, 83
- Walker, D. D., & Diego, F. 1985, *MNRAS*, 217, 355
- Wannier, P. G., Andersson, B.-G., Penprase, B. E., & Federman, S. R. 1999, *ApJ*, 510, 291
- Wannier, P., Penprase, B. E., & Andersson, B.-G. 1997, *ApJ*, 487, L165
- Warin, S., Benayoun, J. J., & Viala Y. P. 1996, *A&A*, 308, 535
- Watson, W. D., Anicich, V. G., & Huntress, W. T., Jr. 1976, *ApJ*, 205, L165
- Weingartner, J. C., & Draine, B. T. 2001, *ApJ*, 563, 842

- Welty, D. E. 2014, in IAU Symp. 297, The Diffuse Interstellar Bands, ed. J. Cami & N. L. J. Cox (Cambridge: Cambridge Univ. Press), 153
- Welty, D. E., & Crowther, P. A. 2010, MNRAS, 404, 1321
- Welty, D. E., Federman, S. R., Gredel, R., Thorburn, J. A., & Lambert, D. L. 2006, ApJS, 165, 138
- Welty, D. E., & Hobbs, L. M. 2001, ApJS, 133, 345
- Welty, D. E., Hobbs, L. M., & Kulkarni, V. P. 1994, ApJ, 436, 152
- Welty, D. E., Hobbs, L. M., & Morton, D. C. 2003, ApJS, 147, 61
- Welty, D. E., Howk, J. C., Lehner, N., & Black, J. H. 2013, MNRAS, 428, 1107
- Welty, D. E., Lauroesch, J. T., Wong, T., & York, D. G. 2016, ApJ, 821, 118
- Welty, D. E., Morton, D. C., & Hobbs, L. M. 1996, ApJS, 106, 533
- Welty, D. E., Ritchey, A. M., Dahlstrom, J. A., & York, D. G. 2014, ApJ, 792, 106
- Welty, D. E., Xue, R., & Wong, T. 2012, ApJ, 745, 173
- Welty, D. E., Hobbs, L. M., Lauroesch, J. T. et al. 1999, ApJS, 124, 465
- Weselak, T., Galazutdinov, G., Beletsky, Y., & Krelowski, J. 2011, AN, 332, 167
- Whittet, D. C. B., Martin, P. G., Fitzpatrick, E. L., & Massa, D. 1993, ApJ, 408, 573
- Wiese, W. L., Fuhr, J. R., & Deters, T. M. 1996, Atomic Transition Probabilities of Carbon, Nitrogen, and Oxygen: A Critical Data Compilation (Washington: NIST)
- York, D. G., & Kinahan, B. F. 1978, ApJ, 228, 127
- Xu, Z., Luo, N., Federman, S. R. et al. 2019, ApJ, 882, 86
- Zonca, A., Cecchi-Pestellini, C., Mulas, G., & Mallocci, G. 2011, MNRAS, 410, 1932

A. Spectra of C I

Figure 24 shows the fits (smooth red lines) to the normalized profiles of the various C I multiplets observed toward HD 62542 (black histograms). At the top is the corresponding higher resolution profile of the Na I $\lambda 5895$ line, which is used to define the component structure for the C I lines. The tick marks show the location of the main component ($v_{\odot} = 14 \text{ km s}^{-1}$) for each line; for C I, the "o" denotes the ground-state transitions, while "**" and "***" denote the transitions from the excited fine-structure states. Unattributed tick marks denote lines from other species (either S I or H₂*). Separate simultaneous fits were performed to the isolated lines from each of the three fine-structure levels, with the relative velocities and b values for most of the components fixed to those determined from Na I; only the individual component column densities, the b value for the main component, and the overall velocity offset were varied for the C I lines. The adopted column densities and main-component b values are given in Table 2.

We used the f values determined by Jenkins & Tripp (2001, 2011) in order to obtain column densities consistent with the values in those surveys, but note that some uncertainties remain.¹³ To set the absolute scale for the f values, Jenkins & Tripp (2001) adopted the well-determined values listed by Wiese et al. (1996) for multiplet 2 (the strongest C I multiplet in $f\lambda$, near 1656 Å). They then estimated the f values for successively weaker transitions by requiring consistency in the measured apparent optical depths, considering the absorption profiles for all the stars in their sample. For the progressively weaker transitions, the derived f values are increasingly higher than the previously reported values – by nearly a factor of 10 for the weakest transitions (Fig. 3 in Jenkins & Tripp 2001). While Jenkins & Tripp (2001, 2011) conducted various tests to try to determine if those differences could be due to the effects of unresolved saturation in the profiles, no satisfactory explanation for the differences has yet emerged. Fortunately, the determination of the relative fine-structure populations (used to estimate the thermal pressures and local densities) should be less affected by the uncertainties in the f values than the absolute column densities.

Contributions from ¹³C were added to the fitted profiles of the C I $\lambda 1328$ multiplet (for which the difference in velocity (relative to the ¹²C lines) is of order -2 km s^{-1} ; Morton 2003; Berengut et al. 2006), but those contributions had only minor effects on the profiles. Given the average interstellar ¹²C/¹³C ratio ~ 70 (Sec. 4.2.2) and the much smaller velocity differences for the other C I multiplets ($\lesssim 0.25 \text{ km s}^{-1}$; Berengut et al. 2006), contributions from ¹³C were not included for the other multiplets.

In general, the C I profiles corresponding to the adopted component structures agree quite well with the observed profiles. The most noticeable differences are for several blended features in the strongest $\lambda 1277$ and $\lambda 1328$ multiplets and for the very weak C I** line in the $\lambda 1276$ multiplet (at 1277.2 Å). Increasing the b values for the excited state lines (from 0.85 to 1.0-1.1 km s^{-1}) would

¹³Three very weak lines were not considered by Jenkins & Tripp (2001, 2011): C I* $\lambda 1287.6$, C I** $\lambda 1274.1$, $\lambda 1288.1$. Revised f values for the first two of those lines are suggested in Sec. C below.

yield noticeably improved fits to the blended features near 1277.5, 1329.1, and 1329.6 Å, but not to the blend of C I λ 1277.2 and C I* λ 1277.3. Increasing the f value of the weak C I** λ 1277.2 line (by a factor of 2.0-2.5) would improve the fit there – and would be more consistent with the differences (new vs. previous) in f values for the other very weak transitions.

B. Spectra of CO

Figures 25 and 26 show the fits (smooth red lines) to the normalized profiles of the various ^{12}CO and ^{13}CO bands observed toward HD 62542 (black histograms). As for the other molecules found in this sight line, absorption from CO is detected only from the main component at $v_{\odot} = 14 \text{ km s}^{-1}$. Both permitted A-X bands and semiforbidden intersystem bands are detected for both isotopologs, from rotational levels $J=0-6$ for ^{12}CO and $J=0-3$ for ^{13}CO ; for each band, the tick marks give the locations of the various rotational lines (from the R, Q, and P branches) at the velocity of the main component. For the permitted A-X CO bands, we adopted the rest wavelengths and f values of Morton & Noreau (1994); for the intersystem bands, we used the values tabulated by Eidelsberg & Rostas (2003), except for ^{12}CO a'17 and ^{13}CO d12 (Morton & Noreau 1994) and ^{12}CO e5 (Sheffer et al. 2002a). The fits to the profiles were performed for a series of choices of the main-component b value, varying only the column densities of the different rotational levels and the overall velocity offset. A b value of 0.5 km s^{-1} gave the most consistent fits to both the strong permitted bands and the weaker intersystem bands; the fits for $b = 0.4$ and 0.6 km s^{-1} were noticeably less consistent. The fits to the individual bands and the adopted column densities $N(J)$, for both ^{12}CO and ^{13}CO , are summarized in Table 13i; the adopted values are given in bold type.

C. Equivalent Widths of Atomic and Molecular Lines

Table 10 lists the total equivalent widths (all components, integrated over the line profile) measured for various atomic species toward HD 62542. Unless otherwise noted (by a number in the reference column), the wavelengths and f values are from Morton (2003; most species) or Jenkins & Tripp (2001, 2011; C I only); the wavelengths are vacuum values for $\lambda < 3000 \text{ Å}$ and in air for $\lambda > 3000 \text{ Å}$. The "Source" column contains a code specifying which spectrum was used for the measurement. The last two columns contain the measured equivalent width and the column density estimated by integrating over the apparent optical depth (AOD) in the profile. In general, the $N(\text{AOD})$ for a given line is larger than the column density that would be estimated just from the equivalent width (assuming the line to be optically thin), but is smaller than the true value (especially for the stronger lines affected by saturation). Where there are multiple lines covering a range in strength for a given species, we have not attempted to obtain a better estimate for the column density by using the method described by Jenkins (1996) – preferring instead to obtain the column densities from the detailed fits to the line profiles – which explicitly account for saturation and blending effects. The uncertainties on the equivalent widths are 1σ values,

and include contributions from both photon noise (Jenkins et al. 1973) and the fits to the local continuum (Sembach & Savage 1992), added in quadrature; the upper limits are 3σ . Because the projected rotational velocity of HD 62542 is fairly low, however, the local "continuum" set by the stellar absorption lines can in some cases be difficult to define precisely (Fig. 1), so that the strengths of some of the broader interstellar lines may be more uncertain.

For a few very weak lines of C I, P I, and S I, f values either were not available or the values listed in Morton (2003) yielded column densities inconsistent with those derived from the profile fits; these are noted by asterisks in the "Ref" column of Table 10. For those lines, we estimate new/revised f values as: C I* λ 1287.6 (0.00023), C I** λ 1274.1 (0.00114), P I λ 1283.9 (0.14), P I λ 1286.4 (0.14), P I λ 1377.9 (0.04), S I λ 1381.6 (0.00018), S I λ 1388.4 (0.00034).

Table 11 lists the equivalent widths (main component only) measured for various molecular species toward HD 62542. The references for the wavelengths and f values are given at the end of the table; the sources of the spectra are specified as in Table 10. The last two columns contain the measured equivalent width and the AOD column density estimate for each line; the uncertainties and upper limits are 1σ and 3σ , respectively. We note that the $N(\text{AOD})$ refer to the lower level involved in each transition; total molecular column densities (as given in Table 4) cannot be estimated unless sufficient information on the excitation is available. Values for the unidentified line near 1300 Å and for several of the DIBs are included at the end of the table.

Table 12 lists the equivalent widths (main component only) measured for individual rotational lines in four of the C₂ bands detected toward HD 62542. The wavelengths and band f values are those adopted by Sonnentrucker et al. (2007); the sources of the spectra are specified as in Table 10. The last column gives the column densities for each rotational level, as determined via simultaneous fits to all the lines in each band, using the adopted $b = 0.7 \text{ km s}^{-1}$. The AOD column density estimates (next-to-last column) are generally in good agreement with the values obtained from the profile fits for the optical/NIR A-X bands, but not for the lower J levels in the D-X (0,0) band, where the stronger UV lines are affected by saturation.

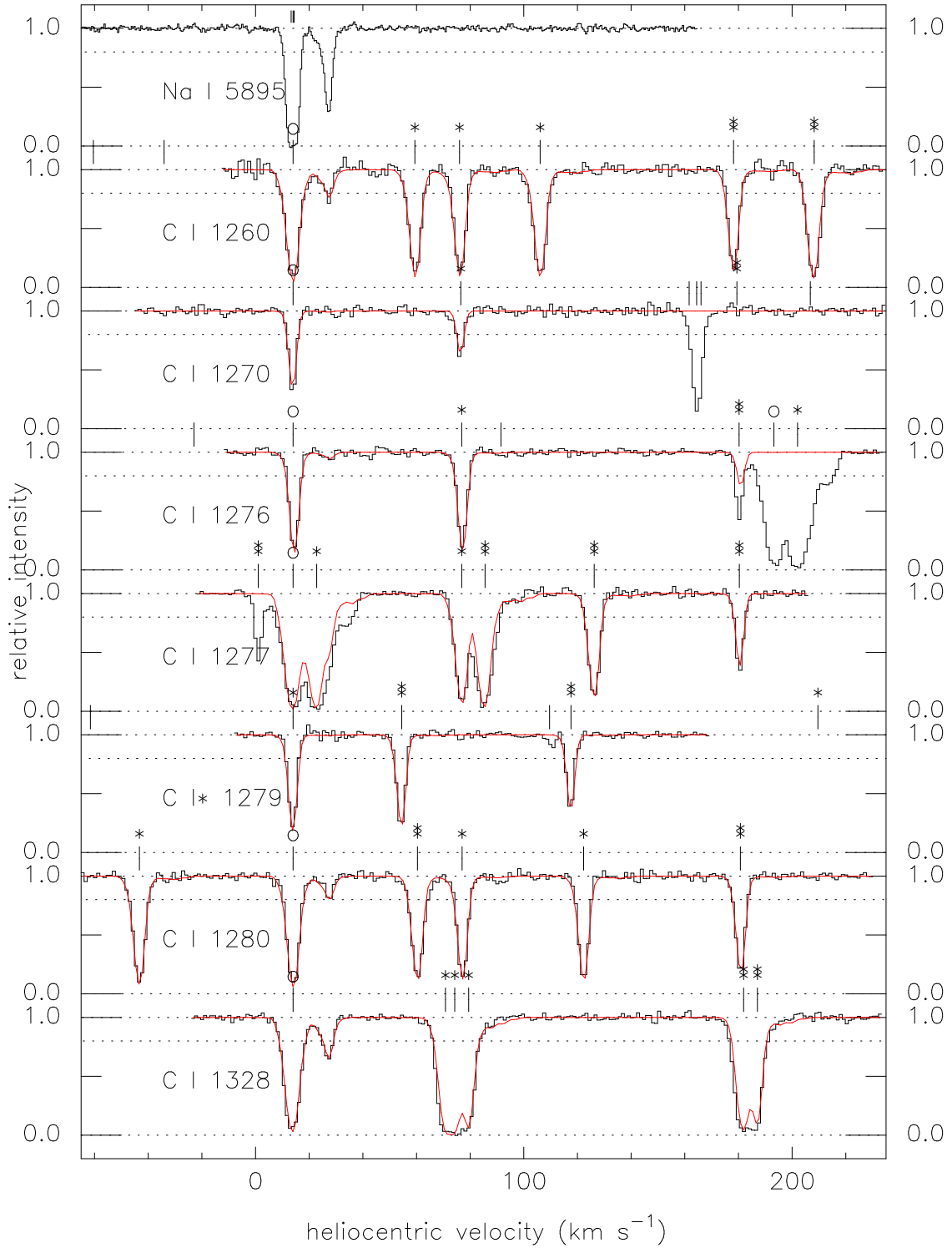


Fig. 24.— Normalized spectra of C I absorption multiplets toward HD 62542 (black histograms). The smooth red curves show the theoretical profiles based on the component structures derived from simultaneous fits to the unblended lines of each of the three fine-structure states. At the top is the corresponding higher resolution spectrum of the Na I D1 line. Tick marks above the Na I D1 line denote the detailed component structure (used also to fit the C I lines); tick marks above the C I lines denote the locations of the main component (14 km s^{-1}) for the ground (o) and excited fine-structure states (* and **); unmarked ticks denote lines of other species (S I or H_2^*).

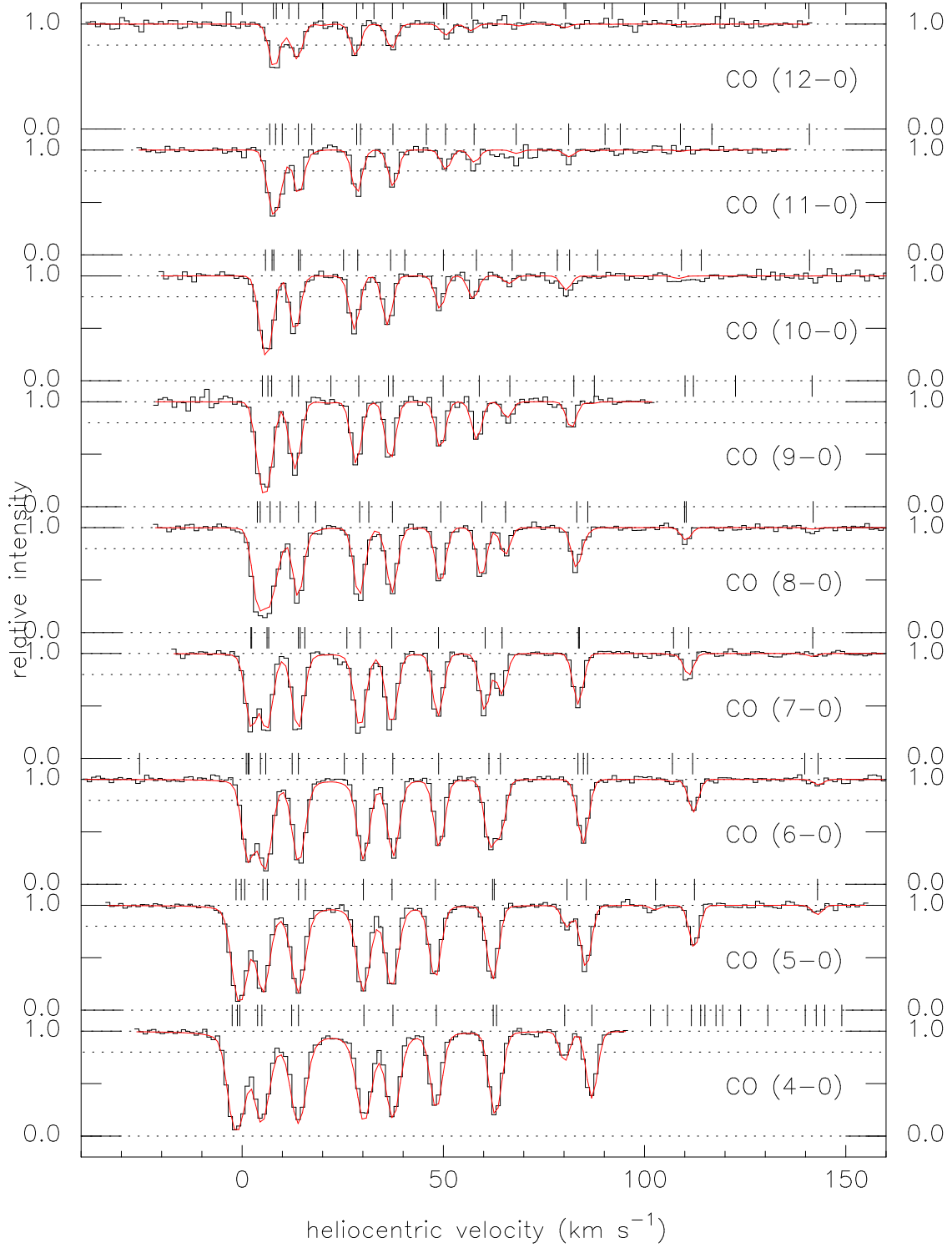


Fig. 25.— Normalized spectra of ^{12}CO A-X bands toward HD 62542 (black histograms). The smooth red curves show the theoretical profiles based on the component structure adopted from fits to the ensemble of bands (a single component at 14 km s^{-1} , with $b = 0.5 \text{ km s}^{-1}$). Tick marks above the spectra denote the locations of that component for the individual rotational levels ($J = 0-6$) from the R, Q, and P branches.

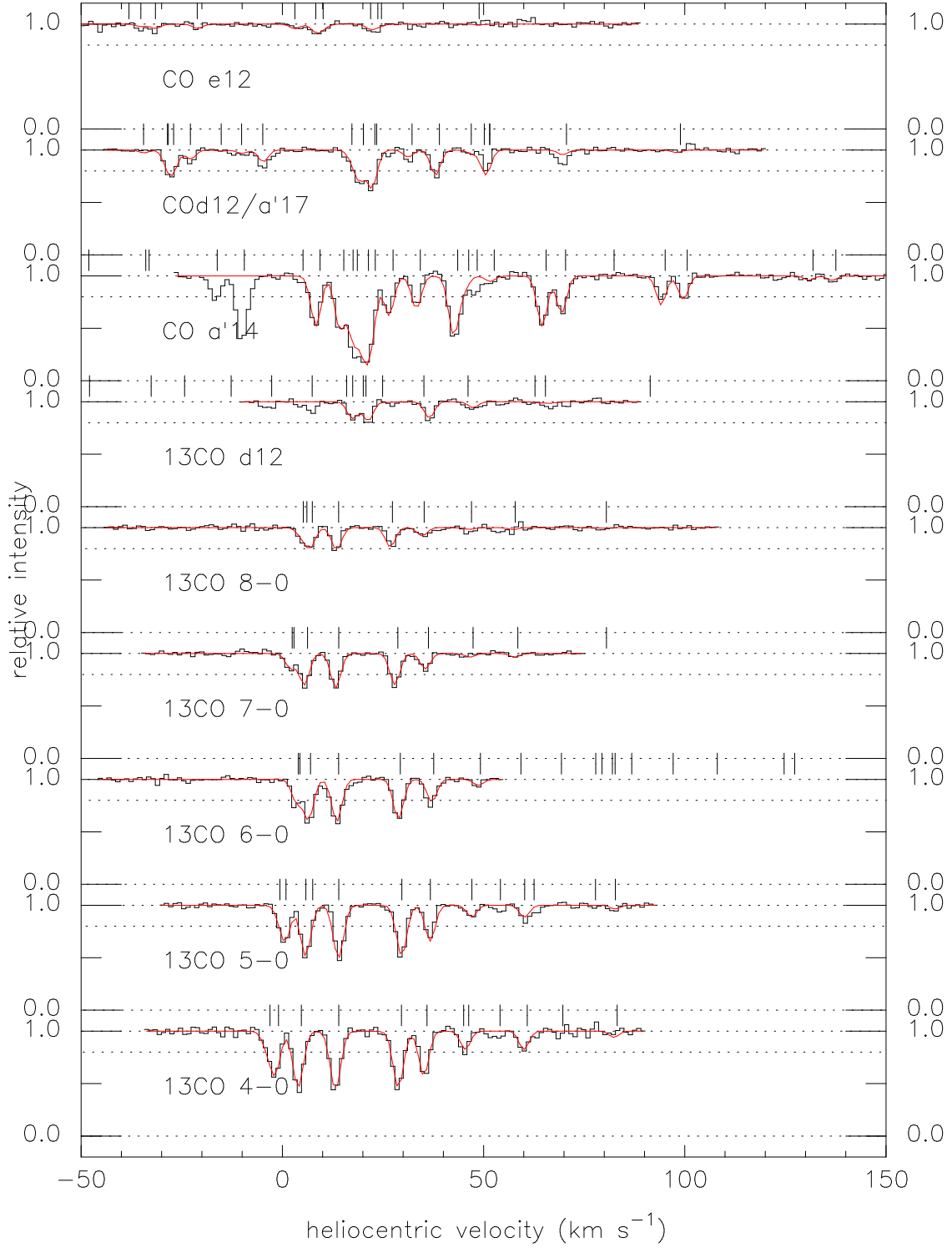


Fig. 26.— Spectra of ^{13}CO A-X and selected ^{12}CO intersystem bands toward HD 62542 (black histograms). The smooth red curves show the theoretical profiles based on the component structure adopted from fits to the ensemble of bands (a single component at 14 km s^{-1} , with $b = 0.5 \text{ km s}^{-1}$). Tick marks above the spectra denote the locations of that component for the individual rotational levels ($J = 0-3$) from the R, Q, and P branches. Absorption that is marked, but not fitted, is due to lines of CO, C^{18}O , or H_2^* .

Table 10. Equivalent Widths – Atomic Lines

Species	λ	f	Ref ^a	Source ^b	W_λ	$\log[N(\text{AOD})]$	$\log[N(\text{fit})]$
B II	1362.4600	0.99600		s	<1.8	<11.04	...
	1362.4730	0.99600		s	blend	...	
C I	1260.7351	0.05880	1	s	25.6±1.2	13.75±0.01	14.92±0.04
	1270.1430	0.00216	1	s	10.1±0.5	14.67±0.02	
	1276.4822	0.01180	1	s	14.9±0.4	14.16±0.01	
	1277.2452	0.13140	1	s	blend	...	
	1280.1352	0.04806	1	s	22.8±0.7	13.79±0.01	
C I*	1328.8333	0.08985	1	s	31.2±0.5	13.68±0.01	
	1260.9262	0.02608	1	s	20.1±0.6	13.98±0.01	15.11±0.03
	1260.9961	0.02204	1	s	18.4±0.5	14.01±0.01	
	1261.1224	0.02731	1	s	22.4±0.7	14.01±0.01	
	1270.4081	0.00041	1	s	6.4±0.6	15.10±0.03	
	1276.7498	0.00824	1	s	14.3±0.4	14.28±0.01	
	1277.2827	0.08142	1	s	blend	...	
	1277.5131	0.03950	1	s	blend	...	
	1279.0562	0.00610	1	s	12.4±0.5	14.34±0.01	
	1279.8907	0.02817	1	s	21.0±0.5	13.98±0.10	
	1280.4043	0.01320	1	s	17.6±0.5	14.19±0.01	
	1280.5975	0.01777	1	s	16.7±0.4	14.06±0.01	
	1287.6076	[0.00023]	*	s	4.4±0.4	[15.11]	
	1329.0849	0.03601	1	s	blend	...	
	1329.1004	0.04350	1	s	blend	...	
1329.1233	0.03086	1	s	blend	...		
C I**	1261.4255	0.02071	1	s	16.5±0.7	13.98±0.01	14.71±0.03
	1261.5519	0.04417	1	s	22.7±0.8	13.83±0.01	
	1274.1090	[0.00114]	*	s	8.4±0.3	[14.71]	
	1277.1900	0.00075	1	s	7.4±0.2	14.95±0.01	
	1277.5501	0.08622	1	s	blend	...	
	1277.7233	0.02764	1	s	18.8±0.5	13.92±0.01	
	1277.9539	0.00307	1	s	10.4±0.4	14.51±0.01	
	1279.2290	0.00900	1	s	12.8±0.4	14.19±0.01	
	1279.4980	0.00362	1	s	9.5±0.3	14.39±0.01	
	1280.3331	0.02759	1	s	21.2±0.6	13.94±0.01	
	1280.8471	0.01329	1	s	15.0±0.5	14.09±0.01	
	1288.0553	0.00002		s	<1.4	[<15.68]	
	1329.5775	0.05785	1	s	blend	...	
	1329.6004	0.03064	1	s	blend	...	
	C II	1334.5323	0.12800		s	stellar	...
2325.4029		4.78E-08		s	<2.7	<18.08	
C II*	1335.6627	0.01280		s	stellar
	1335.7077	0.11500		s	stellar
N I	1200.2233	0.08690		s	141.9±4.7	>14.60	...
	1200.7098	0.04320		s	142.6±6.0	>15.02	
O I	1355.5977	1.16E-06		s	6.8±0.3	17.65±0.02	[17.82]
O I*	1304.8576	0.04780		s	11.2±0.6	13.32±0.02	[13.65]
O I**	1306.0286	0.04780		s	7.9±0.6	13.16±0.02	[13.37]

Table 10—Continued

Species	λ	f	Ref ^a	Source ^b	W_λ	$\log[N(\text{AOD})]$	$\log[N(\text{fit})]$
Na I	3302.3690	0.00897		u	31.3±1.1	13.65±0.01	14.05±0.08
				U	30.1±0.3	13.63±0.01	
	3302.9780	0.00448		u	22.1±1.0	13.78±0.01	
				U	25.4±0.3	13.84±0.01	
	5889.9510	0.65500		c	225.9±2.4	>12.49	
				u	222.4±1.3	>12.25	
				U	230.0±1.5	>12.24	
	5895.9242	0.32700		c	184.3±2.3	>12.70	
u				164.5±1.3	>12.41		
U				182.6±1.4	>12.42		
Mg I	1827.9351	0.02420		s	15.8±0.9	13.51±0.02	13.84±0.04
	2026.4768	0.11300		s	29.4±0.7	13.11±0.01	
Mg II	1239.9253	0.00063		s	13.9±1.5	15.25±0.04	15.25±0.05
	1240.3947	0.00036		s	6.4±1.4	15.15±0.08	
Al I	2367.7750	0.10600		s	<1.8	<11.54	...
	3944.0060	0.11700		u	<1.2	<10.86	
				U	<0.7	<10.62	
Al III	1854.7184	0.55900		s	40.1±6.5	12.47±0.06	12.45±0.05
	1862.7910	0.27800		s	19.1±6.7	12.41±0.13	
Si I	1845.5202	0.27000		s	3.1±1.0	11.61±0.10	[11.61]
	2208.6666	0.05750		s	1.0±0.4	11.61±0.10	
Si II	1260.4221	1.18000		s	stellar	...	15.39±0.02
	1304.3702	0.08630		s	173.0±1.3	>14.75	
	1808.0129	0.00208		s	92.6±4.0	15.37±0.02	
	2335.1230	4.25E-06		s	<3.6	<16.25	
Si II*	1264.7377	1.05000		s	stellar
	1265.0020	0.11700		s	stellar	...	
Si III	1206.5000	1.63000		s	stellar
Si IV	1393.7602	0.51300		s	45.1±2.6	12.80±0.03	12.83±0.03
	1402.7729	0.25400		s	29.1±3.4	12.86±0.05	
P I	1283.8810	[0.14]	*	s	2.2±0.5	[12.02]	[12.02]
	1286.4440	[0.14]	*	s	2.2±0.5	[12.02]	
	1377.0730	0.11000		s	0.8±0.3	11.66±0.12	
	1377.9343	[0.04]	*	s	0.7±0.2	[12.02]	
	1379.4282	0.21900		s	3.2±0.4	11.96±0.04	
	1381.4760	0.31600		s	4.1±0.5	11.93±0.04	
	1782.8291	0.11300		s	2.2±0.7	11.87±0.09	
	1787.6481	0.06040		s	3.0±1.0	12.27±0.10	
P II	1301.8743	0.01270		s	13.8±1.2	13.94±0.03	14.03±0.03
S I	1241.9050	0.00164		s	5.3±0.6	14.47±0.03	14.65±0.02
	1247.1342	0.00064		s	2.1±0.4	14.41±0.05	
	1247.1602	0.00430		s	6.2±0.1	14.11±0.04	
	1262.8599	0.00205		s	8.0±0.5	14.56±0.02	
	1270.7686	0.00011		s	blend	...	
	1270.7804	0.00837		s	16.9±0.7	14.37±0.01	
	1270.7874	0.00158		s	blend	...	

Table 10—Continued

Species	λ	f	Ref ^a	Source ^b	W_λ	$\log[N(\text{AOD})]$	$\log[N(\text{fit})]$
	1295.6531	0.08700		s	20.2±0.5	13.44±0.01	
	1296.1739	0.02200		s	14.9±0.4	13.88±0.01	
	1303.4300	0.00436		s	9.5±0.7	14.31±0.02	
	1316.5425	0.02790		s	15.2±0.4	13.78±0.01	
	1316.6150	0.00530		s	14.6±0.4	14.44±0.01	
	1316.6219	0.00036		s	blend	...	
	1381.5527	[0.00018]	*	s	1.4±0.3	[14.65]	
	1388.4358	[0.00034]	*	s	2.6±0.2	[14.65]	
	1401.5142	0.01280		s	14.5±0.4	14.03±0.01	
	1425.0300	0.12500		s	24.2±0.4	13.33±0.01	
	1425.1879	0.02230		s	17.4±0.3	13.85±0.01	
	1425.2191	0.00148		s	10.4±0.4	14.72±0.01	
	1807.3113	0.09050		s	32.0±1.3	13.39±0.01	
S II	1250.5780	0.00543		s	105.7±1.2	>15.62	...
	1253.8050	0.01090		s	125.3±1.4	>15.42	
	1259.5180	0.01660		s	140.6±1.3	>15.37	
Cl I	1335.7258	0.03130		s	blend	...	[14.30]
	1347.2396	0.15300		s	15.9±0.3	>13.03	
	1379.5279	0.00275		s	7.6±0.5	14.32±0.02	
	1389.6920	0.00013		s	0.7±0.3	14.53±0.14	
K I	4044.1422	0.00568		u	<2.0	<12.39	12.09±0.07
				U	1.0±0.2	12.07±0.09	
				h	0.5±0.1	11.77±0.08	
	4047.2132	0.00264		U	0.3±0.1	11.89±0.13	
				h	0.3±0.1	11.93±0.09	
	7698.9740	0.33930		U	70.8±0.7	>11.69	
				m	67.7±0.2	>11.63	
				a	88.0±3.8	>11.75	
Ca I	4226.7280	1.77000		u	<1.7	<9.78	[9.12]
				U	<0.4	<9.19	
				h	0.4±0.1	9.10±0.09	
Ca II	3933.6614	0.62670		c	68.1±2.0	11.96±0.01	11.97±0.02
				u	68.2±2.0	11.96±0.01	
Ti I	3635.4620	0.25200		u	<2.6	<10.95	...
				U	<0.3	<10.03	
Ti II	3241.9829	0.23200		U	7.0±0.5	11.51±0.03	11.56±0.03
	3383.7588	0.35800		u	10.7±1.7	11.48±0.06	
				U	12.8±0.4	11.56±0.02	
V II	2138.8270	0.08200		s	<3.3	<12.00	...
Cr I	3578.6840	0.36600		u	<2.4	<10.76	...
				U	<0.3	<9.68	
	4254.3320	0.10990	2	h	<0.4	<10.37	
Mn I	4030.7530	0.05650		h	<0.4	<10.67	...
Mn II	1201.1180	0.12100		s	<10.7	<12.84	...
Fe I	2167.4534	0.15000		s	1.2±0.5	11.28±0.15	[11.30]
	3440.6057	0.02360		U	1.0±0.2	11.59±0.07	

Table 10—Continued

Species	λ	f	Ref ^a	Source ^b	W_λ	$\log[N(\text{AOD})]$	$\log[N(\text{fit})]$
	3719.9347	0.04110		u	1.2±0.5	11.36±0.14	
				U	1.1±0.1	11.33±0.04	
	3859.9114	0.02170		u	1.3±0.4	11.68±0.09	
				U	0.7±0.1	11.41±0.08	
Fe II	1260.5330	0.02400		s	blend	...	14.48±0.02
	1901.7730	0.00007		s	<4.4	<15.29	
	2234.4472	0.00003	3	s	<2.7	<15.38	
	2249.8768	0.00182		s	14.0±1.5	14.26±0.04	
	2260.7805	0.00244		s	26.5±1.4	14.42±0.02	
	2344.2139	0.11400		s	251.6±1.9	>14.25	
	2367.5905	0.00002	4	s	<2.7	<15.41	
	2374.4612	0.03130		s	171.2±1.3	14.41±0.01	
Fe II*	2338.7248	0.08970		s	<1.4	<11.50	...
	2345.0011	0.15300		s	<1.7	<11.35	
	2349.0223	0.08980		s	<1.7	<11.58	
	2389.3582	0.08250		s	<1.3	<11.51	
Co II	2012.1664	0.03680		s	<5.5	<12.60	...
Ni I	2320.7468	0.68500		s	<2.1	<10.80	...
Ni II	1317.2170	0.05710	5	s	10.3±0.9	13.09±0.03	13.26±0.04
	1370.1320	0.05880	5	s	16.2±1.0	13.26±0.03	
Ni II*	2217.1670	0.30000	6	s	<1.9	<11.16	...
Cu II	1358.7730	0.26300		s	2.9±0.9	11.84±0.14	11.90±0.04
Zn I	2139.2477	1.47000		s	18.6±0.7	11.67±0.01	[12.14]
Zn II	2026.1370	0.50100		s	89.0±2.3	>12.93	13.13±0.05
Ga II	1414.4020	1.77000		s	2.5±1.0	10.91±0.15	10.92±0.07
Ge II	1237.0591	1.23200	7	s	7.0±1.8	11.72±0.11	11.94±0.06
As II	1263.7700	0.25900	8	s	<1.6	<11.64	...
Kr I	1235.8380	0.20400	8	s	5.6±1.5	12.36±0.11	12.41±0.05
Cd II	2145.0697	0.51000	8	s	2.8±1.8	11.14±0.14	11.18±0.06
Sn II	1400.4400	1.03000	8	s	1.4±0.6	10.91±0.15	10.89±0.08
Pb II	1433.9050	0.32100	9	s	<2.0	<11.54	...

Note. — Uncertainties are 1- σ ; limits are 3- σ . AOD column densities are lower limits to the true values when derived from stronger lines. Values in square braces are assumed, in order to estimate new f values.

^aTransition f values are from Morton (2003), unless specified otherwise: 1 = Jenkins & Tripp (2001, 2011; C only); 2 = Morton 1991; 3 = Miller et al. 2007; 4 = Welty et al. 1999; 5 = Jenkins & Tripp 2006; 6 = Gnaciński 2009; 7 = Heidarian et al. 2017; 8 = Morton 2000; 9 = Heidarian et al. 2015; * = estimated in this study (see Sec. C)

^bSources for the spectra are: a = AAT/UCLES, c = ESO/CES, h = Keck/HIRES, m = Magellan/MIKE, s = *HST*/STIS, u/U = ESO/UVES.

Table 11. Equivalent Widths – Molecular Lines

Species	Band	Transition	λ	f	Ref ^a	Source ^b	W_λ	$\log[N(\text{AOD})]$	
H ₂	B-X(0,3)	R0	1274.537	0.09118	1	s	0.9±0.3	11.84±0.15	
		R1	1274.922	0.06035	1	s	1.0±0.6	12.06±0.27	
		P1	1276.812	0.03058	1	s	0.6±0.3	12.15±0.25	
		R2	1276.325	0.05385	1	s	1.7±0.3	12.34±0.08	
		P2	1279.464	0.03674	1	s	1.4±0.3	12.41±0.11	
		R3	1278.734	0.05074	1	s	<1.3	<12.25	
		P3	1283.111	0.03935	1	s	<1.4	<12.37	
		R4	1282.141	0.04868	1	s	blend	...	
		P4	1287.732	0.04072	1	s	<1.4	<12.37	
	B-X(0,4)	R0	1333.475	0.12500	1	s	1.1±0.3	11.74±0.13	
		R1	1333.797	0.08352	1	s	1.6±0.4	12.08±0.10	
		P1	1335.868	0.04150	1	s	blend	...	
		R2	1335.131	0.07531	1	s	1.6±0.8	12.12±0.24	
		P2	1338.568	0.04972	1	s	0.9±0.2	12.06±0.12	
		R3	1337.467	0.07190	1	s	0.8±0.3	11.85±0.15	
		P3	1342.256	0.05322	1	s	blend	...	
		R4	1340.791	0.07000	1	s	0.6±0.3	11.72±0.20	
		P4	1346.908	0.05518	1	s	0.6±0.4	11.82±0.30	
	CH	G-X		1368.74	0.019	2	s	3.3±0.3	13.05±0.03
			1369.13	0.030	2	s	3.8±0.4	12.90±0.06	
			1370.87	0.009	2	s	1.5±0.3	13.03±0.10	
C-X(0,0)			3137.559	0.0021	3	U	2.6±0.2	13.15±0.04	
			3143.160	0.0064	3	U	8.3±0.4	13.19±0.02	
			3145.992	0.0043	3	U	5.8±0.2	13.20±0.02	
B-X(1,0)		Q ₂ (1)+ ^Q R ₁₂ (1)		3633.289	0.00104	4	u	1.5±0.6	13.09±0.18
							U	2.0±0.2	13.21±0.04
			^P Q ₁₂ (1)	3636.222	0.00069	4	u	1.2±0.5	13.17±0.19
B-X(0,0)		R ₂ (1)		3878.774	0.0011	5	u	2.0±0.6	13.14±0.06
							U	2.8±0.2	13.28±0.03
				3886.409	0.0032	5	u	7.2±0.7	13.23±0.03
							U	7.0±0.3	13.22±0.02
			^P Q ₁₂ (1)	3890.217	0.0022	5	u	4.9±0.6	13.24±0.03
A-X(0,0)		R _{2e} (1)+R _{2f} (1)		4300.3132	0.00506	6	u	23.2±0.8	13.50±0.01
						U	22.1±0.3	13.47±0.01	
						h	22.0±0.1	>13.47	
						u	<1.7	<12.29	
						h	0.4±0.1	11.68±0.07	
CH ⁺	A-X(0,0)	R0	4232.548	0.00545	7	u	<0.9	<13.01	
CH ₂	D-X		1396.8	0.0050	8	s	<0.9	<13.01	
	B-X(1,0)	R1	4711.400	...		U	<0.4	...	
C ₂ ⁺	B-X(0,0)	R1	5065.200	...		U	<0.4	...	
	B-X(1,0)	R0	4894.200	...		U	<0.4	...	
C ₂ ⁻	B-X(1,0)	R0	4894.200	...		U	<0.4	...	
	B-X(1,0)	R1	3579.453	0.00196	9	u	2.0±0.8	12.97±0.13	
CN	B-X(1,0)	R1	3579.453	0.00196	9	U	2.1±0.1	12.99±0.03	

Table 11—Continued

Species	Band	Transition	λ	f	Ref ^a	Source ^b	W_λ	$\log[N(\text{AOD})]$
		R0	3579.963	0.00294	9	u	6.8±0.9	13.33±0.04
		P1	3580.940	0.00098	9	u	<2.4	<13.32
	B-X(0,0)	R2	3873.370	0.0203	10	u	0.7±0.1	12.78±0.07
						U	1.2±0.2	11.63±0.07
		R ₁ (1)+R ₂ (1)+ ^R Q ₂₁ (1)	3873.999	0.0225	10	u	19.0±0.7	12.85±0.01
						U	18.7±0.3	12.84±0.01
		R ₁ (0)+ ^R Q ₂₁ (0)	3874.607	0.0337	10	u	27.9±0.7	12.87±0.01
						U	27.7±0.2	12.86±0.01
		P ₁ (1)+ ^P Q ₁₂ (1)	3875.764	0.0112	10	u	11.7±0.8	12.92±0.02
						U	11.5±0.2	12.91±0.01
		P2	3876.312	0.0135	10	U	0.6±0.2	11.55±0.11
	A-X(2,0)	^R Q ₂₁ (0)	7874.847	2.54e-4	11	U	3.4±0.3	13.39±0.04
		R ₁ (1)	7903.896	2.54e-4	11	U	1.4±0.2	13.00±0.08
						m	1.5±0.6	13.04±0.17
		R ₁ (0)	7906.601	4.01e-4	11	U	4.7±0.3	13.33±0.03
						m	6.0±0.5	13.43±0.03
		^Q R ₁₂ (1)+Q ₁ (1)	7908.955	2.33e-4	11	U	1.7±0.3	13.11±0.08
¹³ CN	B-X(0,0)	R ₁ (1)+R ₂ (1)+ ^R Q ₂₁ (1)	3874.176	0.0225	10	U	1.0±0.2	11.52±0.09
		R ₁ (0)+ ^R Q ₂₁ (0)	3874.783	0.0337	10	U	1.7±0.2	11.59±0.04
						m	1.3±0.2	11.47±0.06
CN ⁺	f-a		2181.78	...		s	<1.7	...
CO ⁺	A-X(2,0)		4250.94	0.00064	12	u	<1.4	<13.15
						h	<0.4	<12.59
CS	C-X(0,0)		1400.88	0.45	13	s	9.3±0.6	12.12±0.03
NH	A-X(0,0)	Q0	3353.9253	0.0024	14	u	1.7±0.7	12.87±0.13
						U	1.8±0.2	12.87±0.05
		R0	3358.0525	0.0041	14	u	3.1±0.8	12.89±0.08
						U	3.3±0.2	12.91±0.03
N ₂	a-X(6,0)	R0	1273.30	...		s	<1.1	...
NO	A-X(0,0)		2262.98	0.00052	15	s	<1.6	<13.86
NO ⁺	A-X(2,0)	R0	1312.94	0.0017	15	s	<0.9	<13.54
OH	D-X(0,0)	Q ₁ (3/2)+ ^Q P ₂₁ (3/2)	1222.07	0.0115	16	s	5.0±2.2	13.58±0.13
		P ₁ (3/2)	1222.52	0.0071	16	s	5.2±2.2	13.81±0.12
	A-X(0,0)	Q ₁ (3/2)	3078.4398	6.20e-4	17	U	4.6±0.4	13.73±0.04
		^Q P ₂₁ (3/2)	3078.4720	4.31e-4	17	U	blend	
		P ₁ (3/2)	3081.6644	6.48e-4	17	U	3.0±0.4	13.75±0.06
OH ⁺	A-X(1,0)	R0	3346.9556	3.52e-4	18	U	<0.47	<13.13
	A-X(0,0)	Q0	3572.6519	3.12e-4	18	U	<0.52	<13.17
		R0	3583.7557	5.27e-4	18	u	<2.1	<13.54
						U	<0.39	<12.81
H ₂ O	C-X		1239.382	0.0043	19	s	<2.2	<13.58
			1239.728	0.0180	19	s	<2.2	<12.95
			1240.153	0.0057	19	s	<2.2	<13.43
SiO	J-X		1310.01	...		s	<1.6	...

Table 11—Continued

Species	Band	Transition	λ	f	Ref ^a	Source ^b	W_λ	$\log[N(\text{AOD})]$
SH	G-X(0,0)		1257.34	...		s	<1.8	...
SH ⁺	A-X(0,0)	R0	3363.49	0.00062	20	u	<2.4	<13.59
						U	<0.9	<13.14
HCl	C-X(0,0)	R0	1290.257	0.141	21	s	<1.4	<11.83
AlH	C-X(0,0)	R0	2242.295	...		s	<1.8	...
UID			1300.45	...		s	3.8±0.4	...
DIBs			4963.9	...		o	6±1	...
			5780.6	...		o	27±3	...
			5797.2	...		o	12±1	...
			6196.0	...		o	4±1	...
			6203.7	...		o	15±4	...
			6283.8	...		o	50±20	...
			6613.7	...		o	7±1	...

Note. — Uncertainties are 1σ ; limits are 3σ .

^aReferences for f values are: 1 = Abgrall et al. 1994; 2 = Sheffer & Federman 2007; 3 = S. R. Federman 2012, private communication; 4 = Weselak et al. 2011; 5 = Lien 1984; 6 = Larsson & Siegbahn 1983a; 7 = Larsson & Siegbahn 1983b; 8 = Lyu et al. 2001; 9 = Meyer & Roth 1990; 10 = Brooke et al. 2014; 11 = Gredel et al. 1991; 12 = Herbig 1968; 13 = Xu et al. 2019; 14 = Meyer & Roth 1991; 15 Jenkins et al. 1973; 16 = Roueff 1996; 17 = Felenbok & Roueff 1996; 18 = Hodges et al. 2018; 19 = Smith & Parkinson 1978; 20 = Pineau des Forêts et al. 1986; 21 = Federman et al. 1995

^bSources of the spectra are: h = Keck/HIRES, m = Magellan/MIKE, o = combination of available optical spectra; s = *HST*/STIS, u/U = ESO/UVES.

Table 12. Equivalent Widths – C₂

Band	Transition	λ	f	Source	W_λ	$N_{12}(\text{AOD})$	$N_{12}(\text{fit})$
D-X(0,0)	R0	2313.163	0.0545	s	9.7±0.5	4.6±0.2	6.9±0.5
	R2	2312.769		s	15.7±0.6	13.6±0.3	25.8±1.4
	P2	2313.745		s	11.0±0.7	13.5±0.5	
	R4	2312.371		s	12.9±0.5	12.0±0.3	25.7±1.4
	P4	2314.126		s	12.8±0.6	14.4±0.4	
	R6	2311.967		s	10.8±0.5	9.9±0.3	16.3±0.8
	P6	2314.503		s	9.9±0.3	10.2±0.2	
	R8	2311.560		s	8.4±0.5	7.2±0.3	8.5±0.4
	P8	2314.874		s	6.7±0.4	6.3±0.2	
	R10	2311.147		s	4.5±0.4	3.7±0.2	4.8±0.3
	P10	2315.240		s	4.9±0.4	4.4±0.3	
	R12	2310.730		s	3.2±0.4	2.5±0.2	2.9±0.3
	P12	2315.601		s	2.9±0.6	2.5±0.2	
	R14	2310.309		s	2.5±0.5	1.9±0.3	2.0±0.2
	P14	2315.956		s	2.6±0.5	2.2±0.3	
	R16	2309.884		s	1.1±0.4	0.8±0.2	1.0±0.2
	P16	2316.307		s	1.4±0.5	1.2±0.3	
	R18	2309.455		s	1.7±0.4	1.3±0.2	1.0±0.2
P18	2316.652	s	1.3±0.4	1.1±0.2			
A-X(3,0)	R0	7719.329	0.00065	U	2.6±0.2	7.6±0.7	7.7±0.7
	R2	7716.528		U	telblend		28.8±1.6
	Q2	7722.095		U	4.5±0.3	26.8±1.8	
	P2	7725.819		U	1.2±0.2	36.4±5.7	
	R4	7714.944		U	2.8±0.3	24.4±2.3	25.8±1.3
	Q4	7724.219		U	3.8±0.2	22.5±1.2	
	P4	7731.663		U	2.2±0.3	38.6±5.1	
	R6	7714.575		U	1.9±0.3	18.1±2.6	16.3±1.3
	Q6	7727.557		U	2.6±0.3	15.4±1.5	
	R8	7715.415		U	telblend		7.2±1.4
Q8	7732.117	U	1.1±0.2	6.6±1.3			
A-X(2,0)	R0	8757.686	0.00140	m	6.1±0.6	6.5±0.6	
				U	5.9±0.3	6.3±0.4	7.1±0.3
	R2	8753.949		m	8.3±0.5	22.0±1.0	
				U	7.8±0.2	20.9±0.5	24.2±0.5
	Q2	8761.194		m	12.5±0.3	27.0±1.0	
				U	9.9±0.3	21.4±0.7	
	P2	8766.031		m	2.8±0.4	29.0±4.0	
				U	2.4±0.3	25.8±2.9	
	R4	8751.685		U	6.5±0.4	20.7±1.1	21.7±0.5
	Q4	8763.751		m	9.0±0.4	19.0±1.0	
				U	9.1±0.3	19.6±0.5	
	P4	8773.430		U	[2.7±0.3]	[16.8±1.7]	
R6	8750.848	U	3.9±0.2	13.4±0.7	13.0±0.5		
Q6	8767.759	m	5.3±0.5	11.0±1.0			

Table 12—Continued

Band	Transition	λ	f	Source	W_λ	$N_{12}(\text{AOD})$	$N_{12}(\text{fit})$
				U	4.9 ± 0.3	10.5 ± 0.5	
	R8	8751.486		U	$[1.6 \pm 0.4]$	$[5.8 \pm 1.1]$	6.5 ± 0.4
	Q8	8773.221		U	3.3 ± 0.3	7.0 ± 0.7	
A-X(1,0)	R0	10143.723	0.00231	U	8.0 ± 0.7	3.9 ± 0.3	4.2 ± 0.3
	R2	10138.540		U	12.3 ± 0.8	15.0 ± 1.0	15.1 ± 0.5
	Q2	10148.351		U	12.5 ± 0.5	12.2 ± 0.5	
	P2	10154.897		U	3.4 ± 0.4	16.3 ± 1.9	
	R4	10135.149		U	12.1 ± 0.8	17.6 ± 1.2	16.4 ± 0.5
	Q4	10151.523		U	15.7 ± 0.5	15.3 ± 0.5	
	P4	10164.763		U	6.7 ± 0.6	19.1 ± 1.7	
	R6	10133.603		U	5.8 ± 0.5	9.0 ± 0.9	8.7 ± 0.5
	Q6	10156.515		U	7.9 ± 0.5	7.6 ± 0.4	
	R8	10133.854		U	5.9 ± 0.8	5.9 ± 0.8	6.1 ± 0.5
	Q8	10163.323		U	6.0 ± 0.7	5.8 ± 0.6	
	Q10	10171.963		U	3.2 ± 0.6	3.0 ± 0.6	3.5 ± 0.5

Note. — Sources are m = Magellan/MIKE, s = *HST*/STIS, U = ESO VLT/UVES. Column densities are in units of 10^{12} cm^{-2} .

Table 13. Fits to CO Bands

Species	Band	λ	$\log(f\lambda)$	Ref ^a	$N_{15}(0)$	$N_{15}(1)$	$N_{15}(2)$	$N_{15}(3)$	$N_{14}(4)$	$N_{13}(5)$	$N_{12}(6)$	$N_{15}(\text{tot})$
¹² CO	(12,0)	1246.059	-0.950	1	5.2±0.7	10.5±1.2	7.8±0.9	3.5±0.5	[4.0]	[3.0]	[4.0]	27.4±1.7
	(11,0)	1263.433	-0.643	1	4.5±0.7	11.0±1.5	7.2±0.8	2.9±0.4	(8.5±2.4)	[3.0]	[4.0]	26.5±1.9
	(10,0)	1281.866	-0.279	1	7.0±1.7	11.9±2.4	6.0±0.6	2.5±0.3	4.8±1.3	[3.0]	[4.0]	27.9±3.0
	(9,0)	1301.403	0.092	1	7.1±2.6	10.0±2.7	5.8±0.8	2.1±0.3	4.7±0.8	<4.6	[4.0]	25.5±3.8
	(8,0)	1322.150	0.423	1	(10.2±1.8)	(18.7±2.6)	8.7±1.0	2.4±0.2	3.3±0.3	5.2±1.6	[4.0]	40.4±3.3
	(7,0)	1344.186	0.745	1	5.6±1.0	14.1±2.0	7.4±0.9	2.3±0.3	3.7±0.4	1.8±2.5	(4.0±8.1)	29.8±2.4
	(6,0)	1367.623	1.036	1	5.2±0.8	7.3±0.9	5.9±0.6	1.9±0.5	3.0±0.2	2.7±0.7	8.6±3.4	20.6±1.4
	(5,0)	1392.525	1.305	1	(2.7±0.4)	(5.8±0.6)	(3.7±0.5)	2.7±0.5	2.6±0.2	3.1±0.3	7.5±0.2	15.2±1.0
	(4,0)	1419.044	1.520	1	(2.4±0.3)	(4.0±0.4)	(3.1±0.4)	2.2±0.4	1.6±0.6	2.6±0.2	2.8±1.3	11.9±0.8
	avg	5.8±1.1	10.8±2.2	7.0±1.1	2.4±0.6	3.4±1.1	3.3±1.3	5.0±3.1	26.4±2.8
	simult	4.4±0.3	7.9±0.4	6.2±0.3	2.2±0.1	3.5±0.2	2.8±0.3	[5.5]	21.1±0.6
	e12	1323.1	-2.070	2	4.8±1.4	13.7±1.6	11.5±1.7	32.9±2.7
	a'17	1366.214	-1.460	1	4.0±1.2	16.0±1.9	10.1±1.5	2.5±1.0	33.0±2.9
	d9	1422.28	-1.256	2	6.9±0.9	13.4±1.1	7.1±1.1	1.8±0.9	29.6±2.0
	d12	1366.443	-1.103	2	7.8±1.4	11.2±1.0	5.2±1.1	2.2±0.7	26.8±2.2
	a'14	1419.535	0.072	2	9.0±3.3	10.5±1.4	6.1±0.5	1.8±0.1	5.6±0.8	28.0±3.6
	avg	6.5±2.1	13.0±2.2	8.0±2.7	2.1±0.3	5.6	30.1±4.1
adopt	6.0±1.0	10.5±2.0	7.0±1.5	2.5±0.5	3.5±0.5	3.2±0.5	5.0±2.0	26.4±2.7	
					$N_{13}(0)$	$N_{13}(1)$	$N_{13}(2)$	$N_{13}(3)$				$N_{13}(\text{tot})$
¹³ CO	(8,0)	1325.793	0.428	1	12.2±1.2	16.9±1.5	8.4±1.2	4.8±1.2	42.3±2.6
	(7,0)	1347.575	0.747	1	11.6±0.9	22.1±1.2	8.1±0.6	1.0±0.5	42.8±1.7
	(6,0)	1370.617	0.951	1	17.0±2.1	21.7±1.7	9.0±0.7	1.1±0.4	48.8±2.8
	(5,0)	1395.229	1.306	1	10.6±1.6	19.8±2.1	6.4±0.5	1.8±0.2	38.6±2.7
	(4,0)	1421.340	1.537	1	13.3±2.8	23.4±3.6	7.4±0.7	1.2±0.2	45.3±4.6
	avg	12.9±2.5	20.8±2.5	7.9±1.0	1.3±0.4	42.9±3.7
	simult	12.8±0.8	21.1±0.9	7.6±0.3	1.5±0.1	43.0±1.2
d12	1370.928	0.322	1	12.7±1.7	21.6±2.2	11.1±2.1	4.4±2.3	49.8±4.2	
adopt	12.8±0.8	21.1±0.9	7.6±0.3	1.5±0.1	43.0±1.2	
					$N_{12}(0)$	$N_{12}(1)$						$N_{12}(\text{tot})$
C ¹⁸ O	(5,0)	1395.455	1.306	1	4.9±1.3	5.0±1.6	9.9±2.1
	(4,0)	1421.530	1.537	1	2.8±0.9	2.9±1.3	5.7±1.6
	simult	4.0±0.8	3.4±1.0	7.4±1.3

Note. — Subscript on $N(J)$ in column headings denotes power of ten for values in that column. Column densities in parentheses or square braces were fixed in fits to the line profiles.

^aReferences for f values: 1 = Morton & Noreau 1994; 2 = Eidelsberg & Rostas 2003.